STUDIA UNIVERSITATIS
BABEŞ-BOLYAI

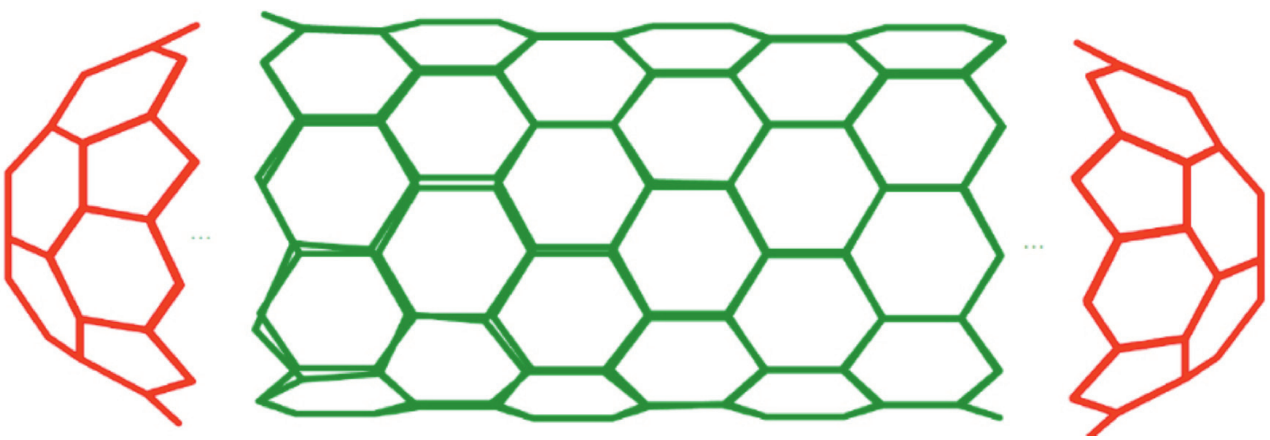

CHEMIA

1/2013

STUDIA
UNIVERSITATIS BABEŞ-BOLYAI

CHEMIA

1/2013

http://chem.ubbcluj.ro/~studiachemia/; studiachemia@chem.ubbcluj.ro

http://www.studia.ubbcluj.ro/serii/chemia/index_en.html

YEAR **Volume 58 (LVIII) 2013**
MONTH **MARCH**
ISSUE **1**

S T U D I A
UNIVERSITATIS BABEŞ–BOLYAI
CHEMIA

1

Desktop Editing Office: 51ST B.P. Hasdeu, Cluj-Napoca, Romania, Phone + 40 264-40.53.52

CUPRINS – CONTENT – SOMMAIRE – INHALT

Studia Universitatis Babes-Bolyai Chemia has been selected for coverage in Thomson Reuters products and custom information services. Beginning with V. 53 (1) 2008, this publication is indexed and abstracted in the following:

- Science Citation Index Expanded (also known as SciSearch®)
- Chemistry Citation Index®
- Journal Citation Reports/Science Edition

STUDIA UBB CHEMIA, LVIII, 1, 2013 (p. 7 – 19)
(RECOMMENDED CITATION)

EFFECTS OF A SINGLE DOSE OF ULTRAVIOLET B IRRADIATION ON OXIDANT/ANTIOXIDANT BALANCE IN THE EYE OF WISTAR RATS

SIMINA MUREŞAN[a], ADRIANA FILIP[a*], VIORICA SIMON[b], ADRIAN F. GAL[c], VIOREL MICLĂUŞ[c], NICOLETA DECEA[a], REMUS MOLDOVAN[a], ADRIANA MUREŞAN[a]

ABSTRACT. Solar ultraviolet radiation (UV) is a major cause of ocular injury contributing to photokeratitis, cataract and pterygium development. The aim of the study was to investigate the oxidant/antioxidant status of Wistar rat eyes after exposure to various doses of UVB in correlation with morphological and structural changes. Five groups of 8 animals each, randomly divided, were treated as follows: group 1: control, no UVB irradiation; group 2: a single UVB exposure to a dose of 45 mJ/cm^2; group 3: a single UVB exposure to 90 mJ/cm^2; group 4: a single UVB exposure to 180 mJ/cm^2; group 5: a single UVB exposure to 360 mJ/cm^2. At 24 hrs after UVB irradiation the animals were anaesthetized and sacrificed by cervical dislocation. The rat eyes from 5 animals were extracted and used for biochemical determinations and from 3 animals were harvested and used for histopathological investigation. Our results demonstrated that a single UVB exposure at different doses disturbs the oxidant-antioxidant balance in the eye tissues by lipid peroxides generation, activation of CAT and SOD and adaptative increasing of GSH levels, particularly at high doses. Twenty hours following UVB irradiation the cornea showed significant lesions: inflammation, hemorrhage, superficial/deep ulcerous keratitis and epithelial exfoliation. Severity of injuries was dose-dependent. These data suggest that oxidative stress may be responsible for the corneal lesions induced by UVB irradiation.

Keywords: *ultraviolet radiation, oxidative stress, eye, Wistar rats*

[a] *"Iuliu Hatieganu" University of Medicine and Pharmacy, Department of Physiology, 1 Clinicilor Street, 400006, Cluj-Napoca, Romania*
[b] *"Babes-Bolyai" University, Faculty of Physics, 1 Mihail Kogalniceanu Street, 400084, Cluj-Napoca, Romania*
[c] *Faculty of Veterinary Medicine, 3-5 Calea Manastur Street, 400372, Cluj-Napoca, Romania*
* *Corresponding author: adrianafilip33@yahoo.com*

INTRODUCTION

The ocular surface is constantly exposed to noxious agents from environment such as atmospheric oxygen (Holly et al., 1977), pollutants, chemical compounds and ultraviolet radiations (Tsubota et al., 1993). A large epidemiological data showed an association between ultraviolet radiation (UV) exposure and anterior pole ocular pathology (Mc Carty and Taylor, 2002). Thus, UV, especially UVB, penetrates the cornea and after absorption into the lens induces its damage by several mechanisms: formation of protein cross-linking, alteration of membrane transport system, swelling (Ringvold et al., 1997; Torriglia and Zigman, 1988), subcapsular vacuoles, deregulation of normal matrix dynamics (Ardan and Cejkova, 2012) and changes in cellular DNA (Wolf et al., 2008). These alterations have a major impact on metabolic pathways in the lens and explain the mechanisms involved in photokeratitis and subsequently in cataract and pterygium development (Johnson et al., 2004) (Berwick, 2000).

Generation of oxygen reactive species such as anion superoxide, hydrogen peroxide, singlet oxygen and hydroxyl radical is a well documented route for UVB-induced ocular damage (Andley, 1987; Goosey, 1980; Spector and Garner, 1981). Generally, cornea stops 92% of UVB and 60 % of UVA, especially its superficial layers (Ringvold et al., 1997). Moreover, it is known that anterior cornea is nourished by the tear film and posterior cornea by the aqueous humor, and both liquid media have protective, antioxidant, antibacterian and lubricant role. Thus, Crouch et al. reported that tears contain only superoxide dismutase (SOD) as antioxidant enzyme (Crouch et al., 1991) not catalase (CAT) or glutathione peroxidase (GPx). Other authors (Behndig et al., 1998) identified in human tears small quantities of SOD and large amounts of various non-enzymatic antioxidant including acid ascorbic, cysteine, lactoferrin (Kuizenga et al., 1987), tyrosine, glutathione and uric acid (Gogia et al., 1998). Aqueous humor has high quantities of ascorbate, glutathione and uric acid which remove reactive oxygen species generated by cellular metabolism and light exposure (Spector and Garner, 1991). The ascorbate protects the lens against lipooxygenase activity and counteracts the reactive oxygen species released by inflammatory cells during ocular inflammation (Williams and Paterson, 1986). The human cornea is rich in SOD, heme oxygenase-1 (HO-1) and NADPH cytocrome P450 reductase and the lens contain antioxidant enzyme such as SOD, CAT, GPx (Abraham et al., 1987; Behndig et al., 1998). The activities of all antioxidant enzymes dramatically decrease with age and after UV exposure and predispose cornea and lens to injury and diseases.

Increased levels of oxidants disturbs the balance between generation of free radicals and their inactivation by antioxidant defense systems and leads to alterations of epithelial membrane proteins, lipid oxidation, changes in ion

concentration and nuclear fragmentation (Soderberg, 1988). In addition, loss of thiol groups, methionine oxidation (Kovacic and Somanathan, 2008) and decreased proteasome activity disturbed redox balance and increase apoptosis (Wilhelm et al., 2007). Moreover, ROS are involved in activation of intracellular signaling pathways including nuclear factor kappa-B (NF-kB) and mitogen activated protein kinase (MAPK) with important consequences in early defensive reactions, in apoptosis and cell proliferation. In parallel, CAT, SOD and GPx activities decrease in the lens (Ringvold et al., 1997) and proinflammatory citokines are released.

Experimental *in vivo* studies certified that the rat lens has a maximum sensivity to UV around 300 nm (Merriam et al., 2000). Setting a maximum tolerable dose of UVB which does not induce damage and consequently cataract is a new goal in preventing ultraviolet radiation-induced changes. The purpose of the study was to investigate the oxidant/antioxidant status of rat eyes after exposure to various doses of UVB in correlation with morphological and structural changes.

RESULTS AND DISCUSSION

MDA is a useful marker for photooxidative damage. Exposures to 45 and 90 mJ/cm^2 of UVB did not reveal any changes in MDA levels in eye homogenates (0.12±0.02 respectively 0.16±0.02 nmoles/mg protein) compared to untreated eyes (0.25±0.16 nmoles/mg protein; $p>0.05$). The irradiation with high doses of UVB (180 and 360 mJ/cm^2) induced a 2.91 respectively 2.75 fold increase in lipid peroxidation as compared to eye exposed to 45 mJ/cm^2 UVB ($p<0.01$) (Figure 1). The increasing of lipid peroxidation was not dose dependent, the differences between MDA levels in groups irradiated with 180 and 360 mJ/cm^2 being insignificant ($p>0.05$).

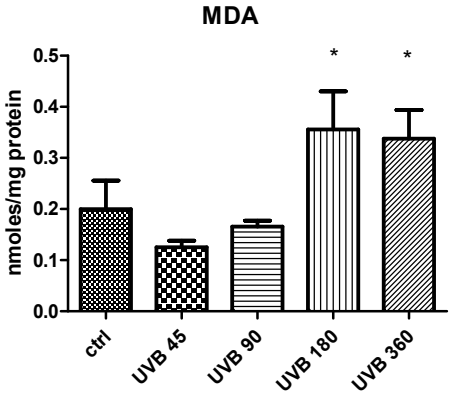

Figure 1. MDA level in eye homogenates exposed to single UVB irradiation

GSH levels increased significantly (6.0 fold) in the irradiated group with 45 mJ/cm^2 compared to the non UVB exposed group (5.16±0.84 vs. 0.86±0.66 nmoles/mg protein; $p<0.001$) (Figure 2). At 90 mJ/cm^2 of UVB the GSH generation also increased significantly compared to control group (3.53 fold; 3.04±0.70 vs. 0.86±0.66 moles/mg protein; $p<0.01$). The two high doses of UVB (180 respectively 360 mJ/cm^2) maintained low levels of GSH in eye tissues, insignificant compared with controls (0.83 ± 0.53 respectively 1.35 ± 0.94 nmoles/mg protein; $p>0.05$).

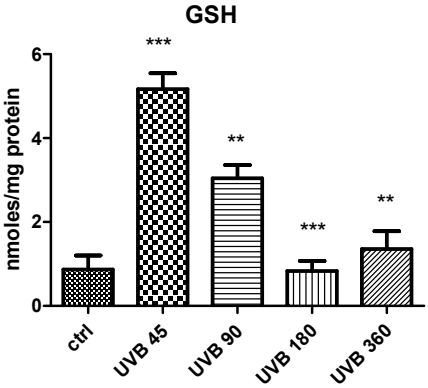

Figure 2. Glutathione reduced level in eye homogenates exposed to single UVB irradiation

GPx activity, under our experimental conditions, decreased insignificantly ($p>0.05$) at all doses administered (Figure 3).

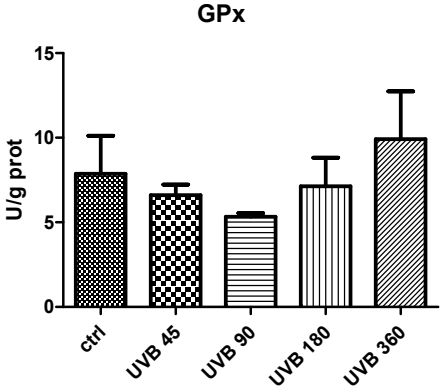

Figure 3. Glutathione peroxidase activity in eye homogenates exposed to single UVB irradiation

CAT activity increased significantly after exposure to 45 mJ/cm^2 (2.55 fold; 0.23±0.04 U/mg protein), 90 mJ/cm^2 (2.0 fold; 0.18±0.04 U/mg protein) and 180 mJ/cm^2 (2.88 fold; 0.26±0.10 U/mg protein) of UVB compared to no exposed animals (0.09±0.06 U/mg protein; $p<0.05$) (Figure 4). A dose of 360 mJ/cm^2 UVB decreased significantly CAT activity (0.08±0.05 U/mg protein; $p>0.05$), the values being similar to control group (Figure 4).

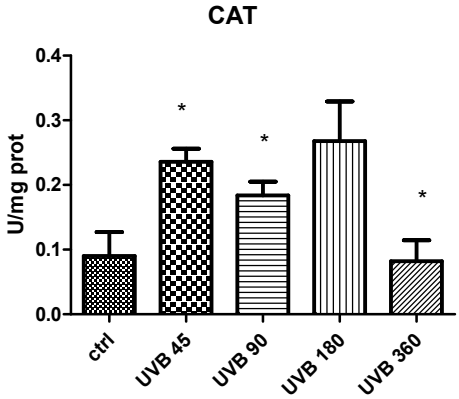

Figure 4. Catalase activity in eye homogenates exposed to single UVB irradiation

MnSOD activity at 24 hrs after the UVB irradiation increased significantly compared to control group only at dose of 360 mJ/cm^2 (2.23 fold; 1984±788.4 vs. 887.7±286.5 U/mg protein; $p<0.05$). Comparison remained significant between group treated with high dose and groups which received low doses of UVB. UVB exposures at doses of 45 mJ/cm^2 and 90 mJ/cm^2 (852.9±44.45 respectively 624.2±68.38 U/mg protein) maintain the reduced MnSOD activity in eye homogenates near to control group (Figure 5).

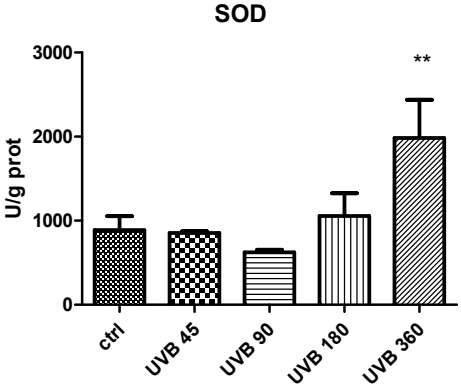

Figure 5. Superoxid dismutase activity in eye homogenates exposed to single UVB irradiation

The exposure of rats at different UV radiation doses was followed by the emergence of different intensity lesions in the cornea, related to the utilized radiation dose. Obvious lesions appear from 90 mJ/cm^2 dose and consist of corneal hypertrophy (1.5 fold), descuamation and zonal epithelial necrosis (superficial ulcerative keratitis), marked stromal edema, massive infiltration with polymorphonuclear cells in the vicinity of the ulcerated area, moderate and diffuse in the rest of the stroma (Figures 6 and 7).

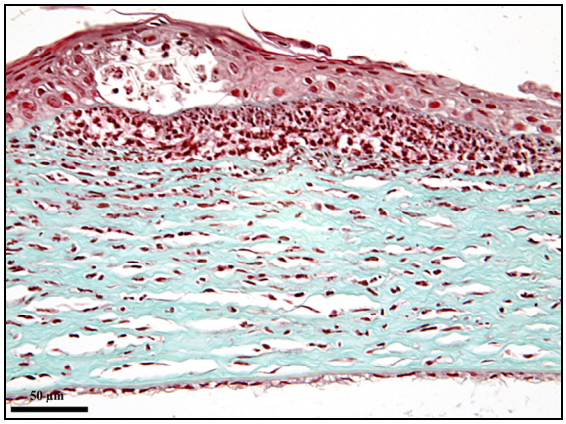

Figure 6. Group III – Cornea: superficial ulcerative keratitis, massive zonal infiltration with polymorphonuclear cells (Goldner's Trichrome)

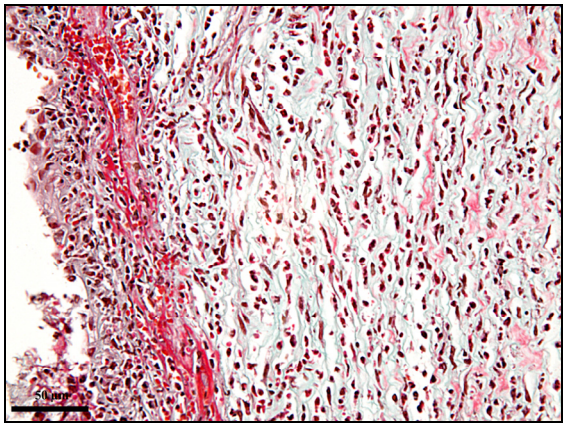

Figure 7. Group V – Cornea: generalized infiltration with polymorphonuclear cells, zonal hemorrhages (Goldner's Trichrome)

In order to estimate *in vivo* the threshold of UVB toxicity on the rat eye we investigated the parameters of oxidative stress in corelation with morphological changes under irradiation with different doses of UVB. It is known that direct

exposure to ambient ultraviolet light affect the cornea and the first changes are those caused by oxidative stress. Moreover, hydrogen peroxide is chronically present in the aqueous environment surrounding the anterior lens and may additional contribute to oxidative injury UVB-induced (Ringvold, 1980). To defend against damaging free radical-mediated reactions, cells possess antioxidant defense mechanisms. Thus, ocular tissues and fluids contain both nonenzymatic antioxidants (ascorbic acid, glutathione and α-tocopherol) and enzymatic antioxidants (catalase, superoxide dismutase, glutathione peroxidase and reductase). Superoxide dismutase protects the ocular tissue from the superoxide radicals and was detected in corneal epitelium and endothelium, lens epitelium, inner segments of the photoreceptor cell layer of the retina and in retinal pigment epitelium (Rao et al., 1985). The dismutation of superoxide by SOD leads to the formation of hydrogen peroxide, which is subsequently converted to water and oxygen through a reaction that is catalyzed by catalase (CAT) or glutathione peroxidase (GPx).

Our results demonstrated that acute UVB exposure at different doses disturbs the oxidant-antioxidant balance in eye tissues by lipid peroxides generation, activation of CAT and SOD and adaptative increasing of GSH levels, especially at high doses. Thus, MDA levels in eye homogenates increased at high doses of UVB in parallel with the decrease of GSH levels.

The UVB doses used in our experiment were chosen to reflect the human exposure of cornea to summer sunlight. It was known that during exposure of human cornea to sunlight 10 hours this received a dose of 0.105 J/cm^2 of UVB (Zigman, 1995). This dose evoked a significant increase in corneal hydration and light absorption.

GSH is a major non-protein thiol in living organisms, which plays a central role in coordinating the body's antioxidant defense process. GSH directly scavenge free radicals and acts as cofactor for GPx during the metabolism of hydrogen peroxide or lipid peroxides. Normally, in the cornea, GSH is found in the millimolar range (4-7 mM), the highest levels being found in the epithelium (Dalton et al., 2004). Generally, UVB exposure activates the transcriptional regulator NF-E2-related factor 2 (Nrf2) and consequently increases the activity of ROS-detoxifying enzymes and stimulates the production of antioxidants, including the glutathione (Schafer et al., 2010). In our study, the GSH enhancement after UVB exposure was important at low doses and was part of adaptive mechanisms triggered to remove reactive oxygen species. At high doses of UVB, GSH decreased dose-dependent due to counteract of reactive oxygen species generated in excess or leakage out of GSH from the lens due to injured of membrane (Hightower and McCready, 1992).

Several previous studies confirmed that UV exposure induced GSH depletion in lens of rabbits (Hightower and McCready, 1992) and rats irradiated (Risa et al., 2004; 2005; Tessem et al., 2006; Wang et al., 2010). Thus,

Hightower exposed cultured rabbit lenses to high doses of UV 315 nm and found a loss of 40 % GSH after irradiation. Wang noticed an average loss of 14% GSH concentration at 7 days after exposure to 8 kJ/m^2 UV 30 nm. Risa used for irradiation of rat lenses doses of 2-15 kJ/m^2 UV 300 nm.

Data in literature concerning these parameters following UV irradiation are rather contradictory probably due to differences in experimental design, UVB light sources used and variable interval between irradiation and evaluation. Thus, Ayala and co-workers did not find a depletion of GSH after UVB exposure of rats (Ayala and Soderberg, 2004). Risa et al. showed that *in vivo* exposure to UV light did not induce a detectable change of total lens GSSG levels (Risa et al., 2004; 2005). In our study, the GPx activity doesn't evolve in parallel to the level of GSH in the eye homogenates.

It is known that glutathione peroxidase (GPx) is a selenoprotein that catalyses the conversion of UV-induced hydrogen peroxide into water and molecular oxygen using GSH as unique hydrogen donor. It is possible to decrease the substrate due to activation of catalase, an enzyme that removes also hydrogen peroxide and protects superoxide dismutase from hydrogen peroxide-induced inactivation.

The results obtained support this hypothesis, the low and moderate doses of UVB increasing the activity of this enzyme. Other authors found that irradiation with 254 nm UV rays for two minutes lead to a decrease in catalase activity in the corneal epithelium, corneal endothelium and lens epithelium (Cejkova and Lojda, 1994). The same results were obtained when corneal epithelium of rabbits was exposed to four doses (1.1 – 1.6 J/cm^2) of UVB (Cejkova et al., 2001). The dose-dependent decline in catalase activity after UV exposure is explained by the direct photodestruction (Afaq and Mukhtar, 2001; Hellemans et al., 2003). In our experiment, MnSOD activity increased after high dose of UVB in order to dismute anion superoxide in hydrogen peroxide. Moreover, it has shown that UVB irradiation induced a release of soluble factors (IL-1α, Il-1β, TNF-α) that amplified MnSOD activity by a paracrine mechanism (Hachtroudi et al., 2002).

Experimental studies showed that ROS generated by UVB cause morphologic alterations in the cornea. A single UVB exposure of cornea blocked the proliferation of epithelial cells, determined the loss by autolysis of superficial corneal epithelial cells. The presence of the inflammatory polymorphonuclear cells infiltrate, directly proportional with the severity of the lesions, represents a morphologic evidence of the oxidative stress involvement in the lesions of the UVB exposed cornea (polymorphonuclear cells are a source of ROS). The presence of leukocytes in the irradiated corneal stroma was reported along with a gradual increase of the xanthine oxidase (Cejkova et Lojda, 1996) and D-amino acid oxidase activities in the corneal epithelium and endothelium (Čejkova et al., 2001). The experimental

generation of superoxide anion in the anterior chamber of the eye, in rabbit, determined the development of an early leukocytic infiltrate in the first 4 hrs from the irradiation (Cejkova et al., 2001).

The stromal inflammatory infiltrate can be induced by the release of interleukin 1β (IL-1β) from the damaged epithelial cells. IL-1β is a multipotent cytokine, involved in the acute neutrophils and macrophages inflammatory response (Wang et al., 2007). This experiment demonstrated the presence of lipid peroxidation in eye tissues in UVB exposures possibly due to release of ROS from polymorphonuclear cells which infiltrate the tissue injured.

Cornea of the rats exposed to 180 mJ/cm^2 presented more advanced lesions: over 2 fold thickening of the cornea, superficial ulcerative keratitis on a larger area in comparison to the anterior dose, very marked stromal edema and massive infiltration of polymorphonuclear cells. The lesions are more advanced at the 360 mJ/cm^2 dose. The cornea appears over 3 fold hypertrophyed, the ulceration from the central area reaches the Bowman membrane and extends into the depth. On the very marked edema background, the stromal liquefaction (keratomalacia) on large areas takes place. The polymorphonuclear infiltrate is very marked and generalized. In addition, diffuse hemorrhages are present and blood vessels appear in the corneal stroma.

CONCLUSIONS

Our results demonstrated that a single UVB exposure at different doses disturbs the oxidant-antioxidant balance in eye tissues by lipid peroxides generation, activation of CAT and SOD and adaptative increasing of GSH levels, particularly at high doses. Reactive oxygen species generated by UVB exposure may be responsible for morphologic alterations of the cornea.

EXPERIMENTAL SECTION

Materials

Trichloroacetic acid, o-phtalaldehyde, t-butyl hydroperoxide, glutathione reductase, glutathione reduced, Bradford reagent, cytochrome c, xanthine, xanthineoxidase, β – nicotinamide adenine dinucleotide phosphate reduced tetrasodium salt (NADPH) were purchased from Sigma-Aldrich Chemicals GmbH (Germany). 2-thiobarbituric acid and EDTA-Na_2 were obtained from Merck KGaA Darmstadt (Germany) and absolute ethanol, hydrogen peroxide and n-butanol from Chimopar (Bucuresti).

Experimental design

Forty female rats, 8 weeks old, weighing 120 ± 5 g, kept on normocaloric standard diet (VRF 1) and water *ad libitum,* were used. The animals were housed (5 animals/cage) at room temperature (24 ± 2^0C), with a 12/12 hrs light dark cycle. The rats were acclimatized to the laboratory for one week before the experiments. Five groups of 8 animals each, randomly divided, were treated as follows: group 1: control, received vehicle, no UVB irradiation; group 2: a single UVB exposure to a dose of 45 mJ/cm^2; group 3: a single UVB exposure to 90 mJ/cm^2; group 4: a single UVB exposure to 180 mJ/cm^2; group 5: a single UVB exposure to 360 mJ/cm^2. Before eye irradiation, the animals were anaesthetized with an i. p. injection of ketamine xylazine cocktail (90 mgkg^{-1} b.w. ketamine, 10 mgkg^{-1} b.w. xylazine). UVB irradiation was performed with a Waldmann UV 181 broadband UVB source, with 1.35 mW/cm^2 intensity, at 10 cm distance from the source. The UVB emission was monitored before each exposure with a Variocontrol radiometer (Waldmann GmbH, Germany). Irradiation doses were established using the formula: dose (mJ/cm^2) = exposure time (sec.) x intensity (mW/cm^2). All the experiments were performed according to the approved animal-care protocols of the Ethical Committee on Animal Welfare of the "Iuliu Hatieganu" University of Medicine, in accordance with the Romanian Ministry of Health and complied with the Guiding Principles in the Use of Animals in Toxicology. At 24 hrs after UVB irradiation the animals were anaesthetized and sacrificed by cervical dislocation. The rat eyes from 5 animals were extracted and used for biochemical determinations and from 3 animals were harvested and fixed in 10% buffered formalin for 48 hours (each eye ball was punctured laterally for a better fixation and crystalline extraction). The eye samples were then embedded in paraffin, cut at 5-µm thickness, and mounted on glass slides. Goldner's tricrome stain was performed for histological examinations. The eye sample harvesting and histological processing was realized in the Department of Histology, Faculty of Veterinary Medicine, Cluj-Napoca, Romania.

Measurement of oxidative stress parameters

Briefly, eye tissues were homogenized with a Polytron homogenizer (Brinkmann Kinematica, Switzerland) for 3 min on ice in phosphate buffered saline (pH7.4), added in a ratio of 1:4 (w/v). The suspension was centrifuged for 5 min at 3000 x g and 4 °C to prepare the cytosolic fractions. The proteins levels in homogenates were measured with Bradford method (Noble and Bailey, 2000). To evaluate the oxidative/antioxidative status we assessed the malondialdehyde, as marker of oxidative attack of reactive oxygen species on lipids, and the antioxidant enzymes activities (superoxide dismutase, catalase and glutathione peroxidase). In addition, we evaluated the level of glutathione reduced as antioxidant no enzymatic parameter.

Malondialdehyde (MDA) was determined using the fluorimetric method with 2-thiobarbituric acid described by Conti (Conti et al., 1991). The eye homogenate samples were heated in a boiling water bath for 1 h with a solution of 10 mM 2-thiobarbituric acid in 75 mM K_2HPO_4, pH 3 solution. After cooling the reaction product was extracted in n-butanol. The MDA was spectrofluorimetrically determined and the values are expressed as nmoles/mg protein.

Superoxide dismutase (SOD) activity was determined using cytochrome c reduction test with some adjustments (Beauchamp and Fridovich, 1971). Skin homogenates were introduced in a cytochrome c solution (2 μM in phosphate buffer 50 mM, pH 7.8) containing xanthine (5 μM). The reaction was started by adding xanthine oxidase (0.2 U/ml in 0.1 mM EDTA). The increasing absorbance at 550 nm, indicating cytochrome c reduction was recorded for 5 min. One unit of SOD inhibits the rate of increase in absorbance at 550 nm by 50% of those produced for a control sample without SOD under the conditions of the assay. Results were expressed in U/mg protein.

Catalase activity (CAT) was assayed according to Pippenger method (Pippenger et al., 1998) in a reaction mixture containing 10mM hydrogen peroxide in 50mM potassium phosphate buffer, pH7.4. The reduction in absorbance at 240 nm was recorded for 3 minutes. The enzyme quantity which produced an 0.43 reduction in absorbance per minute at 25^0 was defined as one unit of catalase activity and expressed as units/mg protein

Glutathione peroxidase activity (GPx) was determined with Flohe and Gunzler method, slightly modified (Flohe and Gunzler, 1984). The reaction mixture consisted in 1mM GSH, 0.24U/ml glutathione reductase and 0.15 mM NADPH (final concentrations) in 50 mM phosphate buffer (pH 7.0). The reaction mixture was incubated at 37º for 5 minutes with appropriate amounts of tissue homogenates. The assay was initiated with a (12mM) t-butyl hydroperoxide solution. The decrease in absorbance at 340 nm was recorded for 3 min. GPx activity was expressed as μmoles of NADP produced/min/mg protein and calculated using a molar absorbtivity for NADPH of $6.2x10^{-6}$, at 340 nm.

Reduced glutathione (GSH) was measured fluorimetrically using o-phtalaldehyde (Hu, 1994). Samples were treated with trichloroacetic acid (10%) and centrifuged. A solution of o-phtalaldehyde (1mg/ml in methanol) was added to supernatants diluted with sodium phosphate buffer 0.1M/EDTA 5mM, pH8.0. After 15 minutes, the fluorescence was recorded (350nm excitation and 420nm emission). GSH concentration was determined using a standard curve and expressed as nmoles/mg protein.

Statistical analysis

The data are expressed as the means± SD in five animals. Each measurement was done in triplicate. Comparisons were made by one-way ANOVA, with Tukey multiple comparisons test, using a GraphPad Prism software program, version 5.0 (GraphPad, San Diego, Ca, USA). $p < 0.05$ was considered as significant.

REFERENCES

1. N.G. Abraham, J.H. Lin, M.W. Dunn, M.I. Schwartzman, *Invest. Ophthalmol. Vis. Sci.,* **1987**, *28*, 1464-1472.
2. F. Afag, H. Mukhtar, *J. Photochem. Photobiol. B.,* **2001**, *63*, 61–9.
3. U.P. Andley, *Photochem. Photobiol.,* **1987**, *46*, 1057-1066.
4. T. Ardan, J. Cejkova, *Acta Histochem.,* **2012**, *114*(6), 540-6.
5. M. Ayala, P.G. Soderberg, *Ophtalmic. Research*, **2004**, *37*, 150-155.
6. C. Beauchamp, I. Fridovich, *Anal. Biochem*., **1971**, *44*, 276-282.
7. A. Behndig, B. Svensson, S.L. Marklund, K. Karlsson, *Invest. Ophthalmol. Vis. Sci.,* **1998**, *39*, 471-475.
8. M. Berwick, *Forum* (Genova), **2000**, *10*, 191-200.
9. J. Cejkova, Z. Lojda, *Acta Histochem.,* **1994**, *96*, 281-286.
10. J. Čejkova, J. Zvarova, M. Andonova, T. Ardan, *Histol Histopathol.,* **1999**, *14*, 471-478.
11. G.M. Cohen, *Biochem. J.,* **1997**, *326*(1), 1-16.
12. M. Conti, P.C. Moran, P. Levillain, *Clin. Chem.,* **1991**, *3*, 1273-1275.
13. R.K. Crouch, P. Goletz, A. Snyder, W.H. Coles, J. *Ocul. Pharmacol*., **1991**, *7*, 253-258.
14. T.P. Dalton, Y. Chen, S.N. Schneider, D.W. Nebert, H.G. Shertzer, *Free Radic. Biol. Med.,* **2004**, *37*(10), 1511-1526.
15. L. Flohe, W.A. Gunzler, *Method Enzymol.,* **1984**, *105*, 114-121.
16. R. Gogia, S.P. Richer, R.C. Rose, *Curr. Eye Res.,* **1998**, *17*, 257-263.
17. J.D. Goosey, J.S. Zigler, J.H. Kinoshita, *Science,* **1980**, *208*, 1278-1280.
18. L.N. Hachtroudi, T. Peters, P. Brenneisen, C. Meewes, C. Hommel, Z. Razi-Wolf, L.A. Schneider, J. Schuller, M. Wlaschek, K. Scharffetter-Kochanek, *Arch Dermatol.*, **2002**, *138*, 1473-1479.
19. L. Hellemans, H. Corstjens, A. Neven, L. Declercq, D. Maes, *J Investig. Dermatol.,* **2003**, *120*, 434-439.
20. K.R. Hightower, J.P. McCready, *Current Eye Research,* **1992**, *11*, 679-689.
21. F.J. Holly, M.A. Lemp, *Surv. Ophthalmol.,* **1977**, *22*, 69-87.

22. M.L. Hu, *Methods Enzymol.,* **1994**, *233*, 380-384.
23. G.J. Johnson, *Eye*, **2004**, *18*(12), 1235-1250.
24. P. Kovacic, R. Somanathan, *Cell membranes and free radical research,* **2008**, *1*, 2-1, 56-69.
25. A. Kuizenga, N.J. Van Haeringen, A. Kijlstra, *Invest. Ophthalmol. Vis. Sci.,* **1987**, *28*, 305-313.
26. C.A. McCarty, H.R. Taylor, *Dev. Ophthalmol.,* **2002**, *35*, 21-31.
27. J. Merriam, S. Lofgren, R. Michael, P.G. Soderberg, J. Dillon, L. Zheng, M. Ayala, *Invest. Ophthalmol. Vis. Sci.*, **2000**, *41*, 2642-2647.
28. J.E. Noble, M.J.A. Bailey, *Methods Enzymol*., **2000**, *463*, 72-95.
29. C.E. Pippenger, R.W. Browne, D. Armstrong, Humana Press Inc. Totowa N.J. **1998**, 299-311.
30. N.A. Rao, L.G. Thaete, J.M. Delmage, A. Sevanian, *Invest Ophthalmol. Vis. Sci.*, **1985**, *26*, 1778-1781.
31. A. Ringvold, *Acta Ophthalmol. (Copenh.),* **1980**, *58*, 69-82.
32. A. Ringvold, *Acta Ophthalmol. Scand.,* **1997**, *75*, 496-498.
33. O. Risa, O. Saether, M. Kakar, V. Mody, S. Lofgren, P.G. Soderberg, J. Ktarane, A. Midelfart, *Exp Eye Res.,* **2005**, *81*, 407-414.
34. O. Risa, O. Saether, P.G. Soderberg, J. Krane, A. Midelfart, *Investig. Ophthalmology and Visual Science*, **2004**, *45*, 1916-1921.
35. M. Schafer, S. Dutsch, U. Keller, F. Navid, A. Schwarz, D. Johnson, J. Johnson, S. Werner, *Genes & Dev.,* **2010**, *24*, 1045-1058.
36. P.G. Soderberg, *Acta Ophtalmol. (Copenh.),* **1988**, *66*, 11-152.
37. A. Spector, W.H. Garner, *Exp. Eye Res*., **1981**, *33*, 673-681.
38. M. Tesem, T. Bathens, S. Lofgren, V. Mody, V. Meyer, X. Dong, P.G. Soderberg, A. Midelfart, *Investigative Ophthalmology and Visual Science,* **2006**, *47*, 5404-5411.
39. A. Torriglia, S. Zigman, *Curr. Eye Res.*, **1988**, *7*, 539-548.
40. K. Tsubota, K. Nakamori, *N Engl. J Med*., **1993**, *328*, 584.
41. Z. Wang, J.T. Handa, W.R. Green, W.J. Stark, R.S. Weinberg, A.S. Jun, *Ophthalmology,* **2007**, *114*(8), 1453-1460.
42. J. Wang, S. Lofgren, X. Dong, K. Galichanin, P.G. Soderberg, *Acta Ophthalmologica,* **2010**, *88*, 779-785.
43. J. Wilhelm, Z. Smistik, G. Mahelkova, R. Vytasek, *Cell Biochem. Funct.,* **2007**, *25*, 317-321.
44. R.N. Williams, C.A. Paterson, *Exp. Eye Res.,* **1986**, *42*, 211-218.
45. N. Wolf, W. Pendergrass, N. Singh, K. Swisshelm, J. Schwartz, *Mol. Vis.,* **2008**, *14*, 274-285.
46. S. Zigman, *Optom. Vis. Sci.,* **1995**, *72*, 899-901.

STUDIA UBB CHEMIA, LVIII, 1, 2013 (p. 21 – 30)
(RECOMMENDED CITATION)

RHEOLOGICAL BEHAVIOR OF SOME OILS ADDITIVATED WITH MIXED PYROMELLITIC ESTERS

SORINA BORAN[a], ANDRA TĂMAŞ[a*]

ABSTRACT. The paper presents the rheological behavior study of castor oil additivated by different types of mixed pyromellitic esters. The influence of pyromellitic esters' structure and concentration was determined, as well as that of temperature, on the rheological behavior, by setting the dependence between the shear stress τ and the shear rate $\dot{\gamma}$. The analysis of dependence $\tau = f(\dot{\gamma})$ demonstrates that the solutions studied present Newtonian behavior.

Keywords: *dynamic viscosity, flow activation energy, lubricating, oil additives*

INTRODUCTION

Along with the need to protect the environment, using vegetable oil-based lubricants has become an important alternative in tribology.

Generally, a lubricant has two major components, base oil and different auxiliary materials which have the property to improve the characteristics of oil used. The basic materials suitable for producing ecological lubricants are vegetable oils because of their high biodegradability, regeneration capacity, low toxicity and wide variety of sources [1, 2]. Unlike mineral oil-based lubricants those based on vegetable oils are rapidly and completely biodegradable, without having a negative effect on the ecosystem. However, their thermal and hydrolytic stability are comparatively lower than that of synthetic oils and need to be improved through a number of measures [3-5].

The main functions of a lubricant is to reduce friction and wear, to dissipate heat, to disperse deposits, to inhibit corrosion and rusting, and the main properties of a base oil is a relatively constant viscosity, low solidification temperature, low deposit formation, low volatility, good thermal -oxidative and hydrolytic stability, and to be biodegradable [6].

[a] *"Politehnica" University of Timisoara, Faculty of Industrial Chemistry and Environmental Engineering, Bd. V. Pârvan Nr. 6, RO-300223 Timişoara, Romania*
* *Corresponding author: andra.tamas@chim.upt.ro*

The vegetable oils used for this purpose can be both edible category (sunflower, soybean, coconut, peanut, palm, rapeseed) and inedible (castor oil) [7, 8]. Lubricating properties of castor oil were studied and were reported to be similar or better than those of vegetable oils commonly used [4, 9].

In this paper as a base vegetable oil was used the castor oil, and as auxiliary materials (which are able to improve the characteristics of oil used) the paraffin oil and a pair of pyromellitic esters whose synthesis and characterization have been published [10, 11].

The main characteristics of the pyromellitic esters (P1 and P2) are found in Table 1. The two esters differ in the molar ratio between the radicals' 2-phenoxy ethyl and 2 - ethyl hexyl derived from the alcohols used for the esterification of pyromellitic anhydride (2:2 for P1 and 3:1 for P2).

Table 1. The properties of the pyromellitic esters used

Ester	Molecular formula	Molecular weight, $kg.kmol^{-1}$	Density at 20˚C, $kg.m^{-3}$	Refractive index at 20˚C	Saponification index, mg KOH/g
P1	$C_{42}H_{54}O_{10}$	718	1103	1.5258	311.42
P2	$C_{42}H_{46}O_{11}$	726	1176	1.5523	309.34

The composition of the samples with esters content is presented in Table 2. In all cases, the castor oil content is 93 wt %. As standard (sample A0) it was used the castor oil with boiling point 313ºC and density $910\,kg\cdot m^{-3}$ (at 20ºC). At the same temperature, the density of paraffin oil was $790\,kg\cdot m^{-3}$.

Table 2. The composition of the analyzed samples

Symbol	Composition, wt %		Symbol	Composition, wt %	
	P1	Paraffin oil		P2	Paraffin oil
A1	2	5	**B1**	2	5
A2	3.5	3.5	**B2**	3.5	3.5
A3	5	2	**B3**	5	2
A4	7	0	**B4**	7	0

The samples preparation was done by dispersing the pyromellitic ester under intense stirring in oils mixture at room temperature (~25˚C). The rheological characterization of the samples was carried out using rotational viscometer Rheotest-2, under thermostatic conditions, at temperature values between 50÷80˚C, close to the operating conditions of lubricated parts. It was followed the establishment of rheological relations $\tau = f(\dot{\gamma})$, as well as the calculation of the flow activation energy E_a [12, 13].

RESULTS AND DISCUSSION

Viscosity is one of the main properties of the oil used and its value should vary as little as possible in operation, at all engine-operating conditions. Oils additivation with different types of synthetic esters is done in order to improve lubricating properties of the base vegetable oil. This additivation should not negatively influence rheological characteristics of the oil. Thus, it was followed the rheological behavior of castor oil additivated with pyromellitic esters, at different concentrations.

The influence of ester type used as an additive, on rheological behavior of castor oil was studied for different concentrations of additive, at three temperature values. In Figure 1, $\tau = f(\dot{\gamma})$ dependence is shown for esters concentration of 3.5 wt. %.

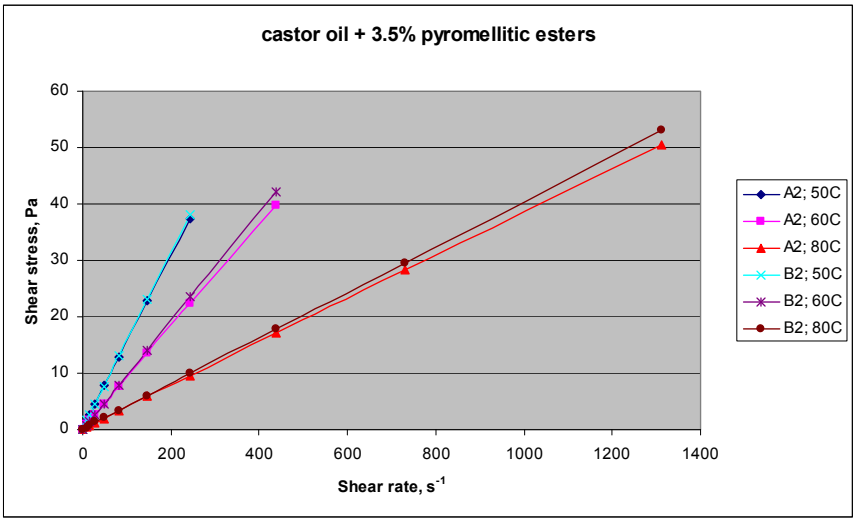

Figure 1. The dependence $\tau = f(\dot{\gamma})$ for samples A2 and B2, at different temperatures

The rheological equations corresponding to these dependencies are shown in Table 3.

Table 3. Rheological equations for samples A2 and B2

Temperature, ˚C	Equation $\tau = \eta \cdot \dot{\gamma}$		Viscosity increasing*, %
	A2	B2	
50	$\tau = 0.1540 \cdot \dot{\gamma}$	$\tau = 0.1567 \cdot \dot{\gamma}$	1.75
60	$\tau = 0.0908 \cdot \dot{\gamma}$	$\tau = 0.0965 \cdot \dot{\gamma}$	6.30
80	$\tau = 0.0385 \cdot \dot{\gamma}$	$\tau = 0.0404 \cdot \dot{\gamma}$	4.94

** Sample B2 compared with sample A2*

It is noted that for these pyromellitic esters, changing the molar ratio of alcohols' used for esterification does not change significantly the oil viscosity and no modifies its Newtonian behavior. The temperature increasing leads to the decrease of samples' viscosity but without the change of the Newtonian behavior.

Also, it was studied the influence of additive concentration on the rheological behavior of castor oil. For pyromellitic ester P1, at a temperature of 60˚C, $\tau = f(\dot{\gamma})$ dependence is shown in Figure 2.

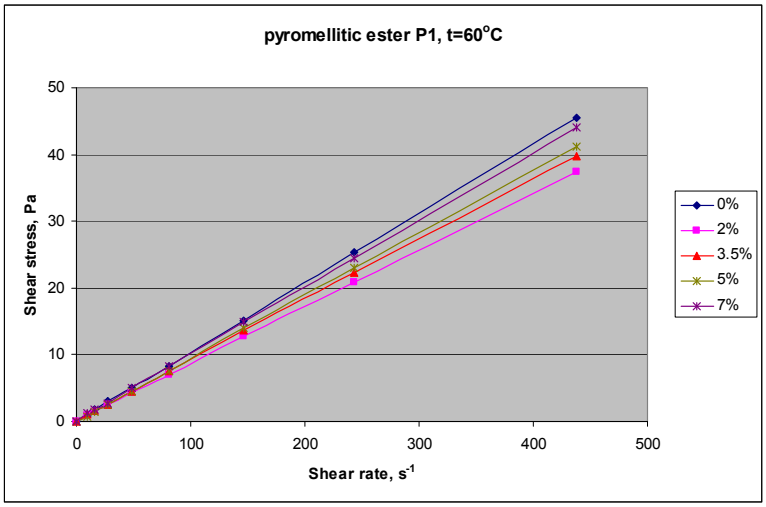

Figure 2. Dependence $\tau = f(\dot{\gamma})$ for samples A0-A4

From the slope of the obtained straight lines it is observed that the addition of pyromellitic ester leads to the decrease of samples viscosity in comparison with the viscosity of oil without additives. The viscosity decrease is relatively small; the most pronounced decrease corresponds to the minimum additive content (2%), followed by its increase with the ester content increasing, but without reaches the corresponding value of pure oil. A similar situation occurs too when the oil is additivated with P2 pyromellitic ester. The obtained viscosity values are presented in Table 4.

Table 4. Dynamic viscosities of the analyzed samples

Symbol	Viscosity, mPa.s		Symbol	Viscosity, mPa.s	
	50ºC	80ºC		50ºC	80ºC
A0	171.4	43.5	**-**	-	-
A1	150.3	36.5	**B1**	150.5	39.5
A2	154.0	38.5	**B2**	156.7	40.4
A3	161.1	40.4	**B3**	161.1	42.1
A4	169.6	42.9	**B4**	164.6	43.5

The exponential decrease of the samples viscosity with the temperature is described by an Arrhenius-type equation:

$$\eta = A \cdot \exp\left(E_a / R \cdot T\right) \tag{1}$$

where E_a - the flow activation energy, $J \cdot mol^{-1}$; R - the gas constant, $J \cdot mol^{-1} \cdot K^{-1}$; T - absolute temperature, K; A - the material constant *Pa·s*.

Through the measurements achievement at different temperatures it was possible to establish the dependence $\ln\eta = f(1/T)$ and to calculate the values of flow activation energy E_a. Particular expressions of equation (1) for the samples A0-A4 and B1-B4 are given in Tables 5a and 5b.

Table 5a. Arrhenius-type equations for samples A0-A4

Content of P1 ester, wt%	$\eta = A \cdot \exp\left(E_a / R \cdot T\right)$	$E_a,\ kJ \cdot mol^{-1}$
0	$\eta = 1.70 \cdot 10^{-5} \cdot \exp\left(5212/T\right)$	43.3
2	$\eta = 0.95 \cdot 10^{-5} \cdot \exp\left(5347/T\right)$	44.4
3.5	$\eta = 1.30 \cdot 10^{-5} \cdot \exp\left(5256/T\right)$	43.7
5	$\eta = 1.45 \cdot 10^{-5} \cdot \exp\left(5240/T\right)$	43.5
7	$\eta = 1.65 \cdot 10^{-5} \cdot \exp\left(5212/T\right)$	43.3

Table 5b. Arrhenius-type equations for samples B1-B4

Content of P2 ester, wt%	$\eta = A \cdot \exp\left(E_a / R \cdot T\right)$	$E_a,\ kJ \cdot mol^{-1}$
2	$\eta = 2.25 \cdot 10^{-5} \cdot \exp\left(5074/T\right)$	42.2
3.5	$\eta = 1.80 \cdot 10^{-5} \cdot \exp\left(5161/T\right)$	42.9
5	$\eta = 2.25 \cdot 10^{-5} \cdot \exp\left(5096/T\right)$	42.3
7	$\eta = 2.70 \cdot 10^{-5} \cdot \exp\left(5043/T\right)$	41.9

It is noted that for the same type of ester, the variation of the flow activation energy with the additive concentration is insignificant. Also, it is observed that the slight increase in molecular mass for pyromellitic ester P2 compared with P1 ester leads, on the one hand, to an increase in the constant A, but also to a decrease of flow activation energy on average 3%.

Using particular expressions of $\eta = f(1/T)$ dependence, the values of dynamic viscosity of the samples were determined in the temperature range 20÷100˚C. Thus, for samples A0, A2 and A4, the viscosity evolution is shown in Figure 3.

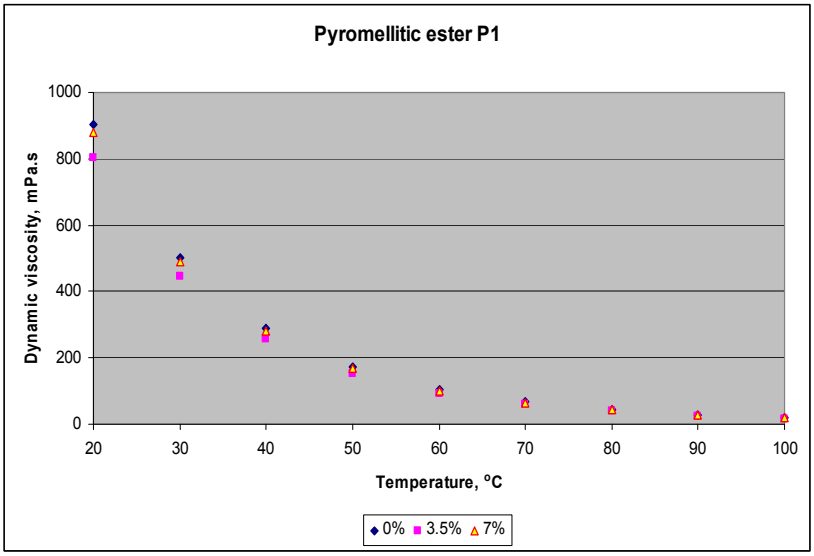

Figure 3. Dynamic viscosity vs. temperature for samples A0, A2 and A4

It is found that with increasing temperature, the values of samples' dynamic viscosity are closer, regardless of the percentage of additive used.

Since lubrication is used, usually, in rotating systems (bearings, gears etc), the dynamic characteristics (speed, dynamic pressure, shear stress) will be expressed in terms of Taylor-Reynolds criterion (Ta_{Re}) specific to this type of motion. This criterion is also used to characterize fluids flow in annulus under the effect of rotational motion.

The values of Ta_{Re} criterion were calculated with relation (2), taking into account the radii of the inner and outer cylinder (r_i and r_o), the inner cylinder revolution n and the fluid properties (viscosity η and density ρ) [14]:

$$Ta_{\mathrm{Re}} = \frac{2 \cdot \pi \cdot n \cdot r_i \cdot (r_o - r_i) \cdot \rho}{\eta} \tag{2}$$

Increasing the hydrodynamic regime, characterized by dimensionless criterion Ta_{Re}, leads to a pronounced decrease of the ratio between shear stress τ (experimentally determined) and dynamic pressure P_{dyn} calculated with the maximum speed.

By analogy with the fluids flow through straight pipes, the dynamic pressure of the fluid in motion in ring-shaped spaces is calculated with:

$$P_{dyn} = \frac{\rho \cdot w_{\max}^2}{2} \tag{3}$$

$$w_{\max} = \pi \cdot d_i \cdot n \tag{4}$$

where $w_{\max}$ is the speed of fluid laminar layer placed next to the moving wall (inner cylinder), d_i - the inner diameter of the ring-shaped space, n - the inner cylinder revolution.

For the samples A0, A2 and A4, at constant temperature, the variation of $\tau/P_{dyn} = f(Ta_{\mathrm{Re}})$ ratio is shown in Figure 4. How change of temperature affects the same dependence, for sample A2, is shown in Figure 5.

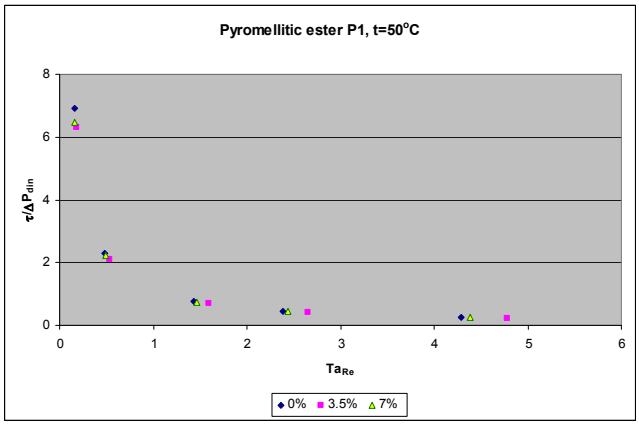

Figure 4. $\tau/P_{dyn} = f(Ta_{\mathrm{Re}})$ dependence for samples A0, A2 and A4

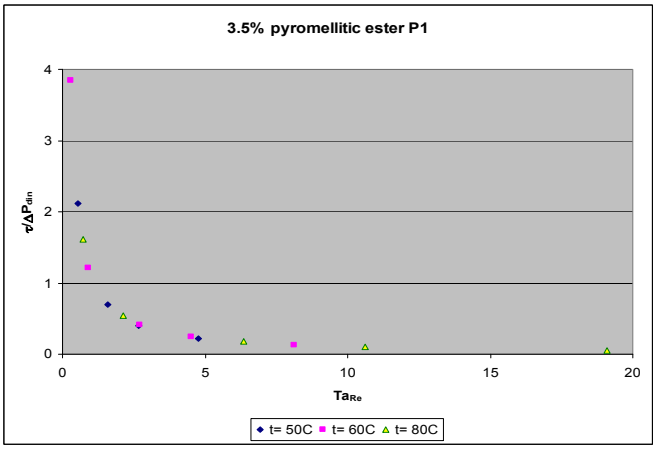

Figure 5. The temperature influence on $\tau/P_{dyn} = f(Ta_{\mathrm{Re}})$ dependence (sample A2)

One can notice that the graphical representation places the results after a parabolic curve with overlapping points, without significant changes depending on the additive concentration or temperature. The profile of both dependencies shows an accentuated decrease with the increasing of hydrodynamic flow regime.

By analogy with the circular motion of the fluid in stirring processes [15, 16], the ratio τ/P_{dyn} is correlated with Ta_{Re} criterion by a relationship of type:

$$\tau/P_{dyn} = C \cdot Ta_{\mathrm{Re}}^{m} \tag{5}$$

or, particularized by logarithmic representation:

$$\ln(\tau/P_{dyn}) = \ln C + m \cdot \ln(Ta_{\mathrm{Re}}) \tag{5a}$$

The particular forms of relationship (5a) determined for sample A2, at different temperatures, are shown in Table 6a. To a temperature of 50˚C, for samples A0, A2 and A4, the particular forms of relation (5a) are shown in Table 6b.

Table 6a. Particular forms of equation (5a) for sample A2

Temperature, ˚C	$\ln(\tau/P_{dyn}) = \ln C + m \cdot \ln(Ta_{\mathrm{Re}})$	C
50	$\ln(\tau/P_{dyn}) = 0.0957 - 1.0135 \cdot \ln(Ta_{\mathrm{Re}})$	1.100
60	$\ln(\tau/P_{dyn}) = 0.1103 - 1.0166 \cdot \ln(Ta_{\mathrm{Re}})$	1.117
80	$\ln(\tau/P_{dyn}) = 0.1417 - 1.0128 \cdot \ln(Ta_{\mathrm{Re}})$	1.152

Table 6b. Particular forms of equation (5a) for samples A0, A2 and A4, at 50˚C

Symbol	$\ln(\tau/P_{dyn}) = \ln C + m \cdot \ln(Ta_{\mathrm{Re}})$	C
A0	$\ln(\tau/P_{dyn}) = 0.0850 - 1.0055 \cdot \ln(Ta_{\mathrm{Re}})$	1.089
A2	$\ln(\tau/P_{dyn}) = 0.0957 - 1.0135 \cdot \ln(Ta_{\mathrm{Re}})$	1.100
A4	$\ln(\tau/P_{dyn}) = 0.0727 - 0.9945 \cdot \ln(Ta_{\mathrm{Re}})$	1.075

Considering the shear stress τ equivalent to the friction pressure drop, it can be assumed that the ratio of the two quantities is equal to the friction coefficient λ corresponding to laminar flow regime ($\lambda = 64 \cdot \mathrm{Re}^{-1}$).

This assumption is confirmed from two directions: on the one hand, the Ta_{Re} values lower than 60, which is the critical value that separates the laminar regime of the turbulent, for fluids flow in annulus [17-20]. On the other

hand, from equations presented in Tables 6a and 6b, it is observed that the values of m coefficient are very close to the value -1, similar to the Reynolds' exponent from the expression of friction coefficient.

CONCLUSIONS

It was studied the rheological behavior of castor oil additivated with mixed pyromellitic esters, monitoring the influence of theirs type and concentration, as well as that of temperature.

For each analyzed sample (pure castor oil, respectively, additivated in different proportions), it was obtained a linear dependence between shear stress τ and the shear rate $\dot{\gamma}$, without yield point τ_0, which shows Newtonian behavior.

Additivation does not significantly change the value of the dynamic viscosity of castor oil but has favorable effects in terms of its lubricating properties.

The rheological equations corresponding to the dependence $\tau = f(\dot{\gamma})$ were determined and, from the slope of the obtained straight lines, was calculated their dynamic viscosity. Also, from the temperature influence, were calculated the flow activation energies and it was established the dependence between the rheological parameters and Taylor-Reynolds criterion (Ta_{Re}), specific to rotational motion.

EXPERIMENTAL SECTION

Determinations were made using the rotational viscometer Rheotest-2 with the system vat-drum S/S_1. For each analyzed sample, the shear stress measurement was performed both to increasing and decreasing values of the shear rate.

The samples were analyzed after one day of preparation.

REFERENCES

1. L. Rhee, *NLGI Spokesman*, **1996**, *60(5)*, 28.
2. R.L. Goyan, R.E. Melley, P.A. Wissner, W.C. Ong, *Lubrication Engineering*, **1998**, *54(7)*, 10.
3. I. Lesiga, M. Picek, K. Nahal, *Journal of Synthetic Lubrication,* **1997**, *13(4)*, 347.
4. S.Asadauskas, J.M. Perez, J. Duda, *Lubrication Engineering*, **1997**, *53(12)*, 35.

5. R. Becker, A. Knots, *Lubrication Science*, **1996**, *8*, 295.
6. S.Z. Erhan, “Vegetables oils as lubricants, hydraulic fluids and inks- Bailey’s Industrial Oil and Fat Products”, 6th ed., John Wiley & Sons Inc., New Jersey, **2005**.
7. O.N. Anand, C.V.Kumar, *Journal of Synthetic Lubrication*, **2006**, *23(2)*, 91.
8. P.V. Joseph, D. Saxena, D.K.Sharma, *Journal of Synthetic Lubrication*, **2007**, *24(4)*, 181.
9. Y. Gerbig, S.I.Ahmed, F.A. Gerbig, H. Haefke, *Journal of Synthetic Lubrication*, **2004**, *21(3)*, 177.
10. L.E. Mirci, “Esteri micşti pe bază de anhidridă piromelitică şi procedeu de obţinere a acestora”, Brevet RO 111760, **1996**.
11. L.E. Mirci, S. Ţerescu (Boran), G. Istrătucă, *Rev. Mat. Plast.*, **1999**, *36(1)*, 13.
12. A. Tămaş, M. Vincze, *Studia UBB Chemia,* **2011**, *56(2)*, 85.
13. A. Tămaş, M. Vincze, *Studia UBB Chemia,* **2011**, *56(3)*, 247.
14. N. Bors, "Contribuţii la studiul influenţei unor substanţe chimice asupra îmbunătăţirii curgerii lichidelor", Teză de doctorat, Universitatea "Politehnica" Timişoara, **2010**.
15. A.G. Kasatkin, "Procese şi aparate principale în tehnologia chimică", ed. a II-a, Ed. Tehnică, Bucureşti, **1963**.
16. K.F. Pavlov, P.G. Romankov, A.A. Noskov, "Procese şi aparate în ingineria chimică - Exerciţii şi probleme", Ed. Tehnică, Bucureşti, **1981**.
17. N. Borş, A. Tămaş, Z. Gropşian, *Chem.Bull."Politehnica" Univ. (Timişoara)*, **2008**, *53(67)*, 1-2, 16.
18. N. Borş, A. Tămaş, *Scient. Bull. "Politehnica" Univ. of Timişoara*, Transactions on Mechanics, **2010**, *1*, 81.
19. A. Tămaş, N. Borş, R. Minea, *Bull. of Petroleum-Gas Univ. of Ploieşti,* Technical Series, **2008**, *LX, 4B,* 105.
20. N. Borş, A. Tămaş, Z. Gropşian, *Studia UBB Chemia*, **2009**, LIV, *4(1)*, 55.

STUDIA UBB CHEMIA, LVIII, 1, 2013 (p. 31 – 41)
(RECOMMENDED CITATION)

DETERMINATION OF METHYLDOPA IN HUMAN PLASMA BY LC/MS-MS FOR THERAPEUTIC DRUG MONITORING

LAURIAN VLASE[a], DAN MIHU[b], DANIELA-SAVETA POPA[a*], ADINA POPA[a], CORINA BRICIU[a], FELICIA LOGHIN[a], RĂZVAN CIORTEA[b], CARMEN MIHU[b]

ABSTRACT. A simple and rapid liquid chromatography coupled with tandem mass spectrometry (LC/MS/MS) method for therapeutic level monitoring of methyldopa in human plasma was developed and validated. The separation was performed on a Zorbax SB-C18 column under isocratic conditions using a mobile phase of 2:98 (v/v) acetonitrile and 0.2% (v/v) formic acid in water at 40ºC with a flow rate of 0.8 mL/min. The detection of was performed using an ion trap MS with electrospray positive ionisation in multiple reaction monitoring (MRM) mode (m/z 212.1 →139.2, 166.2, 195.2). The human plasma samples (0.2 mL) were deproteinised with methanol and aliquots of 1.5 µL from supernatants obtained after centrifugation were directly injected into the chromatographic system. The method shows a good linearity, precision (CV < 8.4 %) and accuracy (bias < 11.1 %) over the range of 0.32-20.48 µg/mL plasma. The lower limit of quantification (LLOQ) was 0.32 µg/mL and the recovery was between 90.9-101.4 %. The method is fast, with a minimum time for plasma sample preparation and a run-time of 1.5 min for instrument analysis (retention time of methyldopa was 1.05 min). The developed and validated method is simple, rapid, selective and sufficiently sensitive to be applied in clinical level monitoring, pharmacokinetics or bioequivalence studies of methyldopa.

Keywords: *methyldopa, LC/MS-MS, therapeutic drug monitoring*

INTRODUCTION

Methyldopa, 2-amino-3-(3,4-dihydroxyphenyl)-2-methylpropanoic acid, (Fig. 1), is an antihypertensive drug with central action [1]. It stimulates the central alpha-2-adrenoreceptors, primarily by its metabolite alpha-methyl-norepinephrine, and decreases sympathetic outflow and blood pressure [2, 3].

[a] *"Iuliu Haţieganu" University of Medicine and Pharmacy, Faculty of Pharmacy, Emil Isac 13, RO-400023, Cluj-Napoca, Romania*
[b] *"Iuliu Haţieganu" University of Medicine and Pharmacy, Faculty of Medicine, Emil Isac 13, RO-400023, Cluj-Napoca, Romania*
* *Corresponding author: dspopa@yahoo.com*

Methyldopate hydrochloride is another drug also used in antihypertensive therapy. It is the ethyl-ester of methyldopa, so a prodrug thereof, becoming pharmacologically active through its metabolism to methyldopa [1].

The chemical structure of methyldopa is analogue of dopa (dihydroxy-phenylalanine), from which it differs through the presence of a methyl group on the alpha-carbon of the side chain, containing thus a chiral centre (Fig. 1). The S-isomer is responsible for antihypertensive activity [2, 4].

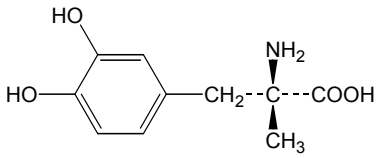

Figure 1. Chemical structure of methyldopa

After oral administration, the absorption of methyldopa is approximately 42% (± 16%). The peak plasma levels occur in 2–4 h and the therapeutic plasma concentrations are usually in the range 1-5 μg/mL. The plasma protein binding is < 20%. The drug is excreted in the urine as decarboxylated metabolites, sulphate conjugate, and unchanged drug [1, 3]. About 40% of the oral dose is excreted in the urine in 48 h, of which about 40% is the conjugate, and a considerable amount of unchanged drug is eliminated in the faeces. Methyldopa has a half-life of about 2 h, but a longer terminal elimination half-time has also been reported [1]. After IV administration of methyldopate, the bioavailability of methyldopa is similar to oral administration because a large portion of ester is not hydrolyzed to methyldopa. Between 52-82% of a IV dose is excreted in the urine in 36 h, and only ~2% is conjugated [1, 3].

Methyldopa is not generally used as a first-line drug in antihypertensive therapy due to its frequent side effects, as sedation and drowsiness, and also sympathetic depression. But it lowers blood pressure without compromising renal blood flow or the glomerular filtration rate, being preferred especially in hypertensive patients with renal complications [2]. It also represents one of the drugs frequently used in pregnancy to treat non-severe hypertension [5, 6]. Therapeutic drug monitoring is required in these cases to ensure the effectiveness of drug treatment and to avoid possible adverse effects.

Several methods involving spectrofluorimetry [7] and high-performance liquid-chromatography (HPLC) with UV [8, 9], fluorescence [7, 9-11], electrochemical [12] or mass spectrometry (MS) [13] detection has been reported to determine therapeutic levels of methyldopa in biological samples: serum [9, 10] or plasma [7, 8, 11-14], urine [7, 12], breast milk [14]. Several of these methods are long and include extraction procedures that prolong the time and cost of analysis.

Generally, the sensitivity of native fluorescence detection of catecholamines, including methyldopa, is three orders of magnitude lower than those detectable by UV. Greater sensitivity is obtained by fluorescence detection after derivatisation, but the time of analysis is longer due to derivatisation steps required [9]. Electrochemical detection offers good sensitivity, however it includes long separation times and usually needs quite complex extractions [12].

In the last decade, mass spectrometry has become the detection mode preferred for liquid chromatography due to its powerful performances: it allows the identification of separated compounds with high accuracy and sensitivity, particularly selective determination, and robustness [15-20]. Sample preparation is commonly simple and rapid and often requires only precipitation of proteins (PP) before chromatographic analysis [13, 17, 20].

The aim of this work was to develop and validate a high-throughput LC/MS-MS method to quantify methyldopa levels in human plasma. This method will be applied in therapeutic drug monitoring and bioavailability studies.

RESULTS AND DISCUSSION

The developed LC/MS-MS method was optimized and validated. It is rapid, with a total run time of instrumental analysis of 1.5 min and a retention time of methyldopa of 1.05 min (Fig. 2). Sample preparation was short including only the precipitation of proteins and processing a small volume of plasma (0.2 mL). The sensitivity was good (LLOQ of 0.32 µg/mL), sufficient to determine therapeutic levels of methyldopa ranging between 1-5 µg/mL. The absolute recoveries were high (between 90.9±6.3 al LLOQ and 99.3±6.1 at 10.24 µg/mL, respectively).

Sample preparation

In the developed method volumes of only 0.2 mL plasma were precipitated with methanol (0.6 mL) and analysed by direct injection of centrifuged supernatant into the chromatographic system. This method is more rapid and offers a shorter time of analysis, and thus a lower cost of routine determinations as compared to the other methods reported in literature (Table 1).

The method involved in sample preparation can influence the chromatographic background level and generate matrix suppression effect in LC-MS assays. No matrix interference or ion suppression was observed from the plasma samples in the developed method. In the scientific literature, there were reported some methods that also used protein precipitation (with perchloric acid or methanol) without extraction for the determination of methyldopa

in human plasma [8, 9, 13]. Several researchers prefer to include in plasma sample preparation an extraction step to eliminate the impurities and to increase the sensitivity (Table 1). Due to the amphoteric nature of methyldopa that would make the isolation difficult by simple liquid-liquid extraction (LLE), solid-phase extraction (SPE) or/and alumina extraction are preferred as isolation methods [10-12]. But the extraction steps increase the time of analysis and the costs of routine determinations, and can affect the recovery.

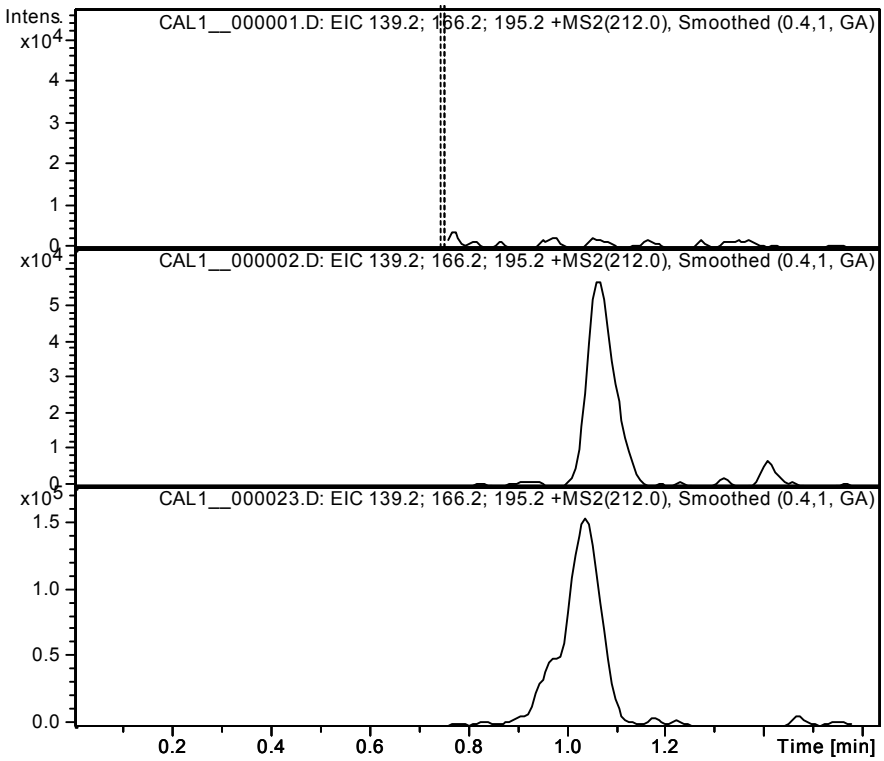

Figure 2. Representative chromatograms of (up) drug-free plasma, (middle) plasma spiked with methyldopa at LLOQ (0.32 μg/mL) and (down) plasma sample obtained from a patient 60 min after administration of methyldopa (concentration found: 1.12 μg/mL).

Li *et al.* used HPLC with diode array detection (DAD) combined with second-order calibration based on alternating trilinear decomposition algorithm for simultaneous quantitative analysis of methyldopa, levodopa and carbidopa. They obtained a good sensitivity (LOQ = 0.244 μg/mL), and a good linearity for the studied range of methyldopa (0.0-7.0 μg/mL), but a relatively long retention time of 3.46 min [8].

Only a LC-MS/MS assay is reported for quantification of methyldopa in human plasma after protein precipitation with perchloric acid. The quantification was performed in MRM mode (m/z 212.1→166.1). Methyldopa has a retention time of 3.4 min and the authors obtained a LOQ of 20 ng/mL. But the recovery was poorer in comparison with our method (93±5, 89±7 and 83±11% for 0.025, 0.25 and 2.5 µg/mL, respectively) [13].

Table 1. Analytical characteristics of some reported HPLC methods for the determination of methyldopa in human plasma or serum

Ref.	Matrix (mL)	Pre-treatment/ extraction[c]	Stationary phase	Mobile phase constituents[b]	Detection mode[a]	LOQ[d] (µg/mL)	Rt[e] (min)	Absolute recovery (%)
Our method	Plasma (0.2)	PP with methanol	Zorbax SB-C18	ACN: 0.2% (v/v) formic acid (2:98,v/v)	ESI-MS/MS, MRM, m/z 212.1→(139.2, 166.2, 195.2)	0.32	1.05	90.9-101.4
Oliveira [13]	Plasma (0.2)	PP with $HClO_4$	Genesis C18	10 mM ammonium acetate buffer (pH 5)-MeOH (70:30,v/v)	ESI-MS/MS, MRM (m/z 212.1→166.1)	0.02	3.4	88
Li [8]	Plasma (0.25)	PP with methanol	Hypersil-ODS	MeOH-0.002M KH_2PO_4 (pH 5) (25:75, v/v)	DAD + SOC-ATLD	0.244	3.46	104±2.6
Muzzi [9]	Serum (0.25)	PP with $HClO_4$	Supercosil LC-18	MeOH-0.02M KH_2PO_4 (pH 2.5), gradient	FD	105 pmol/mL	14.5	NA[f]
				50 mM Tris (pH 7)-MeOH - ACN (8:1:1)	FD with derivatisation	50 pmol/mL		
Bahrami [10]	Serum (1.0)	Alumina extraction	Shimpack-CLC-ODS	MeOH-0.05M KH_2PO_4 (+ TEA, pH 2.3) (8:92, v/v)	FD	0.02	1.7	98±3
Rona [11]	Plasma (1.0)	SPE	Nucleosil 7 C18	5 mM HSA-Na salt containing 0.05 M KH_2PO_4 (pH 3.2)-CAN, gradient	FD	0.01	6.068	94

[a] DAD, diode array detection; SOC-ATLD, second-order calibration based on alternating trilinear decomposition algorithm; FD, fluorescence detection; MRM, multiple reaction monitoring; [b]MeOH, methanol; ACN, acetonitrile; TEA, triethylamine; HAS, heptansulfonic acid; [c]PP, protein precipitation; SPE, solid phase extraction; [d]LOQ, limit of quantification; [e]Rt, retention time; [f]NA, not available.

LC-MS assay

The chromatographic conditions, especially the composition of the mobile phase, were optimized in several trials to achieve maximum peak responses and symmetrical chromatographic peaks, a short retention time of methyldopa

and consequently a shorter run time of analysis. The best results were obtained with the mixture of acetonitrile and 0.2% (v/v) formic acid in water (2:98, v/v) under isocratic conditions.

The electrospray ionization (ESI) in positive ion mode offers significantly higher signals for methyldopa compared to ESI in negative ion mode or atmospheric pressure chemical ionization (APCI). The direct MS detection is used for pharmaceutical purposes in qualitative rather than quantitative analysis. The use of tandem MS detection allows the obtention of better selectivity and sensitivity by the fragmentation of the molecular ion into several ions. The molecular ion $[M+H]^+$ (m/z 212.2) of methyldopa was fragmented into three abundant ions (m/z 195.2, 166.2, 139.2) at the optimum collision energy of 1.2 V (Fig. 3). The detection was carried out in multiple reaction monitoring (MRM) and the extracted ion chromatogram (EIC) of m/z (195.2, 166.2, 139.2) from m/z 212.2 was monitored and analyzed.

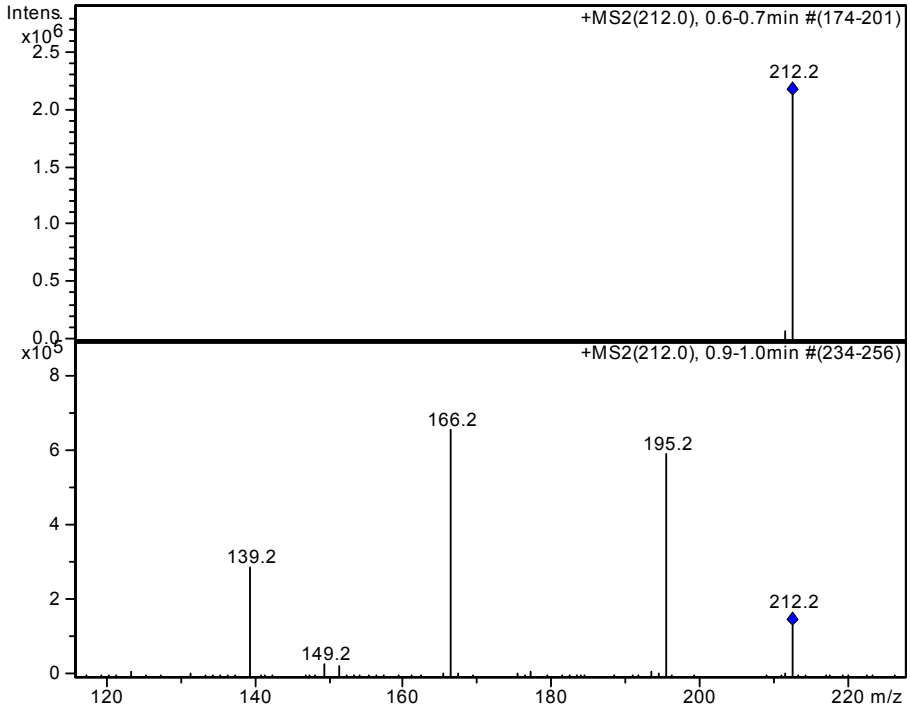

Figure 3. Mass spectra of methyldopa obtained by electrospray ionisation in positive ion mode at the collision energy of 1.2 V: (up) full-scan spectrum with molecular ion $[M+H]^+$ (m/z 212.2); (down) MS/MS reactive spectrum (after fragmentation into monitored ions: m/z 195.2, 166.2, 139.2).

Table 2. The intra-day precision (CV %), accuracy (bias %) and recovery data for the measurement of methyldopa in human plasma (the analysis of five different samples, n = 5)

Nominal concentration (μg/mL)	Found concentration mean μg/mL	± SD	CV (%)	Bias (%)	Recovery (%)	± SD
0.32	0.33	0.02	5.3	2.2	93.7	5.0
0.64	0.61	0.02	2.6	-4.5	95.6	11.1
2.56	2.59	0.12	4.5	1.2	97.0	3.1
10.24	11.38	10.37	3.3	11.1	101.4	2.8

Table 3. The inter-day precision (CV %), accuracy (bias %) and recovery data for the measurement of methyldopa in human plasma (one analysis on five different days, n = 5)

Nominal concentration (μg/mL)	Found concentration mean μg/mL	± SD	CV (%)	Bias (%)	Recovery (%)	± SD
0.32	0.33	0.02	7.6	2.7	90.9	6.3
0.64	0.62	0.02	2.8	-2.3	94.2	5.1
2.56	2.48	0.21	8.4	-3.2	101.0	4.1
10.24	10.95	0.47	4.3	6.9	99.3	6.1

Assay validation

The method was validated in accordance with international regulations [21, 22]. Representative chromatograms of drug-free plasma and plasma spiked with methyldopa at LLOQ are shown in Fig. 2. No interfering peaks from the endogenous plasma components were observed in the retention time of methyldopa.

The calibration curves were described by a quadratic equation over the concentration range of 0.32 – 20.48 μg/mL in human plasma, with a correlation coefficient greater than 0.99. The LLOQ was 0.32 μg/mL, being the lowest concentration having an intra- and inter-day CV and bias under 20% [21]. The values obtained for intra-day and inter-day precision and accuracy during the validation are shown in Tables 2 and 3, respectively.

All values for accuracy and precision were within recommended limits (<15%). The means of absolute recovery values were between 90% and 101%.

Method application

The validated method was used for therapeutic drug monitoring of methyldopa in pregnant women treated for hypertension. Blood sampling was made at 60 min after drug administration (starting with 1g methyldopa daily) and the mean found concentration was 1.81±0.89 μg/ml (n=14). The drug

plasma levels under 0.9 μg/ml were clinically correlated with an insufficient decrease of arterial tension and the daily methyldopa dose was increased to 1.5 or 2 g.

CONCLUSION

The developed and validated LC-MS/MS method satisfied the requirements of a high-throughput assay by its sensitivity, specificity, speed and simplicity. In comparison with other published HPLC [8-12, 14] or LC-MS/MS [13] methods for therapeutic level monitoring of methyldopa in human plasma, the developed method performs better in terms of volume of analyzed plasma sample, analyte recovery, and rapidity (both sample preparation and chromatographic run-time), which are essential attributes for methods used in routine analysis. The method can be successfully applied in bioequivalence or pharmacokinetics studies, or for therapeutic level monitoring of methyldopa.

EXPERIMENTAL SECTION

Reagents

Acetonitrile and methanol of isocratic grade for liquid chromatography, and formic acid of analytical-reagent grade were purchased from Merck KGaA (Darmstadt, Germany). Deionised water was obtained using a Milli-Q Water purification system (Millipore, Milford, MA, USA). The human blank plasma was supplied by the Regional Blood Transfusion Centre of Cluj-Napoca (Romania) from healthy volunteers, men and women.

Apparatus

The following apparatus were used: 204 Sigma Centrifuge (Osterode am Harz, Germany); Analytical Plus and Precision Standard Balance (Mettler-Toledo, Switzerland); Vortex Genie 2 mixer (Scientific Industries, New York, USA); Ultrasonic bath Elma Transsonic 700/H (Singen, Germany). The HPLC system used was an 1100 series Agilent Technologies model (Darmstadt, Germany) consisting of two G1312A binary pumps, an in-line G1379A degasser, an G1329A autosampler, a G1316A column oven and an Agilent Ion Trap Detector 1100 VL.

Chromatographic and spectrometric conditions

Chromatographic separation was performed on a Zorbax SB-C18 (100 mm x 3.0 mm i.d., 3.5 μm) column (Agilent Technologies) under isocratic conditions using a mobile phase consisting of a 2:98 (v/v) mixture of acetonitrile

and 0.2% (v/v) formic acid in water at 40 ºC with a flow rate of 0.8 mL/min. The detection of methyldopa was performed in multiple reaction monitoring (MRM) mode using an ion trap mass spectrometer equipped with an electrospray ion (ESI) source, positive ionisation (capillary 4500 V, nebulizer 60 psi (nitrogen), dry gas nitrogen at 12 L/min, dry gas temperature 350ºC). The extracted ion current (EIC) chromatogram of m/z (139.2, 166.2, 195.2) from m/z 212 was analyzed.

Standard solutions

A stock solution (4.0 mg/mL) was prepared by dissolving an appropriate quantity of methyldopa in methanol. A working solution (32 µg/mL) was prepared by appropriate dilution in drug-free human plasma. This solution was used to prepare plasma calibration standards with the concentrations of 0.32, 0.64, 1.28, 2.56, 5.12, 10.24, and 20.48 µg/mL. Quality control (QC) samples of 0.64 µg/mL (low), 2.56 µg/mL (medium) and 10.24 µg/mL (high) were prepared by adding the appropriate volumes of working solution to drug-free human plasma. The obtained plasma calibration standards and quality control standards were pipetted into 15 mL polypropylene tubes and stored at -20ºC until analysis.

Sample preparation

Standards and plasma samples (0.2 mL) were deproteinised with methanol (0.6 mL). After vortex-mixture (10 s) and centrifugation (2 min at 12000 rpm), the supernatants (0.2 mL) were transferred to autosampler vials, and 1.5 µL were injected into the HPLC system.

Method validation

The specificity of the method was evaluated by comparing the chromatograms obtained from the plasma samples containing methyldopa with those obtained from different plasma blank samples (n=6).

The concentration of methyldopa was determined automatically by the instrument data system using peak areas and the external standard method. The calibration curve model was determined by the least squares analysis: $y = c + bx + ax^2$, weighted (1/y) quadratic regression, where y - peak area of the analyte and x - concentration of the analyte (µg/mL).

The intra-day precision (expressed as coefficient of variation, CV %) and accuracy (expressed as relative difference between obtained and theoretical concentration, bias %) were determined by analysing five different samples (n = 5) from each QC standards (at low, medium and high levels) on the same day. The inter-day precision and accuracy were determined by analysing one sample from each of the QC standards (at low, medium and high levels), in the course of five different days (n = 5).

The lower limit of quantification (LLOQ) was established as the lowest calibration standard with an accuracy and precision less than 20%.

The relative recoveries (at LLOQ, low, medium and high levels) were measured by comparing the response of the spiked plasma with the response of standards in solvent with the same concentration of methyldopa as the plasma (n = 5).

ACKNOWLEDGEMENTS

This work was supported by an internal grant of University of Medicine and Pharmacy "Iuliu Haţieganu" Cluj-Napoca.

REFERENCES

1. A.C. Moffat, M.D. Osselton, B. Widdop, "Clarke's Analysis of Drug and Poisons in pharmaceuticals, body fluids and postmortem material", Pharmaceutical Press, Inc, London, **2011**, 1672.
2. D.P. Westfall, "Antihypertensive drugs", in: C.R. Craig, R.E. Stitzel, "Modern Pharmacology With Clinical Applications", 6th ed., Lippincott Williams & Wilkins, **2004**, 235.
3. P. Anderson, J. Knoben, W. Troutman, "Handbook of clinical drug data", 10th ed., McGraw-Hill, New York, **2002**, 340.
4. E.A. Gadkariem, K.E.E. Ibrahim, N.A.A. Kamil, M.E.M. Haga, H.A. El-Obeid, *Saudi Pharmaceutical Journal*, **2009**, *17,* 289.
5. L.A. Magee, E. Abalos, P. von Dadelszen, B. Sibai, T. Easterling, S. Walkinshaw, CHIPS Study Group. *Br J Clin Pharmacol.*, **2011**, *72*, 394.
6. C.G. Solomon, E.W. Seely, *Endocrinol Metab Clin North Am.*, **2011**, *40*, 847.
7. B.K. Kim, R.T. Koda, *J Pharm Sci.*, **1977**, *66*, 1632.
8. S.F. Li, H.L. Wu, Y.J. Yu, Y.N. Li, J.F. Nie, H.Y. Fu, R.Q. Yu, *Talanta*, **2010**, *81*, 805.
9. C. Muzzi, E. Bertocci, L. Terzuoli, B. Porcelli, I. Ciari, R. Pagani, R. Guerranti, *Biomed Pharmacother.*, **2008**, *62*, 253.
10. G. Bahrami, A. Kiani, S. Mirzaeei, *J Chromatogr B Analyt Technol Biomed Life Sci.,* **2006**, *832*, 197.
11. K. Róna, K. Ary, B. Gachályi, I. Klebovich, *J Chromatogr A*, **1996**, *730*, 125.
12. C. Lucarelli, P. Betto, G. Ricciarello, G. Grossi, *J Chromatogr.*, **1991**, *541*, 285.
13. C.H. Oliveira, R.E. Barrientos-Astigarraga, M. Sucupira, G.S. Graudenz, M.N. Muscará, N.G. De, *J Chromatogr B Analyt Technol Biomed Life Sci.*, **2002**, *768*, 341.
14. J.A. Hoskins, S.B. Holliday, *J Chromatogr.*, **1982**, *230*, 162.

15. L. Vlase, S. Vancea, C. Mircioiu, C.E. Lupusoru, D. Marchidan, C.M. Ghiciuc, *Studia UBB Chemia*, **2011**, *56*, 181.
16. D.S. Popa, B. Kiss, L. Vlase, A. Pop, R. Iepure, R. Paltinean, F. Loghin, *Farmacia,* **2011***, 59*, 539.
17. L. Vlase, D.S. Popa, C. Siserman, D. Zaharia, *Rom. J. Leg. Med*, **2011**, *19*, 145.
18. L. Vlase, D. Muntean, M. Cuciureanu, R. Cuciureanu, S. Gocan, *J. Liq. Chromatogr.& Related Tech*., **2011***, 34*, 436.
19. L. Vlase, D. Muntean, M. Achim, *Studia UBB Chemia,* **2010***, 55*, 305.
20. D.S. Popa, L. Vlase, D. Chirila, F. Loghin, *Rom. Rev. Lab. Med.,* **2010***, 18*, 37.
21. Guidance for Industry, Bioanalytical Method Validation. U.S. Department of Health and Human Services, Food and Drug Administration. Federal Register, **2001**, *66*.
22. Guidance on the Investigation of Bioavailability and Bioequivalence. The European Agency for the Evaluation of Medicinal Products, Committee for Proprietary Medicinal Products, **2001**, CPMP/EWP/QWP/1401/98.

STUDIA UBB CHEMIA, LVIII, 1, 2013 (p. 43 – 50)
(RECOMMENDED CITATION)

COMPUTING THE WIENER INDEX OF AN INFINITE CLASS OF FULLERENES

MODJTABA GHORBANI[a*] and TAYEBEH GHORBANI[b]

ABSTRACT. One the most famous topological index is the Wiener index. It represents the sum of distances of a connected graph and was widely used in correlational studies involving various physical, chemical and biological properties. This topological index was introduced in 1947 by one of the pioneer of this area Harold Wiener. In the present paper, we compute the Wiener index of an infinite class of fullerenes.

Key Words: *Wiener index, Fullerene graphs, Distance matrix*.

INTRODUCTION

Throughout this paper all graphs considered are simple and connected. The vertex and edge sets of a graph G are denoted by $V(G)$ and $E(G)$, respectively. The distance $d_G(x, y)$ between two vertices x and y of V(G) is defined as the length of any shortest path in G connecting x and y. The distance number or Wiener index is a topological invariant widely used in studies of structure-property and structure-activity. In the last decades it has been also studied by pure mathematics, see [1 – 5].

The Wiener index was first defined by Wiener to obtain the sum of distances between carbon atoms in saturated hydrocarbons [6] but, Hosoya reformulated the Wiener index respect to the distances between any pair of vertices:

$$W(G) = \sum_{u,v \in V(G)} d_G(u,v).$$

[a] *Department of Mathematics, Faculty of Science, Shahid Rajaee Teacher Training University, Tehran, 16785-136, I.R. Iran*
[b] *Institute of Nanoscience and Nanotechnology, University of Kashan, Kashan 87317-51167, I.R. Iran*
* *Corresponding author: mghorbani@srttu.edu*

Some physical properties, such as the boiling point, are related to the geometric structure of the molecules. The first investigations of the Wiener index were made by Harold Wiener in 1947 who realized that there are correlations between the boiling points of paraffin and the structure of the molecules.

The main goal of this paper is to compute the Wiener index of a new infinite class of fullerene graphs, C_{20n+60}. The first member of this class is the well-known IPR fullerene C_{60} with icosahedral symmetry group. Here, our notation is standard and mainly taken from standard books of graph theory [7]. We encourage reader to references [8 - 12] for more details about the concept of Wiener index.

RESULTS AND DISCUSSION

Fullerene graphs are mathematical models of fullerenes, polyhedral molecules made of carbon atoms whose faces are pentagons and hexagons. A fullerene is a planar, 3-regular and 3-connected graph that has only pentagonal and hexagonal faces. Such graphs on n vertices exist for all even $n \geq 24$ and for $n = 20$. By Euler's theorem, one can prove that the number of pentagons and hexagons in a fullerene molecule C_n are 12 and $n/2 - 10$, respectively. The first fullerene discovered by Robert Curl, Harold Kroto and Richard Smalley was buckminsterfullerene C_{60}, [13, 14]**.**

In this section by solving a recursive sequence we determine the Wiener index of a class of fullerene graphs with exactly $20n + 60$ ($n = 0, 1, 2,..$) vertices. Clearly, they have $10n + 90$ edges. We denote this class of fullerenes by C_{20n+60}. The first member of this class can be obtained by putting $n = 0$, see Figure 1.

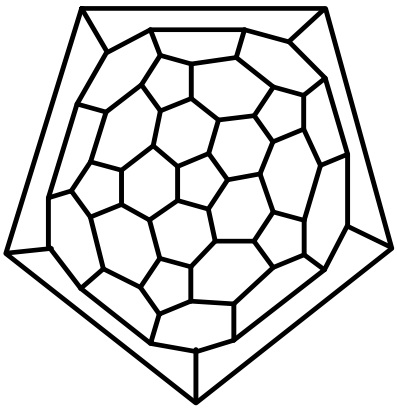

Figure 1. 2 – D graph of fullerene C_{20n+60}, $n = 0$.

In this paper we prove that the Wiener index of this class of fullerenes for $n \geq 8$ is as follows:

$$W\left(C_{20n+60}\right) = 10(40n^3 + 360n^2 + 310n + 663)/3.$$

We can also apply our method to compute the Wiener index in other classes of fullerene graphs. Zhang et al. [15] is described a method to obtain a fullerene graph from a zig–zag or armchair nanotubes.

Denote by $T_Z[n, m]$ a zig–zag nanotube with n rows and m columns of hexagons, see Figure 2. Combine a nanotube $T_Z[n, 10]$ with two copies of the cap B (Figure 3) as shown in Figure 4, the resulted graph being an IPR fullerene, which has $20n + 60$ vertices and exactly $10n + 20$ hexagonal faces.

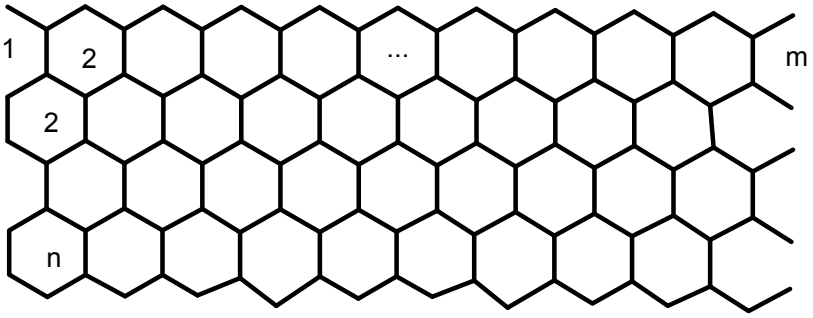

Figure 2. 2 – *D* graph of zig – zag nanotube $T_z[n, m]$, for $m = 10$ and $n = 6$.

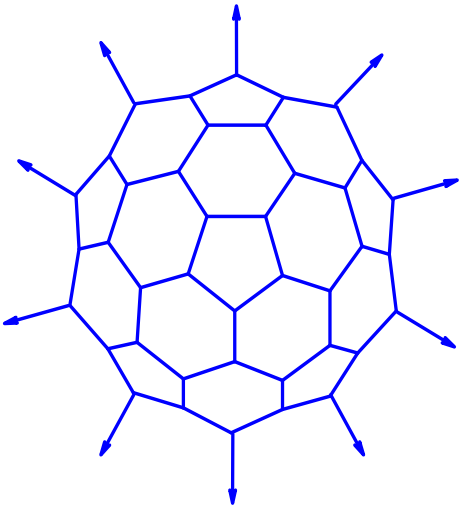

Figure 3. Cap *B*.

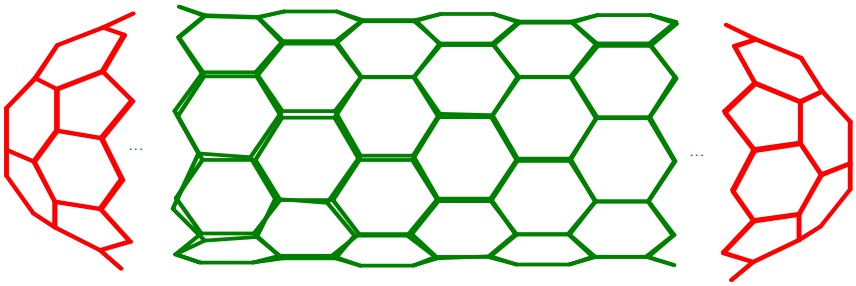

Figure 4. Fullerene C_{20n+60} constructed by combining two copies of caps B and the zigzag nanotube $T_Z[n, 10]$.

A block matrix is a matrix whose entries are again a matrix. In other words, the block matrix can be written in terms of smaller matrices. By using the concept of the block matrices, we stated

Theorem 1. The Wiener index of the $G = T_Z[n, 10]$ nanotube for $n \geq 9$ is calculated as:

$$W(G) = \frac{484}{3}n^3 + 484n^2 + \frac{30371}{3}n - 16819.$$

Proof. According to Figure 5, it is easy to see that $T_Z[n, 10]$ nanotube has $n + 1$ layers of vertices. Let $U = \{u_1, u_2, \ldots, u_{10}\}$ be the vertices of the last row. To compute the Wiener index of this nanotube we make use of a recursive sequence method. Let also U_n be the Wiener index of $G = T_Z[n, 10]$. By using definition of the Wiener index one can see that:

$$\begin{aligned} 2W(G) = U_n &= \sum_{x,y\in U} d(x,y) + \sum_{x,y\in V\setminus U} d(x,y) \\ &\quad + \sum_{x\in V, y\in V\setminus U} d(x,y) \\ &= 90 + U_{n-1} + \sum_{x\in V, y\in V\setminus U} d(x,y). \end{aligned}$$

Thus, it is enough to compute the summation $\sum_{x\in V, y\in V\setminus U} d(x,y)$, but by using the symmetry of this graph we have:

$$\sum_{x\in V, y\in V\setminus U} d(x,y) = 5[d(u_1) + d(u_2)],$$

where, $d(u_1) = \sum_{v\in V\setminus U} d(u_1, v)$ and d(u_2) can be defined by a similar way. By computing these values one can see that:

$$\begin{aligned} d(u_1) &= 437 + 199(n-2) + 30(n-2)(n-3) + (n-2)(n-3)(n-4), \\ d(u_2) &= 431 + 193(n-2) + 28(n-2)(n-3) + (n-2)(n-3)(n-4). \end{aligned}$$

This implies that $U_{n+1} = U_n + 90 + 5[d(u_1) + d(u_2)] = 10n^3 + 200n^2 + 770n + 1920$. By solving this recursive sequence we have:

$$W(G) = \frac{484}{3}n^3 + 484n^2 + \frac{30371}{3}n - 16819.$$

Finally, by computing the Wiener index of $T_Z[n, 10]$ for $n = 1, \ldots, 8$, as reported in Table 1, the proof is completed.

As a corollary of Theorem 1, we can compute the Wiener index of C_{20n+60} fullerenes as follows:

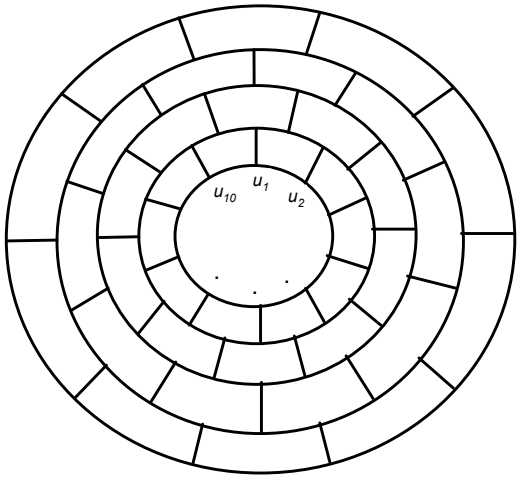

Figure 5. The 2D graph of the nanotube $T_Z[n,10]$.

Table 1. The values of Wiener index for special cases

n	Wiener Index
1	4420
2	14047
3	20400
4	3400
5	52100
6	75320
7	133232
8	177771

Theorem 2.

$$W\left(C_{20n+60}\right) = 10(40n^3 + 360n^2 + 310n + 663)/3.$$

Proof. The distance matrix of fullerene C_{20n+60} can be written as a block matrix by the following way, see Figure 4:

Suppose $\{v_1, v_2, \ldots, v_r\}$, $\{u_1, \ldots, u_s\}$ and $\{w_1, \ldots, w_r\}$ be the set of vertices of the left caps, vertices of $T_Z[n, 10]$ and vertices of the second cap, respectively. The distance matrix D can be written in the following form:

$$D = \begin{pmatrix} V & B & W \\ B & U & B \\ W & B & V \end{pmatrix},$$

where V, B and W are distances between vertices of the first cap with the vertices of the first cap, vertices of $T_Z[n, 10]$ and vertices of the right cap. The matrix U is the distance matrix of vertices $\{u_1, \ldots, u_s\}$. In other words, U is the distance matrix of $T_Z[n, 10]$ and this matrix was computed in Theorem 1. It is easy to see that the Wiener index is equal to the half-sum of distances between all pairs of vertices of D. Notice that for any fullerene graph C_{20n+60}, the matrix V is constant. Obviously, the distance matrices B, U and W are dependant to the number of rows in the nanotube $T_Z[n, 10]$. In other words, if W_n and W_{n-1} are the Wiener indices of the fullerenes C_{20n+60} and $C_{20(n-1)+60}$, respectively, then similar to the proof of the Theorem 1, for $n \geq 8$ we have:

$$\begin{aligned} W_9 - W_8 &= 59700, \\ W_{10} - W_9 &= 69300, \\ W_{11} - W_{10} &= 79700, \\ W_{12} - W_{11} &= 90900, \\ W_{13} - W_{12} &= 102900. \end{aligned}$$

By using a recursive sequence, we have the following formula for the Wiener index of fullerene C_{20n+60}:

$$W_n - W_{n-1} = 400n^2 + 1200n + 7700.$$

If we solve this recursive sequence then, the resulted values represent the Wiener index:

$$W\left(C_{20n+60}\right) = 10(40n^3 + 360n^2 + 310n + 663)/3.$$

The Wiener index of C_{20n+60} for $n = 0, \ldots, 7$ is also reported in Table 2 and this completes the proof of the Theorem.

In the third column of table 2, the boiling pont of a series of fullerenes C_{20n+60}, for $n = 0, \ldots, 8$ is listed. These values are obtained by ACD/LABS software [16]. One can see that there is a correlation of $R = 0.913$ between the values of Wiener index and the boiling point of fullerene C_{20n+60}. This result is mainly because the distances in the molecules are related to the molecular size.

Table 2. The Wiener index of C_{20n+60}, for n = 0, …, 8.

n	W	*BP*
0	11089	849
1	17600	1017
2	30770	1296
3	48625	1417
4	71800	1530
5	100870	1635
6	136455	1735
7	179320	1829
8	230210	1933

CONCLUSIONS

The Wiener index, representing the sum of distances of a connected graph, provided good correlation with some size-dependent physic-chemical or biological properties. In the present paper, we computed, by a recursive method, the Wiener index of an infinite class of fullerenes and tested its correlating ability with the (computed) boiling point of these fullerenes.

REFERENCES

1. A.A. Dobrynin, R. Entringer, I. Gutman, *Acta Appl. Math*., **2001**, *66*, 211.
2. A.A. Dobrynin, L.S. Melnikov, *MATCH Commun. Math. Comput. Chem*., **2004**, *50*, 145.
3, I. Gutman, *Indian J. Chem*., **1997**, *36A*, 128.
4. S. Klavžar, I. Gutman, *Discrete Appl. Math*., **1997**, *80*, 73.
5. H.Y. Zhu, D.J. Klein, I. Lukovits, *J. Chem. Inf. Comput. Sci*., **1996**, *36*, 420.
6. H. Wiener, *J. Am. Chem. Soc*., **1947**, *69*, 17.
7. N. Trinajstić, *Chemical Graph Theory*, CRC Press, Boca Raton, FL, **1992**.
8. M.V. Diudea, M. Stefu, B. Pârv, P.E. John, *Croat. Chem. Acta,* **2004**, *77*, 111.
9. P.E. John, M.V. Diudea, *Croat. Chem. Acta,* **2004**, *77*, 127.
10. A. Graovac, O. Ori, M. Faghani, A.R. Ashrafi, *Fullerene Nanotubes Carbon Nanostruct.*, **2011**, accepted.
11. I. Gutman, *Graph Theory Notes N.Y*., **1994**, *27*, 9.
12. I. Gutman, A.A. Dobrynin, *Graph Theory Notes N.Y*., **1998**, *34*, 37.

13. H.W. Kroto, J.R. Heath, S.C. Obrien, R.F. Curl, R.E. Smalley, *Nature,* **1985**, *318*, 162.
14. H.W. Kroto, J.E. Fichier, D.E. Cox, *The Fullerene*, Pergamon Press, New York, **1993**.
15. H. Zhang, D. Ye, *J. Math. Chem.*, **2007**, *41*, 123.
16. ACD/HNMR Predictor, version 7.03, *Advanced Chemistry Development, Inc.*, Toronto, ON, Canada, www.acdlabs.com, **2012**.

STUDIA UBB CHEMIA, LVIII, 1, 2013 (p. 51 – 61)
(RECOMMENDED CITATION)

LAPLACIAN AND MODIFIED LAPLACIAN MATRICES FOR QUANTIFICATION OF CHEMICAL STRUCTURES

MADIAN RAFAILĂ[a], MIHAI MEDELEANU[a*], CORNELIU DAVIDESCU[a], MIRCEA V. DIUDEA[b]

ABSTRACT. The paper presents the application of Laplacian matrix and its modifications in the characterization of the chemical graphs associated to chemical structures. The eigenvalues of these matrices and some derived topological descriptors were computed. The alkane series C_3 to C_9 was used as the benchmark set in the ordering/discriminating analysis as well as in the QSPR with the normal boiling points.

Keywords: *graphs, Laplacian matrix, chemical structure, topological indices, QSPR*

INTRODUCTION

The chemical formula of a given molecule contains a lot of information which can be directly or, by computational methods, related to topological [1], geometrical [2] and quantum [3,4] descriptors. The basic level of the structural information is the topological one, when the molecule is reduced to a mathematical object called graph *G*, that is a collection of vertices (atoms) and edges (bonds) of the hydrogen depleted molecule (the "molecular" graph [1]). The main relation between the vertices of *G* is the connectivity and, in a first approximation, the nature of atoms is not important. As chemical structures, the molecules have some properties (physical, chemical and biological). At this basic level of molecular modeling, these properties can be correlated with various computed parameters, local and global invariants, the last ones also called topological indices TIs. The topological indices can be computed directly from the molecular graphs [5,6] or better from some matrices associated to molecular graphs [7]. Among the many global invariants calculable from the

[a] *University Politehnica of Timisoara, Faculty of Industrial Chemistry and Environmental Engineering, C. Telbisz Str. No. 6, 300001, Timisoara, Romania*
[b] *Babes-Bolyai University, Faculty of Chemistry and Chemical Engineering, Arany Janos Str. No. 11, 400028 Cluj, Romania*
** Corresponding author: mihai.medeleanu@chim.upt.ro*

topological matrices, the eigenvalues and eigenvectors of the adjacency matrix **A**(*G*) [8-10] or the distance matrix **D**(*G*) [11,12] are the most studied. Another matrix used to characterize the molecular graphs is the Laplacian matrix **L**(*G*)[13].

Recall the definition of these square matrices of $n \times n$ elements:

$$[\mathbf{A}(\mathrm{G})]_{ij} = \begin{cases} 1 & \text{if} \quad i \neq j \quad \text{and} \quad (i,j) \in E(G) \\ 0 & \text{if} \quad i = j \quad \text{or} \quad (i,j) \notin E(G) \end{cases} \tag{1}$$

$$\left[\mathbf{D}(G)\right]_{ij} = \begin{cases} \min l(p_{i,j}), \text{if} \quad i \neq j \\ 0 \ \text{if} \quad i = j \end{cases} \tag{2}$$

$$\mathbf{L}(G) = \mathbf{V}(G) - \mathbf{A}(G) \tag{3}$$

In (2) $min\ l(p_{i,j}) = d_{i,j}$ is the minimum length of the path $p_{i,j}$ that joints the atoms *i* and *j*, or the topological distance $d_{i,j}$ measured in the number of edges/bonds on the shortest path between the two atoms. In (3) V(G) is the diagonal matrix of atom valences and **A** is the adjacency matrix.

Let *G* be a graph on 5 vertices/atoms (the molecular graph of 2-Methylbutane, numbered according to IUPAC rules) and **A** the corresponding adjacency matrix (Figure 1); we have the Laplacian matrix **L**(*G*) as in Figure 1, right.

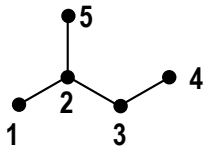

$$\mathbf{A} = \begin{array}{c} \\ \\ \\ \\ \\ \text{sum} \end{array} \left\| \begin{array}{ccccc} 0 & 1 & 0 & 0 & 0 \\ 1 & 0 & 1 & 0 & 1 \\ 0 & 1 & 0 & 1 & 0 \\ 0 & 0 & 1 & 0 & 0 \\ 0 & 1 & 0 & 0 & 0 \end{array} \right\| \begin{array}{c} 1 \\ 3 \\ 2 \\ 1 \\ 1 \end{array} \qquad \mathbf{L} = \left\| \begin{array}{ccccc} 1 & -1 & 0 & 0 & 0 \\ -1 & 3 & -1 & 0 & -1 \\ 0 & -1 & 2 & -1 & 0 \\ 0 & 0 & -1 & 1 & 0 \\ 0 & -1 & 0 & 0 & 1 \end{array} \right\|$$

Figure 1. A graph on 5 vertices/atoms (2-methylbutane, left) and it's adjacency A (middle) and Laplacian L (right) matrices

Let now consider the remote valences *V*(*r*) as the number of neighbors at distance *d*(*i*,*j*)=*r*, *r*=1,2,...*d*(*G*), where *d*(*G*) is the largest distance in *G*. The sums on the rows of the remote adjacency matrix $\mathbf{A}_r(G)$ are just the *remote valences*. The corresponding graphs/subgraphs can be connected or not. Figure 2 shows examples for the graph associated to 2,3-Dimethylpentane. The matrices $\mathbf{A}_r(G)$ (and their powers) were used to define some others one, mainly based on **L**(*G*) matrix definition[14].

The spectrum *Sp*(**M**) represents the collection of all eigenvalues of the matrix **M**(*G*) (or the solutions of its related polynomial *P*(**M**,*x*)).

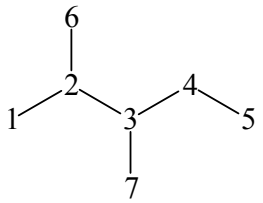

2,3-Dimethylpentane

A_1

	1	2	3	4	5	6	7	*Sum*
1	0	1	0	0	0	0	0	1
2	1	0	1	0	0	1	0	3
3	0	1	0	1	0	0	1	3
4	0	0	1	0	1	0	0	2
5	0	0	0	1	0	0	0	1
6	0	1	0	0	0	0	0	1
7	0	0	1	0	0	0	0	1

A_2

	1	2	3	4	5	6	7	*Sum*
1	0	0	1	0	0	1	0	2
2	0	0	0	1	0	0	1	2
3	1	0	0	0	1	1	0	3
4	0	1	0	0	0	0	1	2
5	0	0	1	0	0	0	0	1
6	1	0	1	0	0	0	0	2
7	0	1	0	1	0	0	0	2

A_3

	1	2	3	4	5	6	7	*Sum*
1	0	0	0	1	0	0	1	2
2	0	0	0	0	1	0	0	1
3	0	0	0	0	0	0	0	0
4	1	0	0	0	0	1	0	2
5	0	1	0	0	0	0	1	2
6	0	0	0	1	0	0	1	2
7	1	0	0	0	1	1	0	3

A_4

	1	2	3	4	5	6	7	*Sum*
1	0	0	0	0	1	0	0	1
2	0	0	0	0	0	0	0	0
3	0	0	0	0	0	0	0	0
4	0	0	0	0	0	0	0	0
5	1	0	0	0	0	1	0	2
6	0	0	0	0	1	0	0	1
7	0	0	0	0	0	0	0	0

Figure 2. Remote adjacency matrices for the graph of 2,3-dimethylpantane

In this paper, the eigenvalues of **L**(*G*) and its modifications (and some topological indices) were computed on the graphs representing 73 alkanes C_3 to C_9. The calculated TIs were correlated with the values of their boiling points at normal pressure.

RESULTS AND DISCUSSION

Modified matrices and topological indices

Let G be an acyclic graph (tree) with *N* vertices, and **A**, **D**,and **L** the matrices described above. Applying the same method used to define the Laplacian **L** we define the modified laplacian $\mathbf{L_k}$ as follows:

Let $\mathbf{A_k}$ be the k^{th} power of the adjacency matrix:

$$\mathbf{A_k} = \mathbf{A}\times\mathbf{A}\times\mathbf{...}\times\mathbf{A} \ , \ k \text{ times} \tag{4}$$

Let v_k be the vertex valence obtained from $\mathbf{A_k}$ and the corresponding diagonal matrix $\mathbf{V_k}$:

$$\mathbf{V}_k = \{v_{k\,i,j}\} = \begin{cases} 0, & \text{if } i \neq j \\ \sum_{j=1}^{n} a_{k\,i,j}, & \text{if } i = j \end{cases} \tag{5}$$

The modified Laplacian:

$$\mathbf{L}_k = \mathbf{V}_k - \mathbf{A} \tag{6}$$

The matrices $\mathbf{L}_k$ (k=1 to 4) and the eigenvalues and their sum for each graph of the selected alkanes were computed. A first set of topological indices are defined in Table 1. Recall that the first eigenvalue of the Laplacian matrix has already been used to characterize some graph properties [15].

Table 1. New topological indices defined on $\mathbf{L}_k$ matrices: k=1 to 4

No	Definition	TI
1	Le_k	First eigenvalue of L_k matrix
2	Se_k	Sum of all eigenvalues of L_k matrix
3	La_k=Sum(Le_k);$_{k=1\text{ to }4}$	Sum al all first eigenvalues (k=1 to 4)
4	Sa_k=Sum(Se_k);$_{k=1\text{ to }4}$	Sum of all sums (k=1 to 4)

Another way to derive molecular descriptors for the characterization of topological structure of the chemical compounds is based on the remote adjacency matrix $\mathbf{A}_r$ [14] (see above). The algorithm is similar to that described for modified Laplacian matrices $\mathbf{L}_k$ but instead of the powers of **A** matrix we use the corresponding remote adjacency matrices $\mathbf{A}_r$ and the diagonal remote valence $\mathbf{V}_r$ matrix. The new modified Laplacian matrices $\mathbf{L}_r$ are:

$$\mathbf{L}_r = \mathbf{V}_r - \mathbf{A}_r \tag{7}$$

where r represent the r^{th} modification of the Laplacian matrix and r$\in$[1, d_{max}] with d_{max} being a maximum chosen distance in G. Obviously, for r=1, the classical Laplacian matrix $\mathbf{L}(G)$ is recovered.

On $\mathbf{L}_r$ matrix and its eigenvalues λ_i, a new topological index was defined:

$$LaR = \sum_{r=1}^{d_{\max}} \sum_{i=1}^{n} (\lambda_i)^r \tag{8}$$

Note that Diudea [16] computed this index up to $d_{max}=d(G)$, with $d(G)$ being the diameter of the graph (i.e. the largest distance in G). On the other hand, the LaR index values increase with the distance in a graph, so, for large graphs the values became too big to be used in correlations or in topological analysis. We tried some normalizations of this index:

$$LaRd = \frac{LaR}{d_{\max}} \tag{9}$$

$$LaRnd = \frac{LaR}{n \cdot d_{\max}} \tag{10}$$

$$LaRl = \log(LaR) \tag{11}$$

All the computed TIs for the alkanes C_3 to C_9 are listed in Table 2.

Table 2. The topological indices as defined in Table 1 and formulae (9) - (12)

Nr.	Alkane	bp °C	Le1	Se1	Le2	Se2	Le3	Se3	Le4	Se4	La	Sa	LaR	LaRd	LaRnd	LaRl
1	C3	-44.5	3.00	4.00	3.41	6.00	4.73	8.00	5.41	12.00	16.56	30.00	8	4.00	1.33	0.903
2	C4	-0.5	3.41	6.00	4.41	10.00	6.30	16.00	9.24	26.00	23.37	58.00	22	7.33	1.83	1.342
3	2-M-C3	-10.5	4.00	6.00	4.73	12.00	9.46	18.00	10.73	36.00	28.93	72.00	24	12.00	3.00	1.380
4	C5	36.5	3.62	8.00	5.11	14.00	7.53	24.00	12.58	42.00	28.84	88.00	54	13.50	2.70	1.732
5	2M-C4	27.9	4.17	8.00	5.56	16.00	10.53	28.00	15.25	54.00	35.52	106.00	58	19.33	3.87	1.763
6	22MM-C3	9.5	5.00	8.00	6.00	20.00	16.32	32.00	18.00	80.00	45.32	140.00	56	28.00	5.60	1.748
7	C6	68.7	3.73	10.00	5.46	18.00	8.44	32.00	14.24	58.00	31.88	118.00	118	23.60	3.93	2.072
8	3M-C5	63.2	4.30	10.00	6.28	20.00	11.60	38.00	19.56	74.00	41.75	142.00	122	30.50	5.08	2.086
9	2M-C5	60.2	4.21	10.00	6.06	20.00	11.50	36.00	18.44	72.00	40.21	138.00	158	39.50	6.58	2.199
10	23MM-C4	58.1	4.56	10.00	6.56	22.00	12.27	42.00	22.18	86.00	45.58	160.00	126	42.00	7.00	2.100
11	22MM-C4	49.7	5.09	10.00	6.74	24.00	17.34	44.00	23.29	102.00	52.46	180.00	128	42.67	7.11	2.107
12	C7	98.4	3.80	12.00	5.64	22.00	9.12	40.00	15.51	74.00	34.07	148.00	258	43.00	6.14	2.412
13	3E-C5	93.5	4.41	12.00	7.05	24.00	12.66	48.00	24.36	96.00	48.49	180.00	330	82.50	11.79	2.519
14	3M-C6	91.8	4.33	12.00	6.53	24.00	12.55	46.00	20.88	92.00	44.29	174.00	254	50.80	7.26	2.405
15	2M-C6	90	4.23	12.00	6.18	24.00	11.57	44.00	19.49	88.00	41.48	168.00	434	86.80	12.40	2.637
16	23MM-C5	89.8	4.63	12.00	7.17	26.00	13.29	52.00	26.40	108.00	51.48	198.00	276	69.00	9.86	2.441
17	33MM-C5	86	5.16	12.00	7.46	28.00	18.36	56.00	28.55	126.00	59.53	222.00	242	60.50	8.64	2.384
18	223MMM-C4	80.9	5.26	12.00	7.65	30.00	18.40	60.00	31.17	138.00	62.48	240.00	246	82.00	11.71	2.391
19	24MM-C5	80.5	4.41	12.00	6.86	26.00	12.66	48.00	24.25	104.00	48.18	190.00	404	101.00	14.43	2.606
20	22MM-C5	79.2	5.10	12.00	7.12	28.00	18.32	52.00	26.39	122.00	56.93	214.00	406	101.50	14.50	2.609
21	C8	125.8	3.85	14.00	5.75	26.00	9.46	48.00	16.44	90.00	35.49	178.00	526	75.14	9.39	2.721
22	3E-C6	118.9	4.44	14.00	7.19	28.00	13.59	56.00	25.43	114.00	50.64	212.00	674	134.80	16.85	2.829
23	3M-C7	118.8	4.34	14.00	6.58	28.00	12.61	54.00	21.86	108.00	45.39	204.00	606	101.00	12.63	2.782
24	34MM-C6	118.7	4.69	14.00	7.52	30.00	14.28	62.00	28.16	130.00	54.64	236.00	458	91.60	11.45	2.661
25	3E-3M-C5	118.2	5.24	14.00	8.22	32.00	19.37	68.00	34.36	152.00	67.18	266.00	518	129.50	16.19	2.714
26	4M-C7	117.7	4.36	14.00	6.69	28.00	13.49	54.00	22.10	110.00	46.65	206.00	520	86.67	10.83	2.716
27	2M-C7	117.6	4.23	14.00	6.22	28.00	11.58	52.00	20.43	104.00	42.46	198.00	1258	209.67	26.21	3.100
28	3E-2M-C5	115.6	4.69	14.00	7.93	30.00	14.30	62.00	31.26	132.00	58.19	238.00	804	201.00	25.13	2.905
29	23MM-C6	115.3	4.64	14.00	7.28	30.00	13.92	60.00	27.44	126.00	53.28	230.00	620	124.00	15.50	2.792
30	233MMM-C5	114.6	5.32	14.00	8.30	34.00	19.42	72.00	36.38	164.00	69.43	284.00	464	116.00	14.50	2.667
31	234MMM-C5	113.4	4.81	14.00	7.98	32.00	14.59	66.00	33.25	144.00	60.62	256.00	596	149.00	18.63	2.775
32	33MM-C6	112	5.17	14.00	7.65	32.00	19.34	64.00	29.74	146.00	61.90	256.00	552	110.40	13.80	2.742
33	223MMM-C5	110.5	5.28	14.00	8.15	34.00	19.39	70.00	35.34	162.00	68.15	280.00	598	149.50	18.69	2.777
34	24MM-C6	109.4	4.48	14.00	7.07	30.00	13.54	58.00	25.36	124.00	50.44	226.00	712	142.40	17.80	2.852
35	25MM-C6	108.4	4.34	14.00	6.51	30.00	11.81	56.00	21.25	118.00	43.91	218.00	1382	276.40	34.55	3.141
36	22MM-C6	107	5.10	14.00	7.16	32.00	18.33	60.00	27.41	138.00	58.00	244.00	1464	292.80	36.60	3.166
37	2233MMMM-C4	106	5.65	14.00	8.65	38.00	20.23	80.00	41.14	194.00	75.65	326.00	434	144.67	18.08	2.637
38	224MMM-C5	99.3	5.12	14.00	7.79	34.00	19.31	64.00	32.19	156.00	64.42	268.00	928	232.00	29.00	2.968
39	C9	150.6	3.88	16.00	5.81	30.00	9.64	56.00	17.12	106.00	36.45	208.00	1100	137.50	15.28	3.041

Nr.	Alkane	bp °C	Le1	Se1	Le2	Se2	Le3	Se3	Le4	Se4	La	Sa	LaR	LaRd	LaRnd	LaRl
40	33EE-C5	146.2	5.30	16.00	9.03	36.00	20.39	80.00	40.26	180.00	74.98	312.00	1292	323.00	35.89	3.111
41	3E-C7	143	4.44	16.00	7.20	32.00	13.65	64.00	26.40	130.00	51.70	242.00	1710	285.00	31.67	3.233
42	3M-C8	143	4.35	16.00	6.59	32.00	12.61	62.00	22.21	124.00	45.76	234.00	1558	222.57	24.73	3.193
43	4M-C8	142.5	4.37	16.00	6.72	32.00	13.53	62.00	22.98	126.00	47.61	236.00	1000	142.86	15.87	3.000
44	2M-C8	142.5	4.23	16.00	6.23	32.00	11.58	60.00	20.47	120.00	42.52	228.00	3586	512.29	56.92	3.555
45	3E-23MM-C5	141.6	5.38	16.00	9.07	38.00	20.43	84.00	42.26	192.00	77.14	330.00	1084	271.00	30.11	3.035
46	2334MMMM-C5	141.5	5.45	16.00	9.11	40.00	20.48	88.00	44.25	204.00	79.28	348.00	876	219.00	24.33	2.943
47	4E-C7	141.2	4.46	16.00	7.30	32.00	14.53	64.00	26.49	132.00	52.77	244.00	1412	235.33	26.15	3.150
48	3E-3M-C6	140.6	5.24	16.00	8.33	36.00	20.35	76.00	35.39	172.00	69.32	300.00	1040	208.00	23.11	3.017
49	23MM-C7	140.5	4.64	16.00	7.29	34.00	13.96	68.00	28.39	142.00	54.29	260.00	1656	276.00	30.67	3.219
50	334MMM-C6	140.5	5.34	16.00	8.58	38.00	20.40	82.00	37.78	188.00	72.10	324.00	848	169.60	18.84	2.928
51	4E-3M-C6	140.4	4.74	16.00	8.11	34.00	15.29	72.00	32.37	154.00	60.51	276.00	1198	239.60	26.62	3.078
52	2233MMMM-C5	140.3	5.68	16.00	9.23	42.00	21.23	92.00	46.32	222.00	82.45	372.00	878	219.50	24.39	2.943
53	34MM-C7	140.1	4.70	16.00	7.58	34.00	14.90	70.00	29.17	148.00	56.34	268.00	936	156.00	17.33	2.971
54	234MMM-C6	139	4.85	16.00	8.15	36.00	15.42	76.00	34.31	166.00	62.72	294.00	990	198.00	22.00	2.996
55	3E-2M-C6	138	4.70	16.00	8.00	34.00	14.95	70.00	32.28	150.00	59.94	270.00	1930	386.00	42.89	3.286
56	233MMM-C6	137.7	5.33	16.00	8.40	38.00	20.38	80.00	37.41	184.00	71.52	318.00	986	197.20	21.91	2.994
57	33MM-C7	137.3	5.17	16.00	7.67	36.00	19.35	72.00	30.70	162.00	62.89	286.00	1686	281.00	31.22	3.227
58	3E-24MM-C5	136.7	4.87	16.00	8.79	36.00	15.60	76.00	38.19	170.00	67.45	298.00	1822	455.50	50.61	3.261
59	35MM-C7	136	4.52	16.00	7.21	34.00	13.79	68.00	26.47	144.00	52.00	262.00	1096	182.67	20.30	3.040
60	25MM-C7	136	4.41	16.00	6.73	34.00	12.72	66.00	22.95	138.00	46.81	254.00	2238	373.00	41.44	3.350
61	26MM-C7	135.2	4.30	16.00	6.39	34.00	11.67	64.00	21.55	134.00	43.91	248.00	5110	851.67	94.63	3.708
62	44MM-C7	135.2	5.18	16.00	7.79	36.00	20.32	72.00	30.89	166.00	64.18	290.00	1078	179.67	19.96	3.033
63	4E-2M-C6	133.8	4.54	16.00	7.48	34.00	14.55	68.00	27.17	146.00	53.74	264.00	1764	352.80	39.20	3.246
64	3E-22MM-C5	133.8	5.30	16.00	8.87	38.00	20.37	80.00	40.21	188.00	74.76	322.00	1730	432.50	48.06	3.238
65	24MM-C7	133.5	4.49	16.00	7.12	34.00	14.46	66.00	26.35	142.00	52.43	258.00	1780	296.67	32.96	3.250
66	2234MMMM-C5	133	5.33	16.00	8.89	40.00	20.37	84.00	42.19	200.00	76.78	340.00	1224	306.00	34.00	3.088
67	22MM-C7	132.7	5.10	16.00	7.17	36.00	18.33	68.00	28.33	154.00	58.93	274.00	5680	946.67	105.19	3.754
68	223MMM-C6	131.7	5.28	16.00	8.20	38.00	19.41	78.00	36.35	180.00	69.25	312.00	1724	344.80	38.31	3.237
69	235MMM-C6	131.3	4.69	16.00	7.53	36.00	14.74	72.00	28.68	158.00	55.63	282.00	1710	342.00	38.00	3.233
70	244MMM-C6	126.5	5.20	16.00	8.08	38.00	20.32	76.00	33.39	180.00	66.98	310.00	1286	257.20	28.58	3.109
71	224MMM-C6	126.5	5.13	16.00	7.89	38.00	19.32	74.00	33.22	176.00	65.55	304.00	2018	403.60	44.84	3.305
72	225MMM-C6	124	5.10	16.00	7.27	38.00	18.35	72.00	28.45	168.00	59.17	294.00	3974	794.80	88.31	3.599
73	2244MMMM-C5	122.7	5.30	16.00	8.66	42.00	20.39	80.00	40.13	210.00	74.49	348.00	1886	471.50	52.39	3.276

Alkane branching ordering

In a topological analysis, the above defined indices were tested for the branching ordering of graphs. Various ordering of alkanes was reported by Bertz [17], Balaban [18] and others. For instance, the C_7 alkanes (all heptanes) are ordered in an identical way by both Bertz and Balaban J-index. Differences appear in the set of C_8 (all octanes): the J index induces a permutation of values: 2,2-2,3-3,4-dimethyl instead of 2,3-3,4-2,2-dimethyl in comparison to the Bertz index. Our indices reproduce the Bertz ordering for C_7 alkanes and dimethyl-C_6 alkanes. Tables 3 and 4 list these alkanes together with their J-index, Le_k indices, two of sum indices (Se4 and Sa) and LaR index.

Analyzing the data in Tables 3 and 4, one observes that LaR index is not suitable for the branching study due to the random ordering. On the other hand, the values of LaR index increase with the maximum distance taken in computation and also with the degree of branching. The other three indices obtained from LaR have a similar behavior as the original index. This interesting behavior of LaR index and its derivatives is under study and will be analyzed in a further paper [19]. Among the other indices, the first eigenvalue of the second modified Laplacian matrix (Le2) induces the same ordering of heptanes as J index and Bertz index. For dimethyl-hexanes, the same index Le2 behaves similarly to J index, with one permutation in comparison to the Bertz results.

Other two indices (Le1 and Le3) based on the first eigenvalue of corresponding matrices gave the same ordering of the tested molecules as the Bertz data, with a single difference for heptanes: the ordering determined by these indices consider the 3-ethylpentane and 2,4-dimethylpentane as having the same degree of branching (degeneracy of the index values). The same degeneracy is observed in the ordering of heptanes based on the sum of adjacency eigenvalues [10].

The ordering of heptanes based on the fourth index Le4 considers the vicinal branching (2,3-dimethylpentane) as slightly more important than the branching at the given atom (2,2-dimethylpentane). For dimethyl-hexanes one gets another type of inversion: 3,4-2,2-2,3 (compared to the Bertz results: 2,3-3,4-2,2).

Table 3. Topological indices of Heptanes

Alkane	N	J	Le1	Le2	Le3	Le4	La	LaR	Sa	Se4
C7	7	2.448	3.801	5.64	9.12	15.51	34.07	258	148	74
2M-C6	7	2.678	4.228	6.18	11.57	19.49	41.78	434	168	88
3M-C6	7	2.832	4.334	6.53	12.55	20.88	44.29	254	174	92
24-MMC5	7	2.953	4.414	6.86	12.66	24.25	48.18	404	190	104
3E-C5	7	2.992	4.414	7.05	12.66	24.36	48.49	330	180	96
23MM-C5	7	3.144	4.629	7.17	13.29	26.4	51.48	276	198	108
22MM-C5	7	3.155	5.097	7.12	18.32	26.39	56.93	406	214	122
33MM-C5	7	3.360	5.164	7.46	18.36	28.55	59.53	242	222	126
223MMM-C4	7	3.541	5.262	7.65	18.4	31.17	62.48	246	240	138

Table 4. Topological indices of dimethyl-hexanes

Alkane	N	J	Le1	Le2	Le3	Le4	La	LaR	Sa	Se4
2,5-MM-C6	8	2.298	4.34	6.51	11.81	21.25	43.91	1382	218	118
2,4-MM-C6	8	3.099	4.48	7.07	13.54	25.36	50.44	712	226	124
2,3-MM-C6	8	3.171	4.64	7.28	13.92	27.44	53.28	620	230	126
3,4-MM-C6	8	3.293	4.69	7.52	14.28	26.18	54.64	458	236	130
2,2-MM-C6	8	3.112	5.10	7.16	18.33	27.41	58.00	1464	244	138
3,3-MM-C6	8	3.373	5.17	7.65	19.34	29.74	61.90	552	256	146

For the two series of analyzed alkanes, the summative index (Sa – the sum of all first eigenvalues of the $\mathbf{L_k}$ matrices, k=1,2,…,4) as well as Se4 index provide the same ordering as that given by the Bertz theory. One can conclude that all these matrices encode information about size and branching of molecular graphs, as already stated by other authors[15,20].

The indices based on the sum of eigenvalues of $\mathbf{L_k}$ matrices show degeneracy (especially Se and Se2) and they could not be analyzed in the same manner as those corresponding to first eigenvalues. Important exceptions are Sa and Se4 which show only one inversion in heptanes ordering (3-ethylpentane is less branched than 2,4-dimethylpentane), the dimethyl-hexanes ordering being the normal one.

Correlating ability

Despite their ability to discriminate the alkane isomers, the computed topological indices give poor correlation with the normal boiling point of these compounds, similar with the J index (frequently used to discriminate isomers). In correlational studies on chemical or physical properties, the J index is used together with the number of atoms (N) meaning that this index expresses more the shape than the size of molecules. A first statistical analysis is done to determine if there is any correlation between the number of atoms in the set of 73 molecules and our topological indices. The data on correlation between N and topological indices based on the first eigenvalue and of LaR type indices are listed in Table 5.

Table 5. Intercorrelation data

	N	LaR	LaRd	LaRnd	LaRl	Le1	Le2	Le3	Le4	La
N	1.000	0.583	0.610	0.927	0.952	0.548	0.736	0.576	0.693	0.674
LaR	0.583	1.000	0.973	0.763	0.756	0.180	0.204	0.204	0.206	0.209
LaRd	0.610	0.973	1.000	0.809	0.772	0.307	0.343	0.329	0.352	0.351
LaRnd	0.927	0.763	0.809	1.000	0.983	0.570	0.692	0.582	0.658	0.652
LaRl	0.952	0.756	0.772	0.983	1.000	0.472	0.620	0.494	0.575	0.566
Le1	0.548	0.180	0.307	0.570	0.472	1.000	0.897	0.982	0.905	0.952
Le2	0.736	0.204	0.343	0.692	0.620	0.897	1.000	0.885	0.987	0.979
Le3	0.576	0.204	0.329	0.582	0.494	0.982	0.885	1.000	0.895	0.950
Le4	0.693	0.206	0.352	0.658	0.575	0.905	0.987	0.895	1.000	0.990
La	0.674	0.209	0.351	0.652	0.566	0.952	0.979	0.950	0.990	1.000

One can see that none of the indices based on the first eigenvalue of Laplacian and modified Laplacian (Le_k) matrices show a significant correlation with the number of atoms N (i.e. the size of molecules). The value 1.00 is obtained in case of the sum of eigenvalues of the Laplacian matrix, this index clearly encoding the molecular size.

Stronger correlations are between the sum of eigenvalues (La) and the Le1, Le2, Le3, Le4 indices which means that these indices encode similar information and cannot be used together in correlations. The correlation coefficients for the dependency of N with sum indices (Se_k) lie between 0.80 and 1.00.

Among all the computed indices, the best monovariate linear correlation is obtained in case of the logarithm of LaR index (i.e. LaRl index):

$$\mathrm{BP} = 68.000(\pm 3.404) \cdot LaRl - 81.512(\pm 8.393)$$

N=73, R=0.9214, R^2=0.8490, adj R^2=0.8468, F(1,71)=399.05, s=15.84 (12)

The correlations of the normal boiling point of alkanes C_3 to C_9 with the Laplacian matrices derived topological indices are listed below.

Le1 $$\mathrm{BP} = 29.130(\pm 0.665) \cdot N - 6.224(\pm 1.7310) \cdot Le1 - 92.469(\pm 6.902)$$ (13)

N=73, R=0.9863, R^2=0.9729, adj R^2=0.9721, F(2,70)=1255.72, s=6.759

Le2 $$\mathrm{BP} = 28.869(\pm 0.878) \cdot N - 1.756(\pm 1.081) \cdot Le2 - 106.989(\pm 5.486)$$ (14)

N=73, R=0.9844, R^2=0.9690, adj R^2=0.9681, F(2,70)=1095.70, s=7.222

Le3 $$\mathrm{BP} = 29.383(\pm 0.666) \cdot N - 0.962(\pm 0.236) \cdot Le3 - 109.116(\pm 4.415)$$ (15)

N=73, R=0.9869, R^2=0.9740, adj R^2=0.9733, F(2,70)=1312.90, s=6.614

Le4 $$\mathrm{BP} = 29.102(\pm 0.810) \cdot N - 0.306(\pm 0.134) \cdot Le4 - 113.107(\pm 4.763)$$ (16)

N=73, R=0.9849, R^2=0.9701, adj R^2=0.9693, F(2,70)=1135.90, s=7.097

La $$\mathrm{BP} = 29.343(\pm 0.774) \cdot N - 0.230(\pm 0.079) \cdot La - 110.870(\pm 4.604)$$ (17)

N=73, R=0.9856, R^2=0.9714, adj R^2=0.9705, F(2,70)=1187.20, s=6.946

LaR $$\mathrm{BP} = 29.208(\pm 0.689) \cdot N - 0.003(\pm 0.0009) \cdot LaR - 118.871(\pm 4.999)$$ (18)

N=73, R=0.9862, R^2=0.9726, adj R^2=0.9718, F(2,70)=1241.1, s=6.798

The contribution of the number of atom is quite the same in all equations. However, the contribution of topological indices is different. The greatest value of the correlation coefficient is obtained for Le1 index. For the rest of indices, the correlation coefficient values are smaller.

Concerning the degeneracy of the computed topological indices, an analysis has been carried out for the set of 73 alkanes and the computed indices listed in Table 2. In the case of the summative type indices (S type) the degeneracy is high except for Sa (sum of all eigenvalues sums) that shows only three pair of degenerated values: compounds 11 and 13 with Sa=180, compounds 24 and 43 with Sa=236 and compounds 31 and 32 with Sa=256. Three indices have no degeneracy within this set: Le2, Le4 and La. The LaR index and the three other indices based on LaR do not degenerate for the 73 alkanes. The Le3 index has two pairs with the same

value: 13 and 19 with Le3=12.6601 and 40 and 73 with 20.3875. The index based on the first eigenvalue of the Laplacian matrix shows the highest degeneracy, with three pairs: 8 and 61 with Le1=4.3028, 13 and 19 with Le1=4.4142, 23 and 35 with Le1=4.3429 and a triple degeneracy: 40, 64 and 73 with Le1=5.3028.

CONCLUSIONS

In this paper, we studied 14 topological indices computed on 73 molecules (alkane isomers of C_3 to C_9). The Laplacian eigenvalue Le and the LaR index were already used as molecular descriptors[14,16]. The eigenvalues of the modified Laplacian matrices have also been used but only to characterize some special graphs [21] and not in correlating studies. We proved here that these indices present a proper behavior in ordering of alkanes, similar to that provided by Bertz index or Balaban's J index, with minor differences.

Using these descriptors as variables in a correlational analysis, no strong intercorrelation between them and the number of atoms in the structures (except the indices based on the sum of eigenvalues) was observed. They can be used in structure – property analysis to describe the molecular branching, together with N (i.e. the number of heavy atoms) with good results.

The degeneracy of the topological indices is not very high for those based on the first eigenvalue. For the sum-type indices this phenomenon is rather present, excepting for Sa.

The LaR index and other normalized indices do not degenerate within the selected set of alkanes.

REFERENCES

1. M.V. Diudea, I. Gutman, L. Jantschi, *Molecular Topology*, Nova Science, **2002**
2. J.C. Cramer, *Essentials of Computational Chemistry. Theories and Models,* Wiley, **2002**, 17-94
3. S.M. Bachrach, *Computational Organic Chemistry*, Wiley, **2007**
4. F. Jensen, *Introduction to Computational Chemistry*, Wiley, **2001**
5. J. Devillers, A.T. Balaban (Eds.), "Topological Indices and Related Descriptors in QSAR and QSPR"*,* Gordon and Breach, Amsterdam, **1999**
6. D. Cvetkovic, P. Rowlinson, S. Simic, "Eigenspaces of Graphs", Cambridge Univ. Press, **1997**
7. D. Cvetkovic, P. Rowlinson, "The Largest Eigenvalue of a Graph: A Survey"*, Lin. Multilin. Algebra*, **1990**, *28*, 3-33
8. L. Lovasz, J. Pelikan, *Period. Math. Hung.*, **1973**, *3*, 175

9. E. Estrada, L. Rodriguez, A. Gutierrez, *Commun. Math. Comput. Chem. (MATCH)*, **1997**, *35*, 145-156
10. A.T. Balaban, D. Ciubotariu, M. Medeleanu, *J. Chem. Inf. Comput. Sci.*, **1991**, *31*, 517
11. B. Zhou, N. Trinajstic, *Chem. Phys. Lett.*, **2007**, *447* (4-6), 384-387
12. Z. Mihalic, S. Nikolic, N. Trinajstic, *J. Chem. Inf. Comput. Sci.,* **1992**, *32*, 28 -37
13. B. Mohar, *Laplacian Matrices of Graphs*, *Prepr. Ser. Dept. Math. Univ. E.K. Ljubljana*, **1988**, *26*, 385-392
14. N. Trinajstic, D. Babic, S. Nicolic, D. Plavšic, D. Amic, Z. Mihalic, *J. Chem. Inf. Comput. Sci.*, **1994** *34*, 368-376
15. I. Gutman, S.L. Lee, C.H. Chu, Y.L. Luo, *Indian J. Chem.*, **1994**
16. M.V. Diudea, *Nanomolecules and Nanostructures - Polynomials and Indices*, MCM series, No. 10, Univ. Kragujevac, Kragujevac, **2010**, *33A*, 603 -608
17. S.H. Bertz, *Discr. Appl. Math*., **1988**, *19*, 65-83
18. A.T. Balaban, *Chem.Phys.Lett.*, **1982**, *89*, 399
19. M. Medeleanu, M.V. Diudea, work in progress
20. I. Gutman, D. Vidovic, D. Stevanovic, *J. Serb. Chem. Soc.,* **2002**, *67*(6), 407-413
21. M. Medeleanu, D. Ciubotariu, M. Mracec, M.V. Diudea, *MATH/CHEM/COMP*, Dubrovnik, **2010**

STUDIA UBB CHEMIA, LVIII, 1, 2013 (p. 63 – 70)
(RECOMMENDED CITATION)

ON OMEGA AND RELATED POLYNOMIALS OF DENDRIMERS

MODJTABA GHORBANI[a*] and MOHAMMAD A. HOSSEINZADEH[b]

ABSTRACT. Omega polynomial was introduced by Diudea. Following Omega polynomial, the Sadhana polynomial was defined by Ashrafi et al. In this paper we compute Omega and Sadhana polynomials of three classes of dendrimers.

Key Words: *Omega, Theta and Sadhana Polynomials, Chain graph, Dendrimer*

INTRODUCTION

Dendrimers are hyper-branched macromolecules, with a rigorously tailored architecture. They have been studied from the topological point of view, including vertex and fragment enumeration and calculation of some topological descriptors, such as topological indices, sequences of numbers or polynomials. In the present work we compute Omega, Theta and Sadhana polynomials of three classes of dendrimers by using the definition of chain graphs [1, 2]. Let G be a simple molecular graph without directed and multiple edges and without loops, the vertex and edge-sets of which being denoted by $V(G)$ and $E(G)$, respectively. Suppose G is a connected molecular graph and $x, y \in V(G)$. The distance $d(x,y)$ between x and y is defined as the length of a minimum path between x and y. Two edges $e = ab$ and $f = xy$ of G are called codistant, "e co f", if and only if $d(a,x) = d(b,y) = k$ and $d(a,y) = d(b,x) = k+1$ or vice versa, for a non-negative integer k. It is easy to see that the relation "co" is reflexive and symmetric but it is not necessary transitive. Set $C(e) := \{f \in E(G) \mid f \text{ co } e\}$. If the relation "co" is transitive on $C(e)$ then $C(e)$ is called an orthogonal cut "oc" of the graph G. The graph G is called co-graph if and only if the edge set $E(G)$ is the union of disjoint orthogonal cuts. Observe *co* is a Θ relation, (*Djoković-Winkler*) [3, 4]:

[a] *Department of Mathematics, Faculty of Science, Shahid Rajaee Teacher Training University, Tehran, 16785-136, I.R. Iran*
[b] *Department of Mathematical Science, Sharif University of Technology, Tehran, 11365-9415, I.R. Iran*
* *Corresponding author: mghorbani@srttu.edu*

$$d(x,u)+d(y,v)\neq d(x,v)+d(y,u)$$

and Θ is a *co*-relation if and only if *G* is a partial cube, as Klavžar [5] correctly stated in a recent paper. Relation Θ is reflexive and symmetric but need not be transitive. Klavžar noted by Θ* the Θ transitive closure, then Θ* is an equivalence (see also the co relation). In this respect, recall some other definitions.

Let $m(G,c)$ be the number of *qoc* strips of length *c* in the graph *G*; for the sake of simplicity, $m(G,c)$ will hereafter be written as *m*. Two counting polynomials have been defined [6–9] on the ground of *qoc* strips, $\Omega(G,x)=\sum_c m\cdot x^c$ and $\Theta(G,x)=\sum_c m\cdot c\cdot x^c$. In a counting polynomial, the first derivative (in x=1) defines the type of property which is counted; for the two polynomials they are $\Omega'(G,1)=\sum_c m\cdot c=e=|E(G)|$ and $\Theta'(G,1)=\sum_c m\cdot c^2$.

The Sadhana index Sd(G) was defined by Khadikar et al [10,11] as $Sd(G)=\sum_c m(G,c)(|E(G)|-c)$, where $m(G,c)$ is the number of strips of length *c*. The Sadhana polynomial $Sd(G,x)$ was defined by Ashrafi et al. [12] as $Sd(G,x)=\sum_c m(G,c)\times x^{|E|-c}$. From the definition of Omega polynomial, one can obtain the Sadhana polynomial by replacing x^c with $x^{|E|-c}$. Then the Sadhana index will be the first derivative of $Sd(G, x)$ evaluated at x = 1. The aim of this study is to compute the Omega and two related polynomials for some special cases of chain graphs. Throughout this paper, our notations are standard and all of graphs are simple and connected. We encourage the reader to consult papers [13 − 21].

RESULTS AND DISCUSSION

In this section we present explicit formulas for the Omega and Sadhana polynomials of some chain graphs. We also encourage the reader to consult [18] for background material, as well as for basic computational techniques. Let G_i's ($1\le I\le k$) be some graphs. A chain graph can be obtained from union of G_i's by joining each v_i to v_{i+1} where $v_i\in G_i$. We denote a chain graph by $G = G(G_1, \ldots, G_k, v_1, \ldots, v_k)$, Figure 1. It is easy to see that $|V(G)|=\sum_{i=1}^{k}|V(G_i)|$, $|E(G)|=(k-1)+\sum_{i=1}^{k}|E(G_i)|$ and the following Lemmas for a chain graph holds:

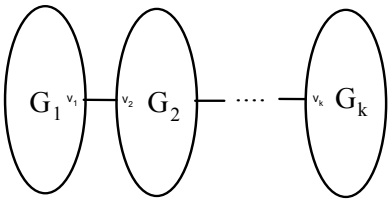

Figure 1. Diagram of a chain graph

Lemma 1. Let $G = G(G_1,...,G_k,v_1,...,v_k)$ be a simple connected chain graph and e$\in$ E(G_1) and f $\in$E(G_2). Then the edges *e* and *f* don't satisfy the "co" relation, in other words, $e \not\odot f$.

Proof. Let $e = ab \in G_1$ and $f = xy \in G_2$ be arbitrary edges. We consider the following cases:

(*i*) $d(a,v_1) = d(b,v_1) = k_1$ and $d(x,v_2) = d(y,v_2) = k_2$. Then

$$d(a,y) = d(a,v_1) + d(v_1,v_2) + d(v_2,y) = k_1 + k_2 + 1$$

and

$d(a,x) = d(a,v_1) + d(v_1,v_2) + d(v_2,x) = k_1 + k_2 + 1$. This implies that $e \not\odot f$.

(*ii*) $d(a,v_1) = d(b,v_1) = k_1$ and $d(x,v_2) = k_2, d(y,v_2) = k_2 + 1$. So,

$$d(a,x) = d(a,v_1) + d(v_1,v_2) + d(v_2,x) = k_1 + k_2 + 1$$

and

$$d(b,x) = d(b,v_1) + d(v_1,v_2) + d(v_2,x) = k_1 + k_2 + 1.$$

This implies that. $e \not\odot f$.

(*iii*) $d(a,v_1) = k_1, d(b,v_1) = k_1 + 1$ and so,

$$d(x,a) = d(x,v_2) + d(v_2,v_1) + d(v_1,a) = k_2 + k_1 + 1$$

and

$$d(y,a) = d(y,v_2) + d(v_2,v_1) + d(v_1,a) = k_2 + k_1 + 1.$$

This implies that $e \not\odot f$.

Lemma 2. Let $G = G(G_1,...,G_k,v_1,...,v_k)$ be a chain graph, $u \in V(G_i)$ and $v \in V(G_j)$ $(1 \le i, j \le k, i \ne j)$. Then

$$d(u,v) = d(u,v_i) + d(v_i,v_j) + d(v_j,v) = d(u,v_i) + d(v_j,v) + | i - j |.$$

Proof. For every $1 \le i, j \le k, i \ne j$, $d(u_i,u_j) = |I - j|$ and this completes the proof.

Theorem 3. Let *G* be a graph with two blocks G_1, G_2 and a cut-edge $uv \in E(G)$ (Figure 2). Then: $\Omega(G,x) = x + \Omega(G_1,x) + \Omega(G_2,x)$.

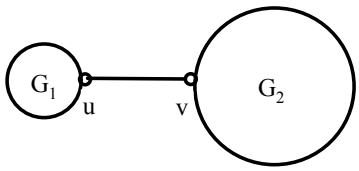

Figure 2. Diagram of a chain graph with two blocks

Proof. By using definition of Omega polynomial and Lemma 1 one can see that

$$\Omega(G,x) = x + \sum_{c_1} m(G_1,c_1)x^{c_1} + \sum_{c_2} m(G_2,c_2)x^{c_2} = x + \Omega(G_1,x) + \Omega(G_2,x).$$

Corollary 4. If $G = G(G_1,...,G_k,v_1,...,v_k)$ is a simple connected chain graph then we have:

$$\Omega(G,x) = (k-1)x + \sum_{i=1}^{k} \Omega(G_i,x).$$

Corollary 5. Let $G = G(G_1,...,G_k,v_1,...,v_k)$ be a chain graph. Then,

$$Sd(G,x) = (k-1)x^{|E(G)|-1} + \sum_{i=1}^{k} \sum_{c_i} m(G_i,c_i)x^{|E(G)|-c_i}.$$

Further, if *G* is a bipartite graph then

$$\theta(G,x) = (k-1)x + \sum_{i=1}^{k} \theta(G_i,x).$$

Theorem **6**. Let *T* be a tree with *n* vertices and

$T = T_n = T(T_{n-1},T_1,v_{n-1},v_1)$. Then $\Omega(T_n,x) = (n-1)x$.

Proof. Let T_{n-1} be a tree with *n*-1 vertices constructed by cutting a pendant vertex *v* of T_n. It is easy to see that T is a chain graph and we can suppose

$T = T_n = G(T_{n-1}, T_1, u, v)$, Figure 3. By cutting a pendant vertex of T_{n-1}, then $T_{n-1} = G(T_{n-2}, T_1, u', v')$ and so on. We have the following equations:

$$\Omega(T_n,x) - \Omega(T_{n-1},x) = x$$
$$\Omega(T_{n-1},x) - \Omega(T_{n-2},x) = x$$
$$\vdots$$
$$\Omega(T_2,x) - \Omega(T_1,x) = x.$$

By summation of these relations one can see that $(T, x) = (n-1)x$.

Example 7. Consider the graph of dendrimer *D* with *n* vertices in Figure 3. Since this graph is a tree with *n* vertices, according to Theorem 6, $\Omega(D,x) = (n-1)x$ and $Sd(D, x) = (n-1)x^{n-2}$. Because a tree is bipartite (and a partial cube) then $\Theta(D, x) = (n-1)x$.

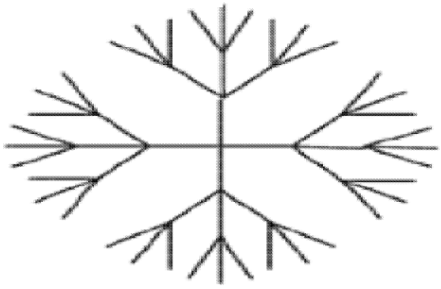

Figure 3. Graph of the dendrimer *D* of *n* = 52

Example 8. Consider the graph of the dendrimer S_1 with *n* vertices, Figure 4. It is easy to see that $\Omega(S_1, x) = 3x + 9x^2$. Now let *S* be a nanostar dendrimer shown in Figure 5. By computing the number of vertices and the number of edges we have $|V(S)| = 19n$ and $|E(S)| = 22n - 1$. Furthermore we can suppose $S = G(N_{n-1}, N_1, v_{n-1}, v_1)$ So we have the following relations:

$$\begin{gathered}\Omega(G_n, x) - \Omega(G_{n-1}, x) = x + \Omega(G_1, x)\\ \Omega(G_{n-1}, x) - \Omega(G_{n-2}, x) = x + \Omega(G_1, x)\\ \vdots\\ \Omega(G_2, x) - \Omega(G_1, x) = x + \Omega(G_1, x)\end{gathered},$$

By Summation of these relations one can easily deduce that $\Omega(S_n, x) - \Omega(S_1, x) = (n-1)x + (n-1)\Omega(S_1, x)$. This implies Omega polynomial of S_n is $\Omega(S_n, x) = (n-1)x + n\Omega(S_1, x)$. Because $\Omega(S_1, x) = 3x + 9x^2$ then, $\Omega(S_n, x) = 9nx^2 + (4n-1)x$ and so Sadhana polynomial is $Sd(S_n, x) = (4n-1)x^{22n-2} + 9nx^{22n-3}$. On the other hand S_n is bipartite and then $\Theta(S_n, x) = 18nx^2 + (4n-1)x$.

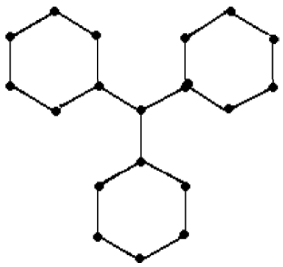

Figure 4. Graph of the dendrimer S_1

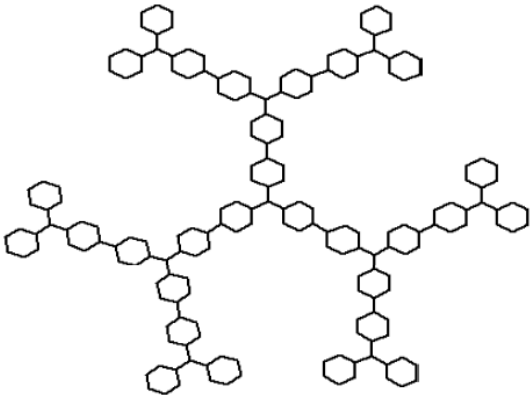

Figure 5. Graph of the nanostar dendrimer S for $n = 3$

Example 9. Now consider the graph H_1 shown in Figure 6. It is easy to see that $\Omega(H\text{-}1, x) = 4x+15x^2$. By using definition of chain graph the graph H_n (Figure 7), it is easy to see that

$$H_n = (H_{n\text{-}1}, H_1; u, v):$$

So, we have the following equations:

$$\Omega(H_n, x) - \Omega(H_{n-1}, x) = x + \Omega(H_1, x)$$
$$\Omega(H_{n-1}, x) - \Omega(H_{n-2}, x) = x + \Omega(H_1, x)$$
$$\vdots$$
$$\Omega(H_2, x) - \Omega(H_1, x) = x + \Omega(H_1, x)$$

By summation of these equations one can see that $\Omega(H_n, x) = (n + 3)x + 15nx^2$. Finally let D be the nanostar dendrimer in Figure 8. Clearly D is a chain graph and $\Omega(D, x) = (4n + 17)x + 4(30n + 3)x^2$. Because $|V(D)| = 120n + 12$ and $|E(D)| = 140n + 13$, then $Sd(D, x) = 4(30n + 3)x^{140n+11} + (4n + 17)x^{140n+12}$ and $\Theta(D, x) = 4(30n + 3)\, x^2 + (4n + 17)x$.

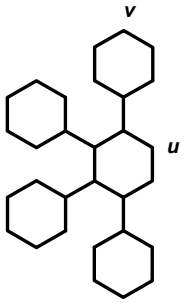

Figure 6. Graph of the nanostar dendrimer H_1

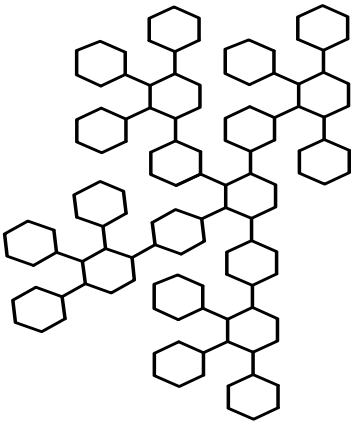

Figure 7. Graph of the nanostar dendrimer H_n

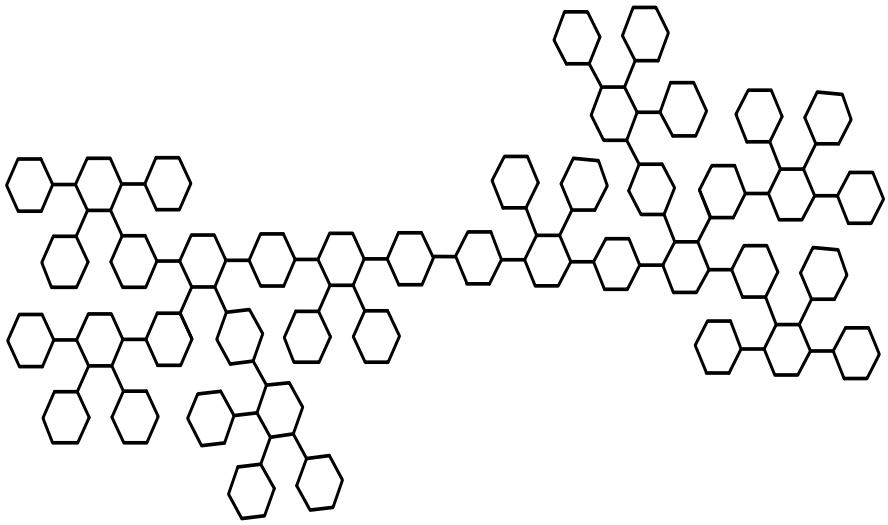

Figure 8. Graph of the nanostar dendrimer *D*

CONCLUSIONS

Nanostar dendrimers can be designed by using the concept of the chain graph. Because of their size, it is difficult to calculate these polynomials in higher generation dendrimers. Formulas for some families of nanostar dendrimers were derived. By this formula we can compute Omega and related polynomials of any nanostructures whose molecular graph is isomorphic to a chain graph.

REFERENCES

1. G.R. Newcome, V.K. Gupta, G.R. Baker, Z.-Q. Yao, *J. Org. Chem.*, **1985**, *50*, 2003.
2. D.A. Tomalia, *Aldrichimica Acta*, **1993**, *26*, 91.
3. D.Ž. Djoković, *J. Combin. Theory Ser. B*, **1973**, *14*, 263.
4. P.M. Winkler, *Discrete Appl. Math*.,**1984**, *8*, 209.
5. S. Klavžar, *MATCH Commun. Math. Comput. Chem.*, **2008**, *59*, 217.
6. P.E. John, A.E. Vizitiu, S. Cigher, M.V. Diudea, *MATCH Commun. Math. Comput. Chem.*, **2007**, *57*, 479.
7. M.V. Diudea, S. Cigher, A.E. Vizitiu, O. Ursu, P.E. John, *Croat. Chem. Acta*, **2006**, *79*, 445.
8. A.E. Vizitiu, S. Cigher, M.V. Diudea, M.S. Florescu, *MATCH Commun. Math. Comput. Chem.*, **2007**, *57*, 457.
9. M.V. Diudea, *Carpath. J. Math.*, **2006**, *22*, 43.
10. P.V. Khadikar, S. Joshi, A.V. Bajaj, D. Mandloi, *Bioorg. Med. Chem. Lett.*, **2004**, *14*, 1187.
11. P.V. Khadikar, V.K. Agrawal, S. Karmarkar, *Bioorg. Med. Chem.*, **2002**, *10*, 3499.
12. A.R. Ashrafi, M. Ghorbani, M. Jalali, *Ind. J. Chem.*, **2008**, *47A*, 535.
13. M. Ghorbani, A. R. Ashrafi, *J. Comput. Theor. Nanosci.*, **2006**, *3*, 803.
14. A.R. Ashrafi, M. Jalali, M. Ghorbani, M.V. Diudea, *MATCH Commun. Math. Comput. Chem.*, **2008**, *60(3*), 905.
15. A.R. Ashrafi, M. Ghorbani, *MATCH Commun. Math. Comput. Chem.*, **2008**, *60*, 359.
16. A.R. Ashrafi, M. Ghorbani, M. Jalali, *Optoelectron. Advan. Mater.- Rapid Commun.*, **2009**, *3(8)*, 823.
17. M. Ghorbani, M. Jalali, *Studia UBB Chemia*, **2009**, *2*, 145.
18. A.R. Ashrafi, M. Ghorbani, *Fullerenes, Nanotubes Carbon Nanostruct.*, **2010**, *18*, 198.
19. M. Ghorbani, M. Jaddi, *Optoelectron. Advan. Mater.- Rapid Commun.*, **2010**, *4(4)*, 540.
20. M. Ghorbani, *Iranian J. Math. Chem.*, **2010**, *1(1)*, 105.
21. M. Ghorbani, *Iranian J. Math. Chem.*, **2011**, *2(2)*, 1.

STUDIA UBB CHEMIA, LVIII, 1, 2013 (p. 71 – 79)
(RECOMMENDED CITATION)

THE ANALYSIS OF COUMARINS FROM *SCOPOLIA CARNIOLICA* JACQ. (*SOLANACEAE*) OF ROMANIAN SPONTANEOUS FLORA

CRISTINA ŞTEFĂNESCU[a], LAURIAN VLASE[a*], MIRCEA TĂMAŞ[a], GIANINA CRISAN[a]

ABSTRACT. Coumarins from *Scopolia carniolica* Jacq. (*Solanaceae*), henbane bell, have been analysed. The qualitative analysis was performed by thin layer chromatography (TLC), scopoletin and two of its glycosides being emphasized. Scopoletin (free and total) was quantitatively determined by LC/MS techniques. The dynamics of coumarin accumulation was analysed in different vegetative organs harvested at 2-4 weeks interval during the vegetation period. The highest amount of free scopoletin was found in the underground organs before fruit maturation, after that period being identified in the aerial parts. The total scopoletin amount, determined after hydrolysis, was up to 70 times higher than the free scopoletin one, indicating that it is preferentially accumulated as glycosides, mostly in the rhizomes and roots.

Keywords: *scopoletin, LC/MS, Scopolia carniolica*

INTRODUCTION

Scopolia carniolica Jacq. like other *Solanaceae* members as *Atropa belladonna*, *Hyosciamus niger*, *Datura stramonium*, is known and used for its tropane alkaloids, atropine and scopolamine, substances with anticholinergic activity upon acetylcholine and muscarinic receptors. The main source of active principles is the underground part – the rhizomes, harvested for industrial extraction purposes. The isolated alkaloids are utilized as muscle relaxants, in preoperative medication or eye exams [**1**]. The plant also contains coumarins (scopoletin), flavonoids, choline, and polyphenols [**2,3**].

Pharmacological studies performed on the coumarin scopoletin (Figure 1) showed antinociceptive, antioxidant, antispasmodic, hypouricemic, hepatoprotective, antiproliferative and antidepressant-like activity [**4-10**]. Scopoletin also showed acetylcholinesterase inhibitory activity which can be used in treating Alzheimer disease [**11**].

[a] *University of Medicine and Pharmacy "Iuliu Haţieganu", Faculty of Pharmacy, Emil Isac 13, RO-400023, Cluj-Napoca, Romania*
* *Corresponding author: vlaselaur@yahoo.com*

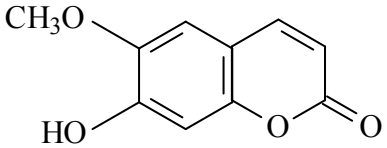

Figure 1. Chemical structure of scopoletin

Considering this promising pharmacological properties for scopoletin, the purpose of the present work was to analyze the vegetative organs of *S. carniolica* harvested from the spontaneous flora of Romania as possible sources for scopoletin extraction.

Literature reports about *Scopolia* genus concern mainly the alkaloid studies and there are few reports concerning the non-alkaloid constituents (coumarins, polyphenolic compounds), especially on *S. lurida* and *S. japonica* [**2**]. One former study on *S. carniolica* presented in literature only indicates the amount of scopoletin and total coumarins in leaves and underground parts of the cultivated species from Poland, quantified by RP-HPLC analysis [**2**].

We aimed to study the dynamics of accumulation of scopoletin in rhizomes, roots, stems and leaves of *S. carniolica*, in order to identify the organ and period when the maximum amount of it could be obtained. The plant samples were harvested at an interval of 2-4 weeks during the vegetation period, from early May to early August.

For the qualitative analysis of scopoletin and other coumarins we have used thin layer chromatography and for the quantitative determination of scopoletin, before and after the sample hydrolysis, high performance liquid chromatography coupled with mass spectrometry was used.

RESULTS AND DISCUSSION

The first step was the TLC identification of scopoletin and coumarin analysis in the plant samples. The samples were rhizomes (Srh), roots (Sra), stems (Sc) and leaves (Sf) harvested in early May (1), middle May (2), early June (3), end of June (4), middle July (5) and early August (6). The samples 2 and 2', 3 and 3', 4 and 4' represented respectively lower and upper stems and leaves. The compounds separated from these samples were compared to standards of scopoletin and umbeliferon (Figure 2 a-d).

By this technique, scopoletin was identified in all samples, except Sf1, Sf2 and Sf2' (afterwards it was identified and quantified in those samples by LC/MS/MS), other three substances (compounds 1, 2 and 3) being also separated.

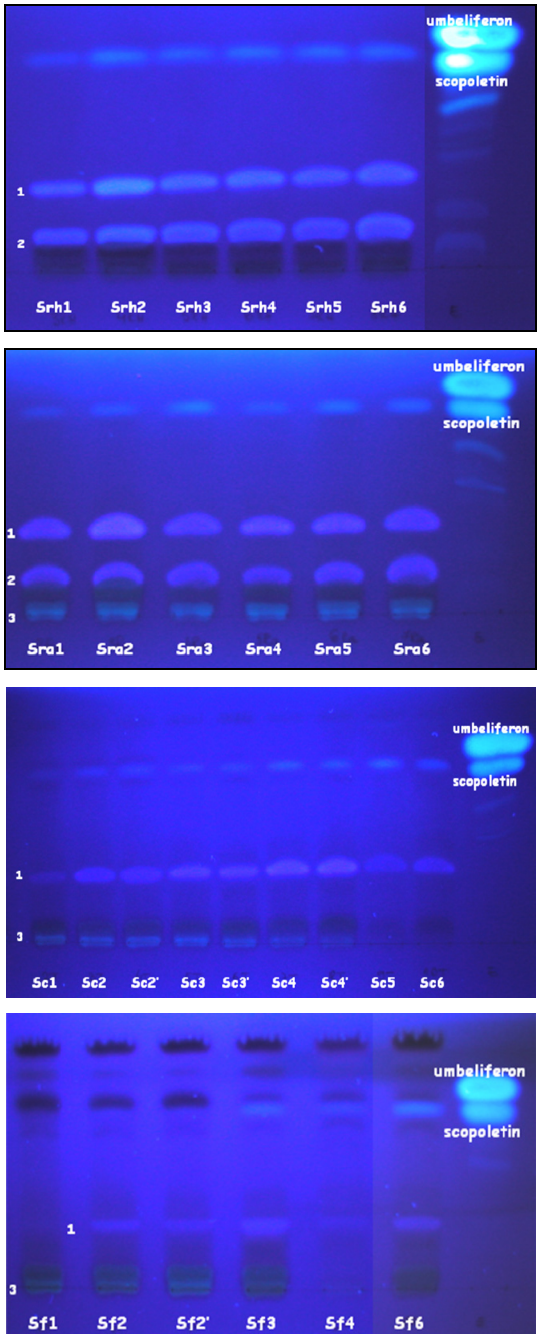

Figure 2. TLC chromatogram of coumarins in *S. carniolica* rhizomes (a), roots (b), stems (c), and leaves (d)

The TLC analysis of compounds 1 and 2 separated by preparative TLC in same analytical conditions as qualitative TLC was performed. The samples were analyzed before and after hydrolysis (H), and compared to the standard of scopoletin and scopoletin isolated by preparative TLC (Sp), the TLC chromatogram being showed in Figure 3. The compounds 1 and 2 are present in samples before hydrolysis and absent in samples after hydrolysis. Instead, in the samples after hydrolysis, scopoletin was identified; therefore we considered them scopoletin glycosides.

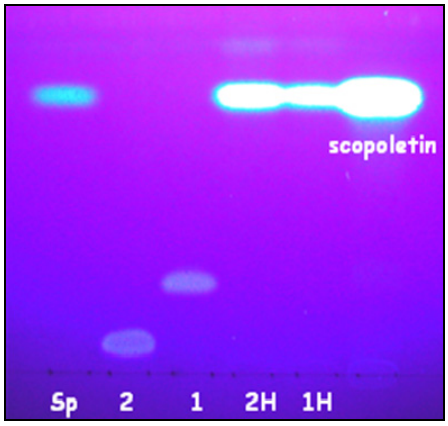

Figure 3. TLC chromatogram of compounds 1 and 2 before and after hydrolysis

Scopoletin (free and total) was quantitatively determined by LC/MS/MS. The plant samples were the same as described for the TLC analysis. The total scopoletin amount was determined in the same samples, but after acid hydrolysis.

The mass spectra of scopoletin is presented in Figure 4. The parent ion, with m/z 193, was fragmented by collision induced dissociations to daughter ions with m/z 133, 137, 149, 165 and 178 (Figure 5); the former ion was chosen for quantification, being the most intense.

The calibration curve of scopoletin was made between 12.8-256 ng/ml (8 concentration levels). For each concentration, the precision and inaccuracy were less than ±5%.

A typical chromatogram of scopoletin at quantification limit (12.8 ng/ml, determined at a signal-to-noise ratio of 10) is shown in Figure 6.

The quantitative results of the amount of scopoletin in analyzed samples are indicated in the charts below (Figure 7).

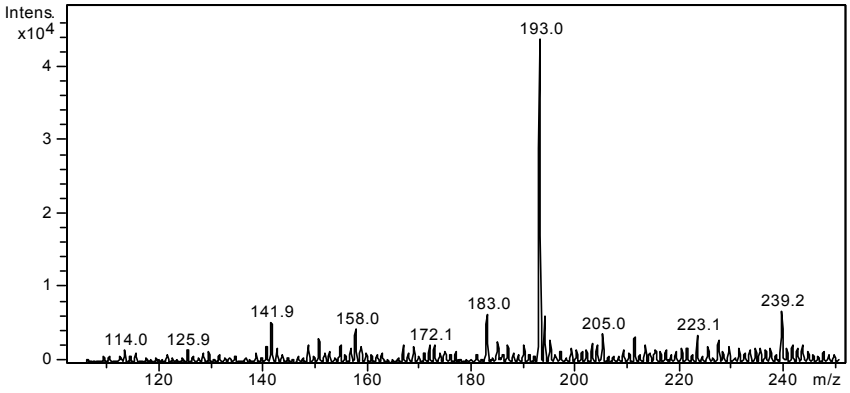

Figure 4. Full scan mass spectra of scopoletin

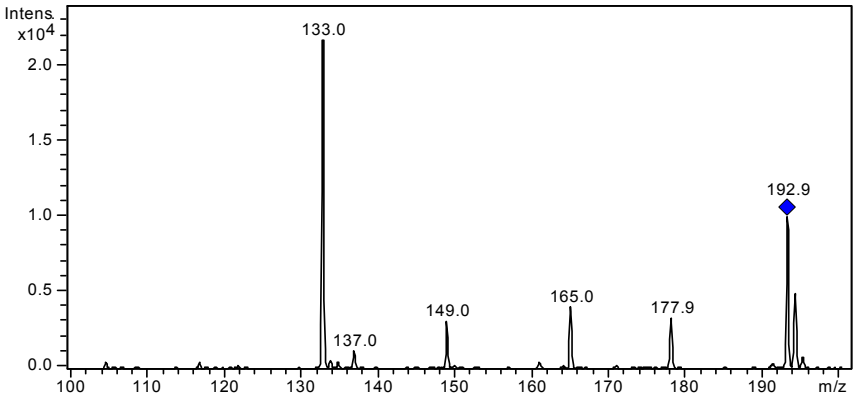

Figure 5. MS/MS fragmentation mass spectra of scopoletin

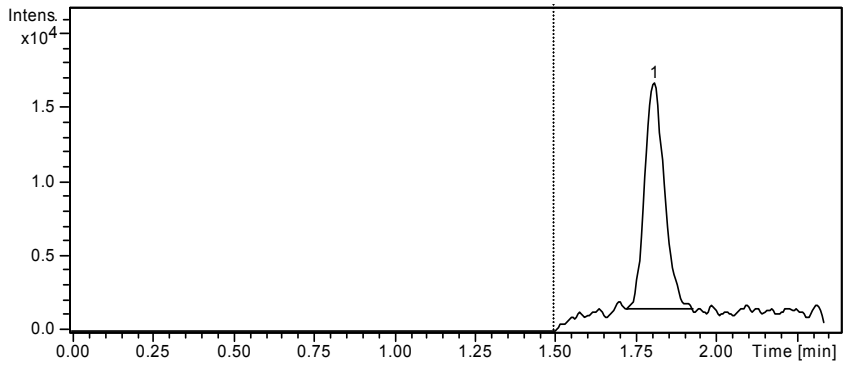

Figure 6. The chromatogram of scopoletin, at quantification limit of the analytical method (12.8 ng/ml)

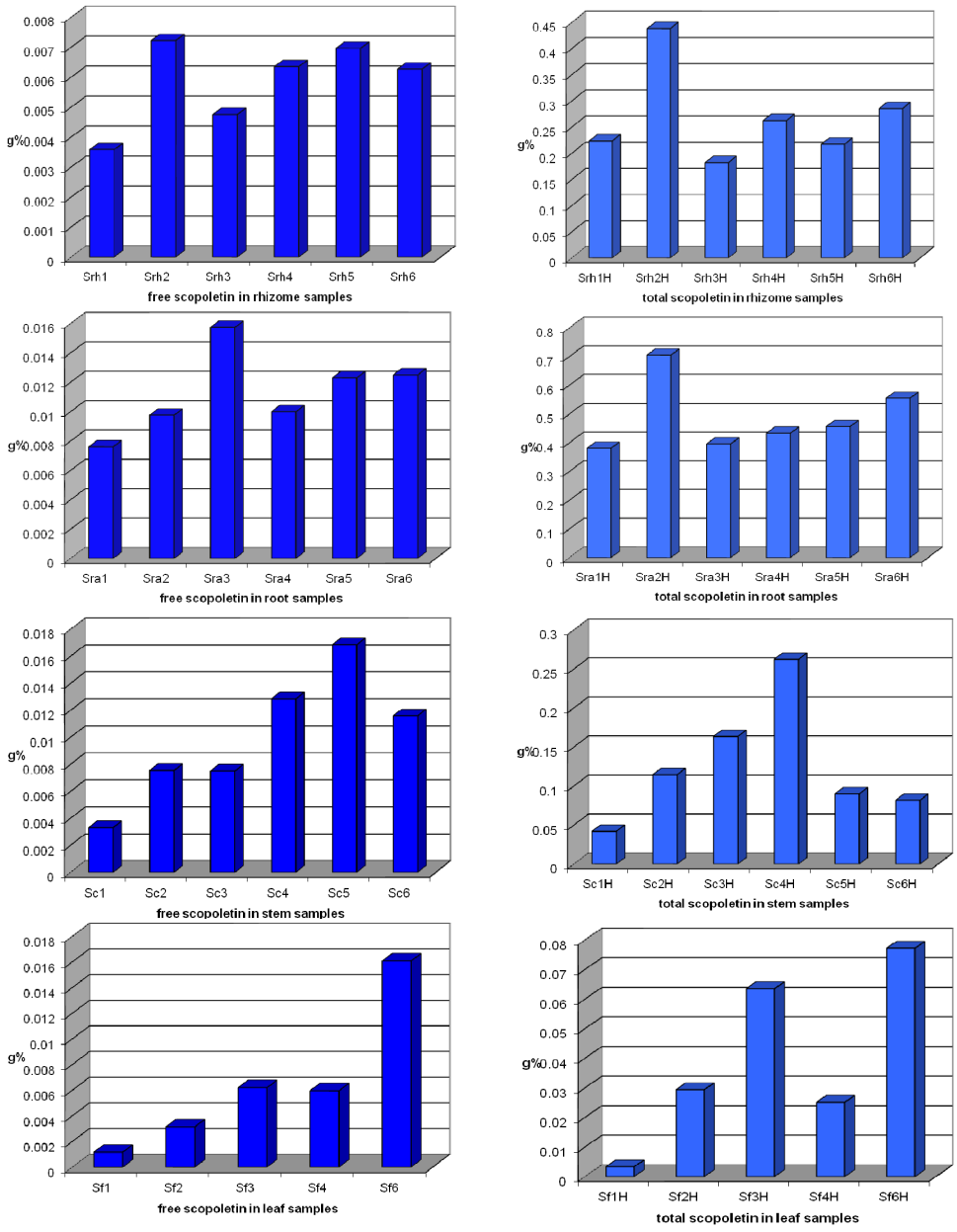

Figure 7. The amount of free and total scopoletin in rhizome, root, stem and leaf samples

The free and total scopoletin amounts determined during the vegetation period were: 0.0035–0.0069% respectively 0.18 - 0.43% in the rhizomes; 0.007 - 0.015% respectively 0.38 - 0.70% in the roots; 0.003 - 0.016% respectively 0.04 - 0.26% in the stems; 0.001 - 0.016% respectively 0.003 - 0.077% in the leaves.

The highest amount of free scopoletin was found for the rhizome in the samples harvested in middle May, for the root in the samples harvested in early June, for the stem in the samples harvested in middle July and for the leaf in the samples harvested in early August. The highest amount of free scopoletin was found in the underground organs before fruit maturation, after that period being identified in the aerial parts.

The highest amount of total scopoletin for rhizomes and roots was found in the samples harvested in May, for the stem in the samples harvested in June and for the leaves in the samples harvested in August. The total scopoletin amount, determined after hydrolysis, was up to 70 times higher than the free scopoletin one, indicating that it is preferentially accumulated as glycosides, mostly in the rhizomes and roots.

For the underground parts, the total amount of scopoletin is comparable to the total of coumarins found in the cultivated species from Poland [**2**], while the amount of free scopoletin is two times lower than the corresponding one. Concerning the leaves content, the amounts of free scopoletin and total scopoletin were 3 times respectively 6 times lower than the corresponding ones, suggesting that the climate and conditions of growth (spontaneous flora or culture) can influence this content.

CONCLUSION

The dynamics of scopoletin accumulation in vegetative organs of indigenous *S.carniolica* was quantified for the first time, using a rapid, precise and facile LC/MS method. The study revealed that the highest quantity of scopoletin accumulates as glycosides in rhizomes and roots during the month of May, accordingly to which we propose the harvesting of this vegetal medicinal product for extraction purposes in the period specified.

EXPERIMENTAL SECTION

Plant material

The rhizomes, roots, stems and leaves of Scopolia carniolica were collected from the same area in Remeţi, Maramureş County, during the months of May, June, July, and August. Plants were identified at the Pharmaceutical Botany Department, Faculty of Pharmacy, University of Medicine and Pharmacy

Cluj-Napoca, where a voucher specimen (nr. 972) was deposited. The vegetative organs were separated, the rhizomes were cut in round pieces, and all the plant material was dried at room temperature. The vegetal material was finely pulverized (sieve VI, Romanian Pharmacopoea X) [**12**].

TLC analysis

0.5 g powdered plat material was added to 10 mL methanol in a system provided with ascendant refrigerant and maintained at 80^{o}C for 10 min on water bath. The extraction liquid was filtered after cooling and the residue was pressed. Methanol was added to each sample up to 10 mL [**13**].

LC/MS analysis

0.1 g powdered plat material was added to 10 mL methanol in a system provided with ascendant refrigerant and maintained at 80^{o}C for 30 min on water bath. The extraction liquid was filtered after cooling and the residue was pressed. Methanol was added to each sample up to 10 mL (solution A). The hydrolyzed samples were prepared as follows: 0.1 mL solution A was treated with 2 mL of 2 N hydrochloric acid and maintained at 80^{o}C for 10 min on water bath in a system provided with ascendant refrigerant. After cooling distilled water was added up to 3 mL.

Reagents

Methanol of gradient grade for liquid chromatography, formic acid, hydrochloric acid, ethyl acetate, and potassium hydroxide of analytical-reagent grade were purchased from Merck KGaA (Darmstadt, Germany). Bidistilled, deionised water *pro injections* was purchased from Infusion Solution Laboratory of University of Medicine and Pharmacy Cluj-Napoca (Romania). Standards: scopoletin from Roth (Germany) ad umbeliferon from Fluka (Germany) were used.

Apparatus and chromatography conditions

The TLC analysis was performed in the following conditions: Adsorbant: TLC Silica gel GF 254 (Merck) plates; Solvent system: ethyl acetate (p.a): methanol (p.a) : water (100/16.5/13.5) (v/v/v); Standards: scopoletin, umbeliferon 0,01% m/v in methanol; 20 μL of samples and standards were applied on 1 cm band with Microcaps TLC spotting capillaries; Detection: after drying, the plate was sprayed with potassium hydroxide 5% in methanol and examined after 30 min in fluorescence at 365 nm [13].

HPLC analysis

HP 1100 Series binary pump, HP 1100 Series auto sampler, HP 1100 Series thermostat, Agilent Ion Trap 1100 VL mass spectrometer; Column: Zorbax SB-C18 100 mm x 3,0 mm i.d., 3,5 μm (Agilent, SUA), on-line filter

0,2 µ (Agilent); Mobile phase: formic acid 0,1% (v/v) - methanol 68/32 (v/v), isocratic elution, 1 ml/min, 40°C, injection volume: 5 µL; Detection: mass spectrometry, m/z 193> m/z 133.

MS detection

Electrospray ionization (ESI) positive ionisation, gas: nitrogen, flow rate 12 l/min, ion source temperature 350°C, nebuliser: nitrogen at 70psi pressure capillary voltage -1500 V, analysis mode MS/MS, m/z 193 > 133.

REFERENCES

1. C. Ştefănescu, M. Tămaş, *Farmacia*, **2001**, *49*(2),77.
2. S. Nowak, T.H. Dzido, E. Soczewinski, M. Wolbis, *Acta Pol. Pharm.,* **2002**, *59*(4), 259.
3. I. Ciulei, E. Grigorescu, U. Stănescu, «Plante medicinale, fitochimie şi fitoterapie», vol. II, Editura Medicală, Bucharest, **1993**, 384.
4. Z. Ding, Y. Dai, Z. Wang, *Planta Med.,* **2005**, *71*(2), 183.
5. S.Y. Kang, S.H. Sung, J.H. Park, Y.C. Kim, *Arch. Pharm. Res.,* **1998**, *21*(6), 718.
6. F.C. Meotti, J.V. Ardenghi, J.B. Pretto, M.M. Souza, J. D'Avila Moura, A.C. Junior et al., *J. Pharm. Pharmacol.,* **2006**, *58*(1), 199.
7. E.J. Oliveira, M.A. Romero, M.S. Silva, B.A. Silva, I.A. Medeiros, *Planta Med.,* **2001**, *67*(7), 605.
8. C.Y. Shaw, C.H. Chen, C.C. Hsu, C.C. Chen, Y.C. Tsai, *Phytoter. Res.,* **2003**, *17*(7), 823.
9. M.L. Barreiro Arcos, G. Cremaschi, S. Werner, J. Coussio, G. Ferraro, C. Anesini, *Phytoter. Res.,* **2006**, *20*(1), 43.
10. J.C. Capra, M.P. Cunha, D.G. Machado, A.D.E. Zomkowski, B.G. Mendes, A.R.S. Santos et al., *Eur. J. Pharmacol.*, **2010***, 643*(2-3), 232.
11. J. Rollinger, A. Hornick, T. Langer, H. Stuppner, H. Prast, *J. Med. Chem.,* **2004**, *47*(25), 6248.
12. ***, "Farmacopeea Română", Ed. X, Editura Medicală, Bucharest, **1993**, 805.
13. M. Tămaş, *Clujul medical,* **1986**, *59*(2), 173.

STUDIA UBB CHEMIA, LVIII, 1, 2013 (p. 81 – 91)
(RECOMMENDED CITATION)

CORROSION BEHAVIOUR OF COMPOSITE COATINGS OBTAINED BY ELECTROLYTIC CODEPOSITION OF ZINC WITH NANOPARTICLES OF CeO_2·ZrO_2 BINARY OXIDES

PATRICK IOAN NEMES[a], NICOLETA COTOLAN[a], LIANA MARIA MURESAN[a*]

ABSTRACT. Composite Zn coatings incorporating CeO_2·ZrO_2 nanoparticles were obtained by electrodeposition on steel from an industrial electrolyte, containing 75 g L^{-1} $ZnCl_2$, 230 g L^{-1} KCl, 20 g L^{-1} H_3BO_3 and two additives, 1 mL L^{-1} each.

The influence of the oxide nanoparticles on phase composition, morphology and structure of the obtained coatings was investigated by X−ray diffraction and SEM−EDX methods. By using polarization measurements, the corrosion behaviour of the deposits was examined and the corrosion process on Zn−CeO_2·ZrO_2 composite coatings was compared with that taking place on composite coatings prepared with a simple mixture of CeO_2 and ZrO_2 oxides and with each oxide separately. On all the composite coatings, corrosion was found to be slower than on the pure Zn surface.

Keywords: *Corrosion; Electrodeposition; Zinc−nanoparticles composite coatings; CeO_2·ZrO_2 binary oxides*

INTRODUCTION

The need to improve the corrosion resistance of protective coatings on steel promoted the application of different post plating surface modification treatments (*e.g.* chrome passivation, protective film generation etc.), but, at the same time, the development of new coatings containing minute amounts of nanoparticles (metal oxides, carbides etc.) with a beneficial effect on the corrosion resistance of the substrate [1].

A survey of recent literature on the metallic composite coatings shows that several oxide nanoparticles are very promising filling dopants for material coatings [2]. Generally, these particles provide improved resistance to oxidation,

[a] *Department of Chemical Engineering "Babes-Bolyai" University, 1, M. Kogalniceanu St., 400084 Cluj-Napoca, Romania*
* *Corresponding author: limur@chem.ubbcluj.ro*

corrosion, erosion and wear to the composite layer. Consequently, many efforts have been made to include oxidic particles such as TiO_2, ZrO_2, CeO_2, SiO_2, Al_2O_3 [3−9] etc. into metallic coatings, by using different preparation methods. Among these particles, ZrO_2 and CeO_2 are particularly very interesting due to their promising physical and chemical properties [6, 10, 11].

Thus, zirconia possesses high resistance to wear and corrosion, biocompatibility, heat resistance and presents good adhesion to metallic surfaces [11, 12]. Chemical vapour deposition, electrophoretic deposition and sol–gel deposition by dip coating procedure are common routes to prepare ZrO_2 coatings for anti−corrosion purposes and for the improvement of mechanical properties of the substrates [12, 13]. It was also reported that ZrO_2 nanoparticles can be uniformly co−deposited into a nickel matrix from a Watts bath containing monodispersed particles in suspension, under DC electrodeposition condition [14]. Zn−ZrO_2 composite coatings were also successfully produced by electrodeposition technique from zinc sulphate baths [15]. The electrolytic codeposition of zinc with different micron or submicron size particles suspended in a classical zinc electroplating bath takes place by agitation and/or use of surfactants, at a current density of around 2 A dm^{-2} [3, 16, 17-19].

Cerium oxides and cerium hydroxides are reported as cathodic corrosion inhibitors and have been proposed as effective species for the protection of metals from corrosion. CeO_2 nanoparticles were co−electrodeposited with nickel and conferred the coating enhanced wear and corrosion resistance, microhardness and improved high temperature oxidation resistance [20].

Despite the large number of works published in literature reporting the unique properties of CeO_2 and ZrO_2, very little has been published about a combination of both in the field of the pre−treatments. It was shown that bis−1,2−[triethoxysilylpropyl]−tetrasulfide silane films containing $CeO_2{\cdot}ZrO_2$ nanoparticles deposited by dip−coating on galvanised steel substrates are very efficient anticorrosion coatings. The presence of zirconium ions provided very good barrier properties, whereas the presence of cerium provided better corrosion inhibition ability [21]. However, to the best of our knowledge, there are no reports on the preparation of composite layers by simultaneous co−deposition of zinc with CeO_2 and ZrO_2 nanoparticles.

In this context, the aim of this work is to investigate the effect of CeO_2 and ZrO_2 nanoparticles, used as a mechanical mixture or as binary $CeO_2{\cdot}ZrO_2$ oxides on the corrosion resistance of zinc coatings, after the electro−co−deposition of nanoparticles with zinc. The method combines the advantages of metal electroplating (such as low cost, versatility and an easy process control) with those of composite materials and allows obtaining advanced materials with tailor−made properties [1].

X ray diffraction (XRD) and SEM−EDX methods were used to determine the structure, the surface morphology and the chemical composition of the deposits. Polarization measurements followed by Tafel interpretation of the polarization curves were carried out in order to characterize the corrosion behaviour of the coatings.

RESULTS AND DISCUSSION

Morphological and structural analysis

SEM observations of the samples (Figures 1, 2) revealed an uniform aspect of the pure Zn deposit, with very small prominences that appear from place to place. The uniformity of the zinc deposit is due mainly to the brightening agents, that reduce the roughness of the surface to a nanometric level.

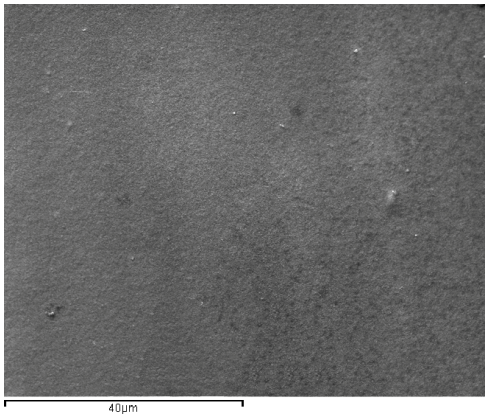

Figure 1. SEM micrograph of pure Zn deposits

In the presence of the CeO_2+ZrO_2 mixture in the plating bath, the cathodic deposit becomes more fine grained, but less uniform (Figure 2).

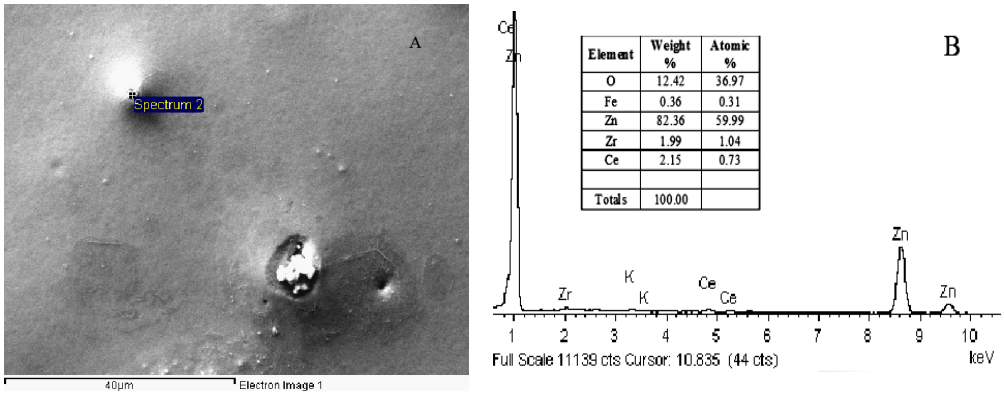

Figure 2. SEM micrograph (A) and EDX spectrum (B) of Zn−(CeO_2+ZrO_2) deposits

This can be due to the fact that the nanoparticles interfere with the nucleation−growth process by enhancing nucleation and exerting a detrimental effect on the crystal growth. Observations of the Zn−(CeO_2+ZrO_2) composite coating by EDX analysis, performed on the irregularities of the surface (Fig. 2B) revealed the presence of both ceria and zirconia, thus proving the successful incorporation of nanoparticles in the metallic matrix. Nevertheless, a small degree of embedded oxide nanoparticles can be observed (table in Fig. 2B), values that are close to those reported in previous works [5, 6].

X−ray Diffraction

The XRD spectra of the investigated specimens are depicted in Figure 3. The main diffraction line can be attributed to the preferential hexagonal orientation of the zinc crystallites on the (101) direction, mainly determined by the presence of surfactants in the plating bath. It has been suggested that a preferred orientation of the zinc crystallites to the (101) direction may facilitate a good co−deposition of ceria [22], and possibly of other nanoparticles as well.

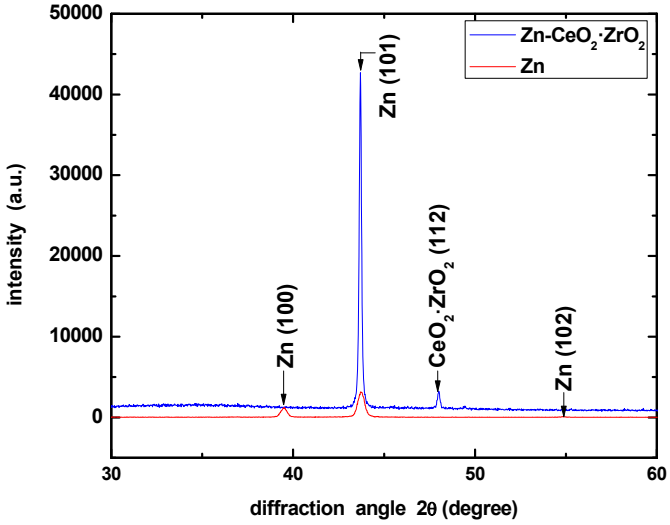

Figure 3. X−ray Diffraction results for the Zn and Zn−CeO_2·ZrO_2 deposits, 1.25 g L^{-1}

Upon addition of the CeO_2·ZrO_2 oxide nanoparticles in the electrolytic bath, the diffraction lines of the resulting deposits exhibit a change in intensity, indicating a textural modification of the coating. The line corresponding to the (101) direction becomes more intense, while the (100) and (102) peaks decrease in height. At the same time, a new peak appears, corresponding to the (112) orientation, that can be attributed to the presence of CeO_2·ZrO_2 [23].

Electrochemical corrosion measurements

Open circuit potential

As it can be observed from Table 1, the open circuit potential values of the investigated samples recorded after one hour of immersion in the corrosive medium are relatively close to each other, with a variation of ±30 mV. The shifts towards a more negative potential in the presence of nanoparticles in the Zn deposit suggest the existence of an influence exerted by these particles on the oxygen reduction process.

Table 1. Open circuit potential values for the obtained Zn and Zn−composite deposits

Deposit	Nanoparticles concentration [g L^{-1}]	OCP [mV *vs* Ag/AgCl]
Zn	0	−983
Zn−ZrO_2	1.25	−1014
Zn−CeO_2		−1011
Zn−CeO_2·ZrO_2	1.25	−996
	5	−1008
Zn−CeO_2+ZrO_2	1.25	−984
	5	−994

Polarization curves

The results of OCP analysis were further endorsed by conducting polarization studies. The cathodic and anodic polarization curves of Zn, Zn−(CeO_2·ZrO_2), Zn−(CeO_2+ZrO_2), Zn−ZrO_2 and Zn−CeO_2 coatings recorded after 1h of immersion in Na_2SO_4 solution (pH 5) are presented in Figure 4. From the polarization curves, the corrosion parameters were evaluated by using only the anodic Tafel slopes, due to the fact that the cathodic branches of the polarization curves are flat (the cathodic process is controlled by the diffusion of O_2, being impossible to calculate $ß_c$). Thus, some degree of imprecision must be associated with the estimated corrosion rate under these conditions. However, a comparison between the behaviours of different deposits could be made, at least semi−quantitatively.

It has been established that a very low concentration of nanoparticles could be insufficient to enhance the corrosion resistance of the deposit, due to a too low percentage of nanoparticles embedded in the metallic matrix, while a too high concentration could generate defects in the coating, which can be starting points for generalized corrosion. Thus, an optimal concentration is required to be found for every particular system.

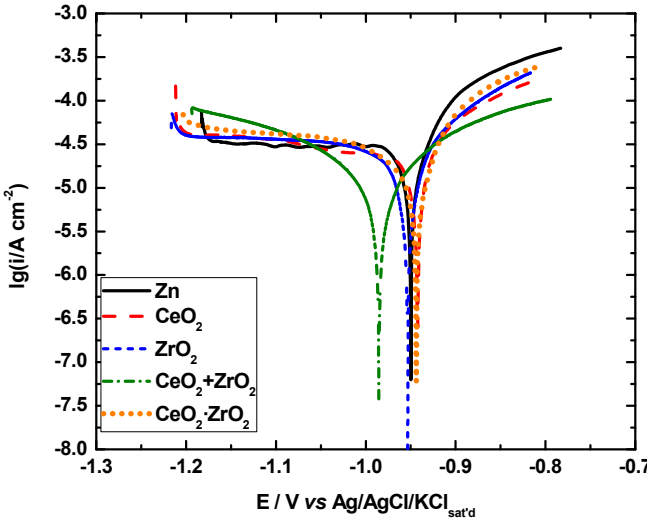

Figure 4. Polarization curves (±200 mV *vs OCP*) for Zn and composite zinc deposits with a 1.25 g L^{-1} concentration of nanoparticles

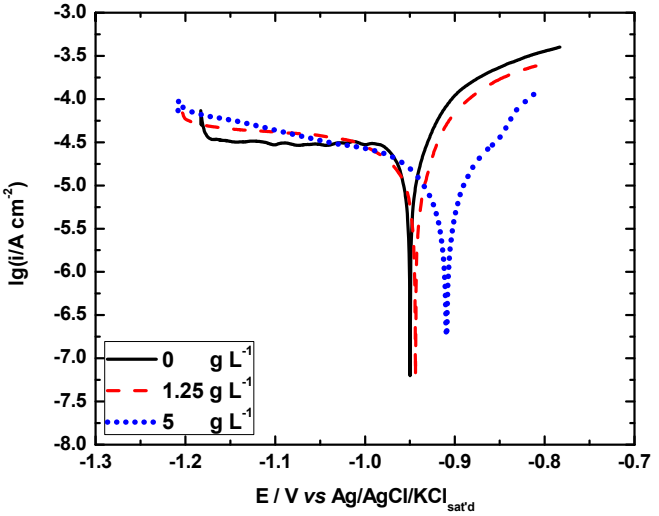

Figure 5. Polarization curves (±200 mV *vs OCP*) for Zn and Zn−CeO_2·ZrO_2 deposits with various concentrations of nanoparticles

The kinetic parameters for the corrosion process were estimated and are presented in Table 2.

Table 2. Corrosion parameters estimated from potentiodynamic measurements for pure zinc deposit and for Zn−oxide nanoparticles composite coatings

Deposit	Nanoparticle concentration [g L^{-1}]	i_{corr} [μA cm^2]	E_{corr} [mV *vs* Ag/AgCl]	R_p [Ω cm^2]	R^2/N*
Zn	0	65.76	−948	1272	0.99/17
Zn−ZrO_2	1.25	27.03	−956	2679	0.99/25
Zn−CeO_2		37.65	−942	1767	0.99/22
Zn−CeO_2·ZrO_2	1.25	35.94	−944	2027	0.99/25
	5	10.60	−909	4542	0.99/27
Zn−CeO_2+ZrO_2	1.25	15.40	−984	4063	0.99/23
	5	15.94	−953	3420	0.99/42

* N represents the number of points from which the R_p was estimated

The influence of the nanoparticles concentration on the corrosion behaviour of the composite coatings was already reported [2]. As it can be observed from Table 2, the lowest corrosion current density and the highest polarization resistance are noticed in the case when 5 g L^{-1} binary CeO_2·ZrO_2 oxide nanoparticles were used.

In the case of the CeO_2+ZrO_2 mixture, the best corrosion resistance corresponded to 1.25 g L^{-1}concentration, closely followed by the 5 g L^{-1} concentration. At the same time, it should be mentioned that in this case, the cathodic branches of the polarization curves recorded when the mixture is used, becomes mostly controlled by the charge transfer step, instead of the O_2 diffusion step.

At a concentration of 1.25 g L^{-1} the most beneficial effect was noticed in the case of CeO_2+ZrO_2 mixture, followed by ZrO_2 and the binary CeO_2·ZrO_2 oxide, confirming the importance of the nature and properties of nanoparticles (size, surface charge, shape, previous treatments etc.) in the corrosion behavior of the composite deposits in which the nanoparticles are incorporated [24]. At the same time, by comparing the results obtained when CeO_2 and ZrO_2 were used separately, with those obtained in the presence of their mixture, it can be observed that a synergistic effect occurs when both are present, suggesting that the zirconia nanoparticles in combination with ceria offers a better protection than each type of nanoparticles used alone, both having a complementary role in this process.

CONCLUSIONS

The analysis of the results led to the following conclusions:

- The co−deposition of oxide nanoparticles with zinc leads to changes in the morphology of the resulting nanocomposite coatings as compared to pure Zn coatings. The composite coatings incorporating binary $CeO_2 \cdot ZrO_2$ oxides exhibited the highest corrosion resistance, due to the inclusion of the binary oxide in the metallic matrix.
- The physical and electrochemical properties of Zn coatings were best when the binary $CeO_2 \cdot ZrO_2$ and CeO_2+ZrO_2 mixture oxide nanoparticles were used. CeO_2 provides enhanced corrosion protection, with an effect on the oxygen reduction reaction, while ZrO_2 inhibits the corrosion process, and improves the wear resistance.
- The binary oxides used in optimal concentration (5 g L^{-1}) were proven to be more efficient than the simple mixture of the two oxides (CeO_2 and ZrO_2) probably due to the uniform distribution of Ce and Zr oxides on the surface of the composite samples (50:50 w:w).
- A synergistic effect was put in evidence when the two oxides were used in mixture as compared to individual ones.
- The corrosion properties of the composite coatings depend on the nanoparticles concentration in the plating bath. Thus, an optimal concentration was put on evidence for the investigated nanocomposite deposits. The existence of an optimal concentration of nanoparticles is the result of the action of two contrary effects: on one hand, the nanoparticles have a beneficial influence, by reducing the active surface in contact with the corrosive medium and on the other hand, at a concentration that may be too high, they could generate defects in the metallic coating, stimulating corrosion.

EXPERIMENTAL SECTION

Materials

Three types of nanoparticles were used: ZrO_2 (Zirconium (IV) Oxide, Sigma Aldrich, TEM size <100 nm), CeO_2 (Cerium (IV) Oxide, Sigma Aldrich (BET size <25 nm) and a binary oxide $CeO_2 \cdot ZrO_2$ (Sigma Aldrich, BET size <50 nm). Also, experiments were performed using a physical mixture of commercial ZrO_2 and CeO_2 (50:50 w:w). In all experiments, the total concentration of nanoparticles (ZrO_2, CeO_2, $CeO_2 \cdot ZrO_2$ and a mixture of the oxide nanoparticles ZrO_2 and CeO_2 (50:50 w:w) in the electrolytic bath, was 1.25 g L^{-1}, respectively 5 g L^{-1}. The particles were suspended in an aqueous solution (pH=5.9) containing 75 g L^{-1} $ZnCl_2$, 230 g L^{-1} KCl, 20 g L^{-1} H_3BO_3,

and two additives (a surfactant and a brightening agent), 1 mL L^{-1} each. The corrosion studies were carried out by using a solution of 0.2 g L^{-1} Na_2SO_4, pH=5. All other reagents were of analytical grade and used as received.

Methods

Zn and Zn−oxide nanoparticles coatings were galvanostatically deposited on carbon steel (EN 10025 Euronorm) in a shape of a disc (S = 0.5024 cm^2) at a current density of 20 mA cm^{-2}, during 30 minutes, under magnetic stirring at 250 rpm, by using a potentiostat (PARSTAT 2273), at room temperature (21 ± 2ºC). The thickness of the resulting coatings was about 20 μm. Prior to the electrodeposition process, the working electrode was wet polished on emery paper of different granulations (from 600 to 2500) and finally on felt with a 2 μm diamond polishing paste (Buehler, US).

Before plating, the electrode was ultrasonicated for 2 min in ethanol, then thoroughly rinsed with ethanol and distilled water in order to remove any remaining impurities from the surface.

The 50 mL electrolytic bath containing the dispersed nanoparticles was ultrasonicated for 30 minutes then stirred at 400 rpm for 3 hours, previous to the plating procedure [17-19].

The electrodeposition experiments were performed in a three−electrode cell with a volume of 62 mL, with a separate compartment for the reference electrode connected with the main compartment *via* a Luggin capillary. The working electrode was the coated steel disc, the reference electrode was an $Ag/AgCl/KCl_s$ electrode and the counter electrode was a platinum coil.

During corrosion tests, the potentiodynamic polarization measurements were conducted using an electrochemical analyzer (PARSTAT 2273).

Corrosion experiments were carried out in 0.2 g L^{-1} aerated Na_2SO_4 solution (pH 5), at room temperature. Open−circuit potential (*OCP*) measurements were performed as a function of time. Anodic and cathodic polarization curves were recorded in a potential range of $E = E_{corr} \pm 200$ mV, with a scan rate of 0.166 mV s^{-1}.

The structure of the deposits and the preffered orientation of the crystallites were determined by XRD analysis with a Brucker X−ray diffractometer with a Cu K_α (λ = 0,15406 nm) at 45 kV and 40 mA. The 2θ range of 20–100º was recorded at the rate of 0.02º and 2θ 0.5 s^{-1}. The crystal phases were identified comparing the 2θ values and intensities of reflections on X−ray diffractograms with JCP data base using a Diffrac AT−Brucker program.

The SEM micrographs of the surfaces were performed by using a Carl Zeiss Evo series 40x VP and the EDX interpretations were obtained by using an Oxford Instruments EDX equipment, coupled with SEM.

ACKNOWLEDGEMENTS

This work was possible with the financial support of the Sectoral Operational Programme for Human Resources Development 2007–2013, co–financed by the European Social Fund, under the project number **POSDRU/107/1.5/S/76841** with the title „Modern Doctoral Studies: Internationalization and Interdisciplinarity".

Prof. Dr. Lorenzo Fedrizzi and Dr. Maria Lekka from the University of Udine, Italy are gratefully acknowledged for the SEM and EDX observations.

Dr. Emil Indrea from the National Institute for Research and Development of Isotopic and Molecular Technologies Cluj−Napoca, Romania, is gratefully acknowledged for the XRD measurements.

REFERENCES

[1] A. Hovestad, L.J.J. Jansen, *Journal of Applied Electrochemistry,* **1995**, *25*, 519.

[2] C.T.J. Low, R.G.A. Wills, F.C. Walsh, *Surface & Coatings Technology*, **2006**, *201*, 371.

[3] A. Gomes, M.I. Da Silva Pereira, M.H. Mendonça, F.M. Costa, *Journal of Solid State Electrochemistry,* **2005**, *9*, 190.

[4] B.M. Praveen, T.V. Venkatesha, *Applied Surface Science*, **2008**, *254*, 2418.

[5] W. Liu, Y. Chen, C. Ye, P. Zhang, *Ceramics International,* **2002**, *28*, 349.

[6] P.M. Ashraf, S.M.A. Shibli, *Electrochemistry Communications*, **2007**, *9*, 443.

[7] T.T. Tuaweri, G.D. Wilcox, *Surface & Coatings Technology,* **2006**, *200*, 5921.

[8] K. Kondo, A. Ohgishi, Z. Tanaka, *Journal of The Electrochemical Society,* **2000**, *147*, 2611.

[9] H.M. Hawthorne, A. Neville, T. Troczynski, X. Hu, M. Thammachart, Y. Xie, J. Fu, Q. Yang, *Surface & Coatings Technology,* **2004**, *176*, 243.

[10] Y. Wang, R. Kovacevic, J. Liu, *Wear,* **1998**, *221*, 47.

[11] S.K. Yen, M.J. Guo, H.Z. Zan, *Biomaterials*, **2001**, *22*, 125.

[12] J.H. Sui, W. Cai, *Nuclear Instruments and Methods in Physics Research B*, **2006**, *251*, 402.

[13] Y−P. Fu, S−H. Hu, B−L. Liu, *Ceramics International*, **2009**, *35*, 3005.

[14] F. Hou, W. Wang, H. Guo, *Applied Surface Science,* **2006**, *252*, 3812.

[15] K. Vathsala, T.V. Venkatesha, *Applied Surface Science*, **2011**, *257*, 8929.

[16] A.V. Pop, A. Vlasa, S. Varvara, C. Bulea, L. Muresan, *Optoelectronics and Advanced Materials*, **2009**, *3*, 1290.

[17] A. Vlasa, S. Varvara, A. Pop, C. Bulea, L. M. Muresan, *Journal of Applied Electrochemistry*, **2010**, *40*, 1519.

[18] E. Grünwald, C. Bulea, "Electrodepunerea zincului si aliajelor de zinc din solutii slab acide", Ed. Casa Cartii de Stiinta, Cluj-Napoca, **2011**, 211.

[19] P. Nemes, M. Zaharescu, L. M. Muresan, *Journal of Solid State Electrochemistry*, **2012**, DOI 10.1007/s10008−012−1901−6.

[20] S.T. Aruna, C.N. Bindu, V. Ezhil Selvi, V.K. William Grips, K.S. Rajam, *Surface & Coatings Technology*, **2006**, *200,* 6871.

[21] M.F. Montemor, W. Trabelsi, S.V. Lamakac, K.A. Yasakauc, M.L. Zheludkevichc, A.C. Bastos, M.G.S. Ferreira, *Electrochimica Acta*, **2008**, *53*, 5913.

[22] S. Ranganatha, T.V. Venkatesha, K. Vathsala, M.K. Punith Kumar, *Surface & Coatings Technology*, **2012**, *208*, 64.

[23] F. Zhang, C.H. Chen, J.M. Raitano, J.C. Hanson, W.A. Caliebe, S. Khalid, S.W. Chan, *Journal of Applied Physics*, **2006**, *99*, 084313.

[24] C. Zanella, M. Lekka, P.L. Bonora, *Journal of Applied Electrochemistry,* **2009**, *39*, 31.

STUDIA UBB CHEMIA, LVIII, 1, 2013 (p. 93 – 103)
(RECOMMENDED CITATION)

THE DETERMINATION OF CONCENTRATIONS OF IONS Zn^{2+}, Cd^{2+}, Mn^{2+} WITH 1-(2-PYRIDYLAZO)-2-NAPHTHOL IN AQUEOUS-MICELLAR MEDIUM ON TWO-DIMENSIONAL ABSORPTION SPECTRA OF WAVE LENGTH BY pH COORDINATES

ANATOLIY V. DROZD[a*], OLGA S. KALINENKO[a], NATALIA A. LEONOVA[a]

ABSTRACT. An iterative author's algorithm (step-by-step approach) for determine concentrations of ions Zn^{2+}, Cd^{2+}, Mn^{2+} with 1-(2-pyridylazo)-2-naphthol in aqueous-micellar medium on two-dimensional spectra of absorption of wave length by pH coordinates is proposed. Different two- and three-component model mixtures analyses were carried out. Test results comparison of determination and roof-mean-square deviation from introduced concentrations by proposed iterative algorithm and least squares method shows advantages of iterative algorithm for three-component systems and congruent accuracy for two-component systems.

Keywords**:** *two-dimensional absorption spectra, consistent method of incorporating surface, least squares method, 1-(2-pyridylazo)-2-naphthol, complexes, determination of ions* Zn^{2+}, Cd^{2+}, Mn^{2+}

INTRODUCTION

Using of the two-dimensional spectra and spectra of high order in the chemical analysis increases amount of information about the system and increases accuracy as compared with one dimension spectra and scalar measurements. Spectrophotometric method is simple and cheap as compared with instrumental methods of atomic spectroscopy. Two-dimensional spectra of multicomponent systems create additional abilities for the determination of several components in the system. Coordinate pH can be complementary coordinate to λ. Two-dimensional spectra can be handled using known methods.

[a] *V.N. Karazin Kharkiv National University, Svobody sq., 4, Kharkiv, 61022, Ukraine*
* *Corresponding author: drozd@univer.kharkov.ua*

RAFA method assumes calibration matrix decomposition to the product of two vectors and usage of them for the calculation of the concentrations. Such calculations are overlaid with systematic errors, which arise from the interference of the components. Developed algorithm allows to negate systematic errors.

Two- and three-component zinc-cadmium-manganese subsystems occur in the analysis of special aluminum alloys, in waste waters of galvanizing plants, in the analysis of vegetable agricultural products.

Spectrophotometric determination of Zn^{2+} and Cd^{2+} ions at joint presence in waste waters using chelates extraction with PAN in chloroform is described in [1]. It is also specified that owing to the similarity of absorption spectra complexes with PAN, the determination errors are great and yield to dithizone determinations.

In [2] there is shown the possibility of determination of Zn^{2+} and Cd^{2+} ions with PAN in aqueous-micellar medium on two-dimensional spectra of wave length by pH with formation of a pseudo-one-dimensional vector-spectrum.

Rank annihilation factor analysis (RAFA) method was offered, proved and developed in the works [3, 4]. RAFA method was created for processing of two-dimensional spectra. Last years RAFA method is used for the determination of the concentration of the component at determination of equilibriums constants [5], at spectrophotometric determination of the constants of acidity of dyes [6], at the determination of the protonacids by the acid-base titration method [7], the kinetic - spectrophotometric analysis [8]. A new spectrophotometric method has been developed in [9] to determine melamine in milk. The RAFA method is applied at the determination of one component in the presence of other components showing an analytical signal in the same intensive parameter space [10-12]

The purpose of the present work is to study the possibilities of consistent method of incorporating surface at step-by-step determination of Zn^{2+}, Cd^{2+}, Mn^{2+} ions out of two-dimensional absorption spectra of complexes with PAN of λ-pH coordinates in two- and three - component systems.

RESULTS AND DISCUSSION

Optimization of spectrum measurements of wavelength and pH

Absorption spectra of Zn^{2+}, Cd^{2+} and Mn^{2+} ion complexes with the PAN in aqueous-micellar solutions remain quite similar (fig. 1). Simultaneous determination using component extinctions at different wave lengths is meaningless.

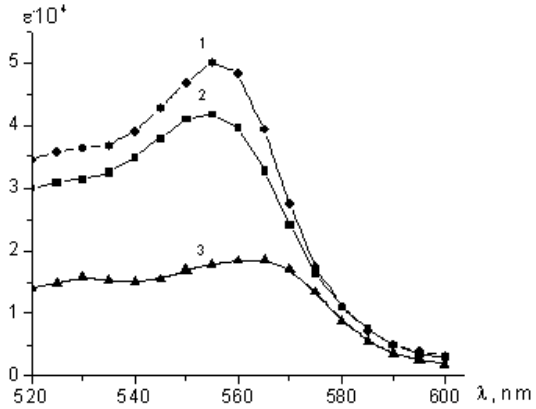

Figure 1. Absorption spectra of $Zn(PAN)_2$ (1), $Cd(PAN)_2$ (2), $Mn(PAN)_2$ (3) complexes in the aqueous-micellar medium. Mass fraction of sodium ethoxydodecylsulphate ω = 2,5 %. Ion concentrations $c(Zn(PAN)_2)$= 0,1-1·10^{-5} mol/l, $c(Cd(PAN)_2)$= 0,1-1·10^{-5} mol/l, $c(Mn(PAN)_2)$= 0,1-1·10^{-5} mol/l

If pH is used as an intensive parameter of analytical signal, additional differences in absorption coefficients ($\varepsilon_{\lambda,pH,j}$) of components are shown.

$$\varepsilon_{\lambda,pH,j} = \varepsilon_{\lambda.j}\alpha_{pH,j} \quad (1)$$

The ($\alpha_{pH,j}$) yield of complexes - pH relationships are presented in fig. 2.

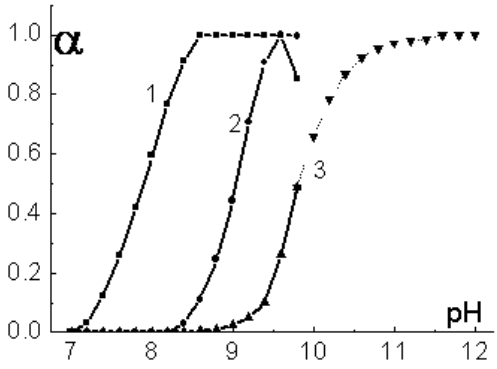

Figure 2. The yield of complexes - pH relationship in aqueous-micellar medium $Zn(PAN)_2$ (1), $Cd(PAN)_2$ (2), $Mn(PAN)_2$ (3). ω(sodium ethoxydodecylsulphate) = 2,5 %. Ion concentrations $c(Zn(PAN)_2)$ = 0,1-1·10^{-5} mol/l, $c(Cd(PAN)_2)$ = 0,1-1·10^{-5} mol/l , $c(Mn(PAN)_2)$ = 0,1-1·10^{-5} mol/l

For the subsequent calculations absorption spectra of each complex at different pH were normalized A_i/A_{max}, and after overlapping, there were selected wave length ranges in which spectrum structure is similar. This range is λ= 530-570 nm.

The result of the successive approximations for $Zn(PAN)_2$ according to the pH at λ = 555 nm is shown on the fig. 3. As it seen from the fig. 3, twenty successive approximations stabilize $c(Zn^{2+})$ value.

Beer's law holds in the whole pH range used

The yield of the complexes according to the pH is described by the equation of mass action law: $[M(PAN)_2] = \beta [M^{2+}] [HPAN] 10^{2pH}$. In order to keep complex yield portion constant (or close to constant) it is necessary for the reagent concentration in the solution to be considerably (10 times and more) higher than metal cation concentration, $[HPAN] >> [M^{2+}]$. In spite of the taken measures, it should be noted that after subtracting the first inscribed surface from the measured, all accumulated differences in the yield of the first complex -pH relationships remain in the residual surface. An attempt to exclude accumulation of distortions before calculating concentration of the second component by singular decomposition of difference matrix $DA^{(0)}$ by means of the "svd" [4] software and restoration using two eigenvalues didn't show any positive results. Cadmium concentrations do not vary significantly. The absence of the significant distortions in the residual analytical signal of spectra, especially at lower pH, is due to fulfillment of the following condition: $\beta_2/\beta_1 > \beta_1$.

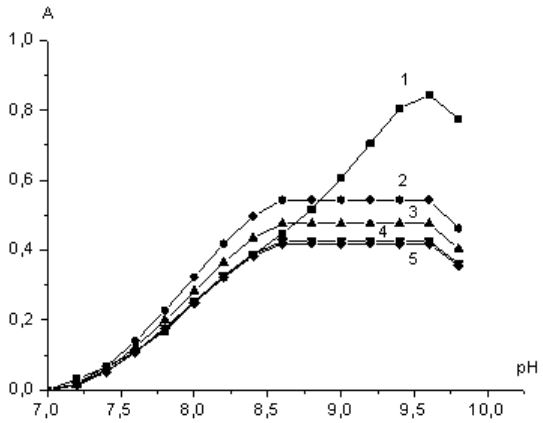

Figure 3. Relationships: 1 – total light absorbance of the mixture according- pH at λ = 555 nm; 2,3,4,5 – restored light absorbance at λ = 555 nm after one, three, fifteen and twenty iterations.

Analysis of the model solutions

Simultaneously determination of ion concentrations (c_j) for pseudo-one-dimensional spectra $\mathbf{A}(n_\lambda + n_{pH}, 1)$ was conducted by solving combined equations of the (7) type according to the least squares method.

$$\mathbf{E}(n_\lambda + n_{pH}, m)\cdot\mathbf{c}(m, 1) = \mathbf{A}(n_\lambda + n_{pH}, 1) \quad (2)$$

$$\mathbf{c} = (\mathbf{E}^{\mathbf{T}}\cdot\mathbf{E})^{-1}\cdot\mathbf{E}^{\mathbf{T}}\cdot\mathbf{A} \quad (3)$$

$\mathbf{E}(n_\lambda + n_{pH}, m)$ – matrix of the molar absorption coefficients has $n_\lambda + n_{pH}$ lines and m columns; m – number of components; $\mathbf{E}^{\mathbf{T}}$ – transpose of the matrix of coefficients.

The results of ion determination in the model solutions are presented in Table 1. Using found (c_j^{det}) and given (c_j^{input}) component concentrations, root-mean-square deviations from the given concentrations have been estimated.

$$s_c = \sqrt{\frac{\sum_{j=1}^{n}(c_j^{\det} - c_j^{input})^2}{n-1}} \quad (4),$$

where n – the number of three-component mixtures, or the number of two-component mixtures in which j-component is present. Such estimated deviation includes both random and systematic errors of the determination and acts as a measure of reproducibility.

Table 1. The results of ion concentrations determination in the model mixtures by iterative author's algorithm (IAA) and least squares method (LSM)

No	Analytical concentration, C 10^5 (mol L^{-1})			Found concentration, C,S_c 10^5 (mol L^{-1})			
	$Zn(PAN)_2$	$Cd(PAN)_2$	$Mn(PAN)_2$	Used method	$Zn(PAN)_2$	$Cd(PAN)_2$	$Mn(PAN)_2$
1	0.80	0.80	0.80	IAA	0.81	0.94	0.69
				LSM	1.27	0.35	0.18
2	1.20	0.40	0.40	IAA	1.10	0.49	0.21
				LSM	1.12	0.62	0.05
3	0.40	0.40	1.20	IAA	0.44	0.51	0.73
				LSM	0.47	0.40	1.58
4	0.40	1.20	0.40	IAA	0.46	1.04	0.33
				LSM	0.54	0.89	0.17
				IAA, S_c	0.06	0.13	0.18
				LSM, S_c	0.27	0.30	0.49

No	Analytical concentration, C 10^5 (mol L^{-1})			Found concentration, C,S_c 10^5 (mol L^{-1})			
	$Zn(PAN)_2$	$Cd(PAN)_2$	$Mn(PAN)_2$	Used method	$Zn(PAN)_2$	$Cd(PAN)_2$	$Mn(PAN)_2$
5	0.50	2.00	-	IAA	0.46	2.10	-
				LSM	0.46	1.99	-
6	0.50	-	2.00	IAA	0.48	-	2.23
				LSM	0.56	-	1.88
7	-	1.00	1.00	IAA	-	0.98	1.12
				LSM	-	0.81	1.10
8	-	2.00	0.50	IAA	-	2.10	0.45
				LSM	-	1.91	0.57
9	1.00	-	1.00	IAA	1.08	-	0.95
				LSM	0.89	-	1.15
				IAA, S_c	0.06	0.10	0.16
				LSM, S_c	0.09	0.11	0.12

Sequential determinations by developed method measure first from three components more accurately, then they measure second and worst accurately they measure third component. The result of the determination of first determined component Zn^{2+} is almost five times accurately then the result on LSM. There are the advantages for other ion but they are less. In spite of the errors given in the table, developed method results in the higher accuracy compared to the simultaneous determination using LSM.

As it seen from the results of analysis, working range for such determinations for three ions is $(0,2\text{-}2,0)\cdot10^{-5}$ mol·L^{-1}. Fewer concentrations have greater relative error.

Determination of Zn^{2+} and Mn^{2+} in oatmeal

The sample of oat «Hercules» TM «Dobrodiya», manufacturer CJSC «Niva», Ukraine, Luhansk city, was analysed. Analysis of oat was performed according to the method: 10 g of accurately weighed portion of oat is incinerated in the muffle furnace for 3 hours at the 740 K and dissolved in the 15 ml of diluted nitric acid. Mixture was filtered into the 50 ml volumetric flask after the dissolution of metal salts. Filtrate was diluted to the volume with water. 2,5 ml of the obtained solution was taken for analysis according to the described method.

For example, Table 2 shows the results of Zn^{2+} and Mn^{2+} determination in oatmeal using consistent method of incorporating surface. The method assumes ignition of the sample, dissolution in HNO_3 deposition and abstraction of Fe^{2+}, Cu^{2+}, Ni^{2+}, Co^{2+} ion complexes with PAN at pH 6,5-7. Neutral water

insoluble chelates Fe^{2+}, Cu^{2+}, Ni^{2+}, Co^{2+} with PAN deposited from an aqueous solution without sodium ethoxydodecylsulphate. Aqueous phase (filtrate) is used to determine Zn^{2+} and Mn^{2+}. Cadmium in vegetable objects cannot be determined by the given procedure, since its concentration significantly smaller. The accuracy of the analysis is verified by the addition technique.

Table 2. Concentration results of Zn^{2+}, Mn^{2+} in oatmeal

№	Added		Found				Concentration in sample	
	m(Zn^{2+}), mg	m(Mn^{2+}), mg	c(Zn^{2+}), mg/kg	*s*(Zn^{2+})	c(Mn^{2+}), mg/kg	s(Mn^{2+})	c(Zn^{2+}), mg/kg	c(Mn^{2+}), mg/kg
1	-	-	15.0 19.4	0.5	93.0 17.0	0.6	15.0	17.0
2	-	-	20.0		17.8		20.0	17.8
3	-	-	19.1		18.2		19.1	19.0
4	13	11	32.4	0.8	30.2	0.9	19.4	19.2
5	13	11	30.9		28.5		17.9	17.5
6	13	11	31.5		29.1		18.5	18.1

The results of the determination of mass fraction for c(Zn^{2+})=18,9 mg/kg, c(Mn^{2+})=18,1 mg/kg. Standard deviation s(Zn^{2+})=1,3 mg/kg, s(Mn^{2+})=0,9 mg/kg, Relative standard deviation S_r(Zn^{2+})=0,07, S_r(Mn^{2+})=0,05, «confidential interval» Δc(Zn^{2+})=1,4 mg/kg, Δc(Mn^{2+})=0,9 mg/kg.

Zinc concentration 19,1 ± 0,7 mg/kg, maximum admissible concentration (MAC) = 27 mg/kg Manganese concentration 18,1 ± 0,9 mg/kg, MAC = 50 mg/kg.

As it seen from the table 1, c_{min} (Cd^{2+}) is $3 \cdot S_c$ is 4 mg/kg, MAC (Cd^{2+}) is 0,1 mg/kg.

V – vector-spectrum of dimensional ion complexes Zn^{2+} and Mn^{2+} with PAN at pH of maximum emerge; **Q** – complex Zn^{2+} and Mn^{2+} emerge vectors according to the pH; $\mathbf{A}^{(0)}$ – the matrix of initial absorption in the analyzed system of oatmeal are presented as an example in the Table 3-5. Weight of the sample was 10,0 g.

Table 3. The molar absorption coefficients of the complexes $Zn^{2+}$and Mn^{2+} with PAN ($\varepsilon \cdot 10^{-2}$ l·mol·cm)

λ, nm	530	535	540	545	550	555	560	565	570
ε_{Zn}	381,7	377,0	401,0	441,0	486,0	519,0	499,0	405,0	280,0
ε_{Mn}	121,0	126,0	124,0	127,0	133,0	137,0	139,0	132,0	112,0

Table 4. Depending of emerge complex $Zn^{2+}$and Mn^{2+} with PAN according to pH.

pH	7.0	7.2	7.4	7.6	7.8	8.0	8.2	8.4	8.6	8.8	9.0	9.2	9.4	9.6	9.8
Q_{Zn}	0	0,034	0,125	0,258	0,420	0,594	0,768	0,914	1	1	1	1	1	1	0,850
Q_{Mn}	0	0	0	0	0	0	0	0	0	0	0,005	0,01	0,025	0,050	0.100

Table 5. The initial absorbances in the analyzed system of oatmeal.

pH λ,nm	7.0	7.2	7.4	7.6	7.8	8.0	8.2	8.4	8.6	8.8	9.0	9.2	9.4	9.6	9.8
530	0	0,032	0,072	0,120	0,170	0,220	0,266	0,306	0,338	0,378	0,399	0,423	0,506	0,532	0,663
535	0	0,030	0,071	0,119	0,169	0,220	0,267	0,307	0,336	0,373	0,393	0,417	0,493	0,529	0,663
540	0	0,031	0,074	0,124	0,178	0,232	0,282	0,324	0,355	0,393	0,414	0,439	0,515	0,557	0,685
545	0	0,035	0,083	0,138	0,198	0,258	0,312	0,358	0,392	0,432	0,456	0,484	0,562	0,604	0,731
550	0	0,039	0,092	0,154	0,220	0,285	0,346	0,396	0,433	0,477	0,503	0,535	0,618	0,658	0,781
555	0	0,042	0,099	0,166	0,236	0,306	0,370	0,423	0,462	0,506	0,535	0,570	0,658	0,697	0,818
560	0	0,0401	0,094	0,157	0,224	0,291	0,351	0,401	0,436	0,479	0,506	0,540	0,627	0,677	0,775
565	0	0,0323	0,075	0,124	0,176	0,228	0,276	0,316	0,346	0,384	0,402	0,426	0,506	0,566	0,695
570	0	0,0208	0,049	0,081	0,115	0,150	0,182	0,209	0,230	0,257	0,265	0,278	0,339	0,400	0,523

CONCLUSIONS

1) When consistent method of incorporating surface is used for determination, in three-component as well as in two-component systems, in the Zn^{2+}, Cd^{2+}, Mn^{2+} row, according to the determination sequence, concentration errors are increasing.

2) In a three-component system, determination errors using consistent method of incorporating surface are several times fewer, than determination errors using LSM. The repeatability of the measurements of Zn^{2+} is 5 times better, but for Cd^{2+} and Mn^{2+} is 2 times better than the results calculated using LSM.

The use of pseudo-one-dimensional method to determine three components shows unsatisfactory errors.

3) In two-component systems, LSM does not yield to the consistent method of incorporating surface by accuracy.

EXPERIMENTAL SECTION

Apparatus and software

All absorbance measurements were obtained using a spectrophotometer (spectrophotometer SF-46. LOMO, St. Petersburg, Russia; in quartz cells (l = 1 cm)), between 500 and 800 nm digitized every 5 nm with optical scale (definition) 0,5 nm. pH meter (universal ionometer pH-meter 150 MI, Minsk, Byelorussia) was used for the pH adjustments. The absorbance data from the spectrophotometer were collected in Excel. Analysis was performed in Matlab.

Reagents

Metal ions standard solutions (0,01 mol·L^{-1}) were prepared by the dissolution of metal shots of extra purity in nitric acid.

1-(2-pyridylazo)-2-naphthol (of the "Reanal" company) was additionally purified by recrystallization from isopropanol. A working solution of $4 \cdot 10^{-3}$ mol·L^{-1} concentration was prepared by dissolution of the necessary PAN shot in ethanol and making it up to the mark in a volumetric flask.

The SAS (Surface activity substance) solution – sodium ethoxydodecyl-sulphate with average molar weight of 700 (gel with a mass fraction of the basic substance of 70,1 %, manufacturer: "Cognis") was prepared with a mass fraction ω = 12,5% by dissolution of a shot in a distilled water.

The buffer solution containing 0,05mol/l $Na_2B_4O_7 \cdot 10H_2O$, 0,14 mol·L^{-1} $Na_2HPO_4 \cdot 2H_2O$, 0,2 mol·L^{-1} $Na_3C_6H_5O_7 \cdot 5{,}5H_2O$ and 0,06 mol·L^{-1} NaOH was used.

Procedure generation of two-dimensional spectra

Complex absorption spectra and their yield according to the pH were measured on a spectrophotometer-ionometer apparatus with pH-electrodes in a cell. The titrant (HCl, 0.5 mol·L^{-1}) moved through a flexible capillary from the microburet into a cell. After each step of a titrant addition, pH and absorbance measurements in λ = 520 - 600 nm range were carried out. Such measurements were done for the solution containing cations as well as for the solution in the blank run. After subtraction, the two-dimensional ion-complex absorption spectrum with the PAN according to λ and pH was acquired.

Aliquot part of solutions (no more than 6 ml) (Zn^{2+}, Cd^{2+} and Mn^{2+} cations) are brought into a 25 ml flask. Than 1ml of ascorbic acids (mass fraction is 10 %), 1 ml of the PAN are brought in, than alkali solution (*c*(NaOH) = 1,0 mol·L^{-1}) is added drop by drop until steady red colour occurs, than 10 ml of the buffer and 5 ml of SAS are added. After that the solution is made up to the volume with distilled water. 8 ml of aliquot is placed in a 1 cm-width cell and titrated with hydrochloric acid at 0,05 ml measuring absorbance and pH.

Preliminary correction of the measurement results

Calculations were carried out in Matlab 6.5 software.

The measured values of the array A(i, j) adjusted to reflect changes in the volume of the solution, A^{cor} (i, j), according to the equation (5), and then subjected to a cubic spline approximation - calculated value $A^{(0)}$(n_λ, n_{pH}) for pH_i = 7.0 +0,20 i (i = 0 ... n_{pH})

$$A^{cor}(i,j) = A(i,j) \cdot (V_0 + \Delta V_j) / V_0 \quad (5)$$

where, V_0 = 8,0 ml − volume aliquot of solution complexes; ΔV_j − the added volume of NaOH to the titration of V_0.

Design method

Calibration matrix (**E**(n_1,n_2)) of λ-pH coordinates breaks up in two vectors:

$$\mathbf{E}(n_\lambda, n_{pH}) = \mathbf{V}(n_\lambda, 1) \cdot \mathbf{Q}(n_{pH}, 1), \quad (6)$$

where, **V** – vector-spectrum of dimensional ion complex with PAN at pH of maximum emerge; **Q** – complex emerge vector according to pH; n_λ – wave length values at two-dimensional spectra; n_{pH} – pH values in which absorption coefficients were measured.

Components concentration is obtained by multiplying the two vectors (2):

$$\mathbf{E}(n_\lambda, n_{pH}) = \mathbf{V}(n_\lambda, 1) \cdot \mathbf{Q}(1, n_{pH}) \quad (7)$$

Components concentration is calculated by the following equation (3):

$$\mathbf{c} = \mathbf{V}^+ \cdot \mathbf{A}^{(0)} \cdot (\mathbf{Q}^+)^{\mathbf{T}} \quad (8)$$

where, $\mathbf{A}^{(0)}$ – the matrix of initial absorbance in the analyzed system, ($^+$) – indicates the matrix pseudo inversion $(\mathbf{V}^+ = (\mathbf{V}^{\mathbf{T}} \cdot \mathbf{V})^{-1} \cdot \mathbf{V}^{\mathbf{T}})$

However at such calculation the result will be correct only if $\mathbf{A}^{(0)}$ contains a two-dimensional spectrum of a single determinate component. In a multicomponent analysis determined concentrations are distorted by the presence of other absorptive components. In order to bring test results closer to the actual values it is proposed to use the method of successive approximations (consistent method of incorporating surface).

The first determined component is the one which first shows dependence of yield at the increasing of pH. After the estimation of the concentration by the equation (2), restoration of the response surface is carried out by the equation (4).

$$\mathbf{A1} = \mathbf{V}\ \mathbf{Q}\ \mathrm{c} \quad (9)$$

The **A1** surface in the area where the first component is emerging lies over **A**, and in the area of higher pH, we observe **A1** (i, j) <**A** (i, j). After element replacements by the following condition:

if **A**(i, j) – **A1**(i, j) > 0.001 then $\mathbf{A}^{(1)}$ (i, j) = **A1**(i, j), calculation by the equation (2) is carried out $\mathbf{c}^{(1)} = \mathbf{V}^{+}\mathbf{A}^{(1)} \cdot (\mathbf{Q}^{+})^{\mathrm{T}}$ After *k* successive approximations the result of $c^{(k)}$ does not change.

$^{(1)\,(2)\ldots.\,(k)}$ – number of iteration**.**

The second component concentration is calculated out of the difference matrix $\mathbf{AR}^{(0)} = \mathbf{A}^{(0)} - \mathbf{A}^{(k)}$ by the same algorithm. For the third component of the system the difference matrix $\mathbf{ARR}^{(0)} = \mathbf{AR}^{(0)} - \mathbf{AR}^{(k)}$ is used.

ACKNOWLEDGMENTS

Anatoliy V. Drozd, Olga S. Kalinenko, Natalia A. Leonova

REFERENCES

1. I.G. Perkov, A.V. Drozd, and G.V. Artsebashev, *J. Anal. Chem*., **1989**, *44*(8), 1465.
2. A.V. Drozd, and I.M. Baskir, *J. Anal. Chem*., **2002**, *57*(1), 20.
3. C.-N. Ho, G.D. Christian and E.R. Davidson, *Anal. Chem.,* **1978**, *50*, 1108.
4. A. Lorber, *Anal. Chem.,* **1985**, *57*, 2395.
5. H. Abdollahi and F. Nazari, *Anal. Chim. Acta*, **2003**, *486*, 109.
6. K. Zarei, A. Morteza and E. Abdinasab, *Eurasian J. Anal. Chem*, **2009**, *4(3)*, 314.
7. H. Abdollahi, A. Safavi and S. Zeinali, *Chemometrics and Intelligent Laboratory Systems*, **2008**, *94*, 112.
8. M. Bahram and M. Mabhooti*, Anal. Chim. Acta*, **2009**, *639*, 19.
9. Yating Liu, Jian Deng, Lin An, Jun Liang, Fei Chen and Hui Wang, *Food Chemistry*, **2011**, *126*, 2.
10. H. Abdollahi, A. Golshan, *Analytica Chimica Acta*, **2011**, *693*(1-2), 26-34.
11. Y. Liu, J. Deng, L. An, J. Liang, F. Chen, H. Wang, *Food Chemistry,* **2011**, *126* (2), 745-750.
12. A. Afkhami, F. Khajavi, H. Khanmohammadi, *Analytica Chimica Acta,* **2009**, *647*(2), 189-194.

STUDIA UBB CHEMIA, LVIII, 1, 2013 (p. 105 – 115)
(RECOMMENDED CITATION)

THERAPEUTIC MONITORING OF LEVOFLOXACIN: A NEW LC-MS/MS METHOD FOR QUANTIFICATION OF LEVOFLOXACIN IN HUMAN PLASMA

BRÎNDUŞA ŢILEA[a], LAURIAN VLASE[b], DANIELA-SAVETA POPA[b*], DANIELA PRIMEJDIE[b], DANIELA LUCIA MUNTEAN[c], IOAN ŢILEA[a]

ABSTRACT. A simple and sensitive liquid chromatography coupled with tandem mass spectrometry (LC-MS/MS) method for the quantification of levofloxacin in human plasma was developed and validated. The separation was performed on a Zorbax SB-C18 column under isocratic conditions using a mobile phase of 17:83 (v/v) acetonitrile and 0.1% (v/v) formic acid in water at 50ºC with a flow rate of 1 mL/min. The detection of levofloxacin was performed in multiple reaction monitoring (MRM) mode using an ion trap mass spectrometer with electrospray positive ionisation. The human plasma samples (0.1 mL) were deproteinised with methanol and aliquots of 1 µL from supernatants obtained after centrifugation were directly injected into the chromatographic system. The method shows a good linearity (r^2 > 0.99), precision (CV < 11%) and accuracy (bias < 4.7%) over the range of 0.1-10.0 µg/mL plasma. The lower limit of quantification (LLOQ) was 0.1 µg/mL and the recovery was between 95.2-104.5%. The method is not expensive, it needs a minimum time for plasma sample preparation and has a run-time of 1.3 min for instrument analysis (retention time of levofloxacin was 0.9 min). The developed and validated method is very simple, rapid and efficient, with wide applications in clinical level monitoring, pharmacokinetics and bioequivalence studies of levofloxacin.

Keywords: *levofloxacin, LC-MS/MS, therapeutic drug monitoring*

[a] *University of Medicine and Pharmacy Tirgu Mures, Faculty of Medicine, 38 Gh. Marinescu St., RO-540139, Tirgu Mures, Romania*
[b] *University of Medicine and Pharmacy "Iuliu Haţieganu", Faculty of Pharmacy, Emil Isac 13, RO-400023, Cluj-Napoca, Romania*
[c] *University of Medicine and Pharmacy Tirgu Mures, Faculty of Pharmacy, 38 Gh. Marinescu St., RO-540139, Tirgu Mures, Romania*
* *Corresponding author: dspopa@yahoo.com*

INTRODUCTION

Levofloxacin, (-)-(S)-9-fluoro-2,3-dihydro-3-methyl-10-(4-methyl-1-piperazinyl)-7-oxo-7*H*-pyrido[1,2,3-*de*]-1,4-benzoxazine-6-carboxylic acid (Fig.1), is a systemic drug from third generation of quinolones [1]. It is the active S-(-) enantiomer of ofloxacin and has bactericidal activity against a broad spectrum of gram-negative and gram-positive aerobes and atypical bacteria. It has limited activity against anaerobes [2]. Its therapeutic effectiveness is due to its capacity to inhibit two enzymes involved in bacterial DNA replication: the DNA gyrases and topoisomerase IV. Thus, levofloxacin affects DNA replication, transcription, repair and recombination. The effect is initially bacteriostatic but becomes bactericidal when bacteria are unable to repair the DNA lesions [Modern]. Therapeutic use of levofloxacin includes mainly urinary and respiratory tract infections, as well as systemic infections [3, 4].

The antibiotic activity of fluoroquinolones depends on the ratio of maximum drug concentration (Cmax) to minimum inhibitory concentration (MIC). Moreover, the ratio of the 24 h area under the concentration-time curve (AUC_{24}) of fluoroquinolones to MIC is an important predictor of treatment efficacy [5]. Therefore to have an effective dosage and to prevent bacterial resistance the monitoring of plasma concentrations of fluoroquinolones is recommended.

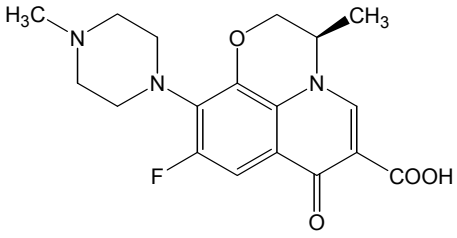

Figure 1. Chemical structure of levofloxacin

Levofloxacin is rapidly absorbed from the digestive tract and its oral bioavailability is ~99%. The peak plasma levels occur in 1-2 h. The therapeutic plasma concentrations are usually in the range of 0.5 - 6 μg/mL after oral administration or perfusion; Cmax can grow up to 12 μg/mL after high doses of levofloxacin. The plasma protein binding is between 30-40% and the drug is widely distributed in body tissues. Levofloxacin is excreted in the urine almost unchanged (80-85%) with a plasma elimination half-life of 6-8 h, being increased in renal impairment [1-3,6,7].

Several methods involving quantitative nuclear magnetic resonance spectrometry [8], capillary electrophoresis [9], high-performance thin-layer chromatography (HPTLC) [10] and high-performance liquid-chromatography (HPLC) with UV [11-16], fluorescence [5, 17-20] or mass spectrometric (MS)

[6, 21-23] detection have been reported to determine therapeutic levels of levofloxacin or ofloxacin in biological samples: serum [5] or plasma [8, 10, 14-23], urine [8, 14, 17], tissues [6, 22].

Liquid chromatography coupled with mass spectrometry has become increasingly popular in recent years, taking the place of conventional HPLC methods with UV, fluorescence or electrochemical detection due to its powerful performances. It is more rapid, usually requires a simple pre-treatment of samples, and offers an extraordinary selectivity, sensitivity and robustness [24-29]. The combination of HPLC with tandem mass spectrometry is becoming the method of choice for therapeutic drug monitoring and toxicology studies [30].

The aim of this study was to develop and validate a new simple and efficient LC/MS/MS assay for the quantification of levofloxacin in human plasma. This method will be applied in therapeutic drug monitoring, as well as in pharmacokinetics or bioavailability studies.

RESULTS AND DISCUSSION

The developed LC/MS-MS method was optimized and validated. It is rapid, with a total run time of instrumental analysis of 1.3 min and a retention time of levofloxacin of 0.9 min (Fig. 2). Sample preparation consisted only of protein precipitation. The volume of plasma required for processing was small, of 0.1 mL. All these features make the method ideal for routine analysis.

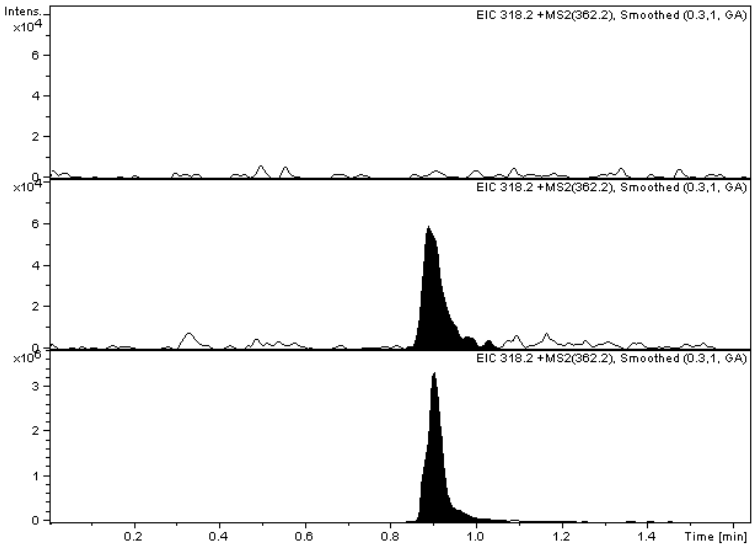

Figure 2. Representative chromatograms of (up) drug-free plasma, (middle) plasma spiked with levofloxacin at lower limit of quantification (0.1 μg/mL) and (down) plasma sample obtained from a patient 4 h after administration of 500 mg levofloxacin in perfusion (concentration found: 4.18 μg/mL).

The sensitivity of the developed method was good (LLOQ of 100 ng/mL), sufficient to determine therapeutic levels of levofloxacin, which are greater than 0.5 µg/mL. The absolute recoveries were high (between 91.4-100.1% at LLOQ, and 86.6-103.8% at 3.200 µg/mL, respectively).

Sample preparation

The assay sensitivity depends primarily on detection mode, but the method involved in sample preparation may also influence the chromatographic background level and can generate matrix suppression effect in LC-MS assays. An extraction step in plasma sample preparation to eliminate the impurities and to enhance sensitivity increases the time of analysis and the costs and can affect the recovery. In the method elaborated by Ji *et al.,* levofloxacin was isolated from plasma by extraction in dichloromethane, but even if the limit of quantification (LOQ) was 10 ng/mL, the recovery mean was only 55.5% [21]. In scientific literature, there are some LC-MS/MS methods that use precipitation of proteins (with acetonitrile or methanol) without extraction for the determination of levofloxacin in human plasma with better recoveries, > 70% (Table 1).

LC-MS/MS assay

The chromatographic conditions, especially the composition of mobile phase, were optimized in several trials to achieve maximum peak responses and symmetrical chromatographic peaks, a short retention time of levofloxacin and consequently a shorter run time of analysis. The best results were obtained with the mixture of acetonitrile and 0.1% (v/v) formic acid in water (17:83, v/v) under isocratic conditions.

In the case of levofloxacin, electrospray ionization (ESI) mode offers significantly higher signals compared to atmospheric pressure chemical ionization (APCI). The signal intensities of levofloxacin obtained in positive ion mode were much higher than those in negative ion mode, so the former ionization mode was chosen.

The direct MS detection is used for pharmaceutical purposes in qualitative rather than quantitative analysis. The use of tandem MS detection allows the obtention of better selectivity and sensitivity by the fragmentation of the molecular ion into several ions. After the collision that induced the dissociation of levofloxacin in ion trap mass spectrometer, the molecular ion $[M+H]^+$ (m/z 362.2) produced one abundant ion (m/z 318.2) $[M,H\text{-}CO_2]$ at the optimum collision energy of 1.2V (Fig. 3), thus, the detection of levofloxacin was carried out in multiple reaction monitoring (MRM) by monitoring the transition m/z 362.2 → m/z 318.2. No matrix interference or ion suppression was observed from the plasma samples.

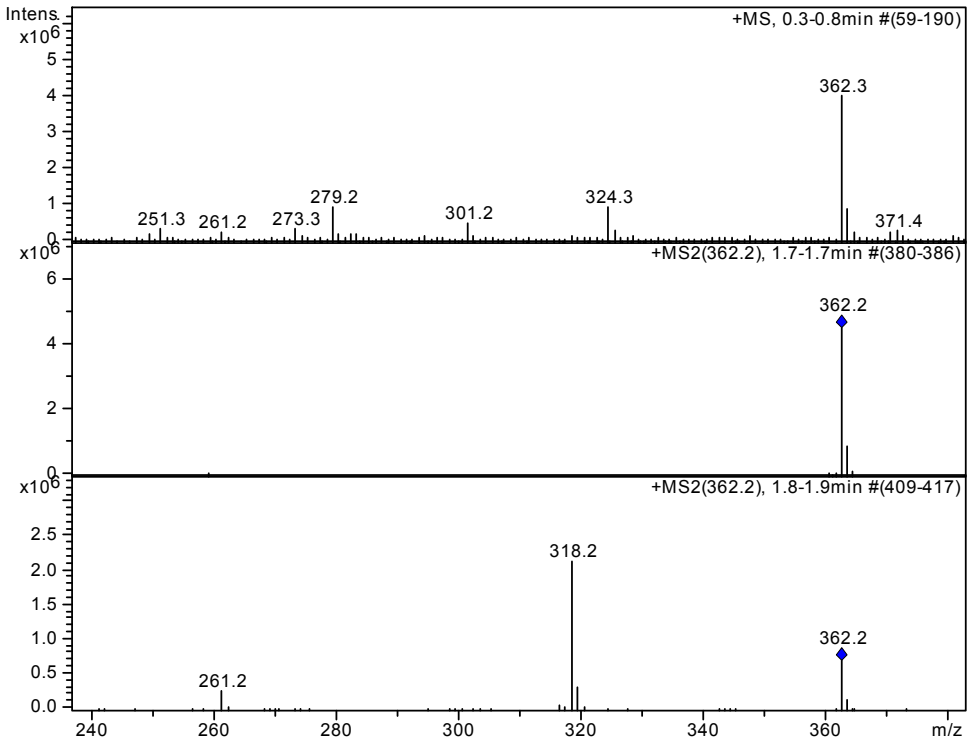

Figure 3. Mass spectra of levofloxacin obtained by electrospray ionisation in positive ion mode at the collision energy of 1.2V: (up) full-scan spectrum; (middle) MS spectrum of pseudo-molecular ion $[M+H]^+$; (down) MS/MS reactive spectrum (after fragmentation; monitored ion: m/z 318).

Other similar methods that operated in ESI(+)-MRM mode using the same transition monitoring were reported in the literature to quantify levofloxacin in plasma [22, 23] or other various samples as tissues samples [6], environmental water and swine wastewater [31, 32]. Of all these methods, those applied to plasma showed better sensitivity (LOQ < 100 ng/mL) using small volumes of plasma [22, 23] (Table 1) compared to that developed by us. However, our method is more rapid and has the characteristics of a high-throughput assay. It offers a shorter time of analysis and a lower cost in the case of routine measurements as compared to the other longer methods reported in literature (Table 1).

As the therapeutic plasma levels of levofloxacin are between 0.5-6 µg/mL, the LLOQ of 0.100 µg/mL established in our method can be accepted in bioequivalence studies and for routine purposes in therapeutic level monitoring of levofloxacin in human plasma.

Table 1. Analytical characteristics of some reported HPLC methods for the determination of levofloxacin or ofloxacin in human plasma or serum

Ref.	Matrix (mL)	Pre-treatment/ extraction[c]	Stationary phase	Mobile phase constituents[b]	Detection mode[a]	LOQ[d] (ng/mL)	Rt[e] (min)	Absolute recovery (%)
Our method	Plasma (0.1)	PP with methanol	Zorbax SB-C18	ACN: 0.1% (v/v) formic acid (17:83,v/v)	ESI-MS/MS, MRM (m/z 362.2 →318.2)	100	0.9	95.2-104.5
Ji [21]	Plasma (0.02)	ELL	HILIC Silica	ACN-100mM ammonium formate (pH 6.5) (82:18, v/v)	MS/MS, ESI, MRM (m/z 362.7→261.2)	10	1.9	55.2
Fang [22]	Plasma (0.15)	PP with MeOH	C4	MeOH-0.05% formic acid in water, gradient	ESI-MS/MS, MRM (m/z 362.1→318.1)	21.8	10.0	81.9-99.1
Meredith [23]	Plasma (0.02)	PP with ACN and MeOH	Phenomenex Luna, PFP	ACN-0.1% formic acid, gradient	ESI-MS/MS, MRM (m/z 362.1→318.3)	78	3.2	>70
Watabe [5]	Serum (0.20)	PP with $HClO_4$ and MeOH	Inertsil C8	ACN-1% TEA (pH 3) (14:86, v/v)	HPLC-FD	100	12.8	86.9-91.4
Wagen-lehner [17]	Serum (NA)	PP with ACN and $HClO_4$	Reversed phase	Citric acid buffer + ammonium perchlorate – ACN + ion pairing reagent (90:10,v/v)	HPLC-FD	2.34	NA[f]	NA
Tsaganos [19]	Plasma (0.50)	PP with ACN and trichloro-acetic acid	Nucleosil C18	25 mM sodium phosphate buffer (pH 3), 10 mM SDS: ACN (35:65, v/v)	HPLC-FD	390	2.9	NA
Zhou [20]	Plasma (0.1)	LLE	Kromasil C18	10mM phosphate buffer, pH 3.0 (with 0.01% TEA):ACN (76:24, v/v)	HPLC-FD	52.1	2.5	~86%
Siewert [18]	Plasma (0.05)	PP with trifluoro-acetic acid	YMC Pro C18	MeOH / 1.0 M ammonium acetate / H2O, gradient	HPLC-UV	100	8.3	97.2-104.7
Wong [14]	Plasma (NA)	LLE	Inertsil C18	NA (containing chiral reagents)	HPLC-UV	82	NA	NA
Kumar [15]	Plasma (0.5)	LLE	C18	20mM KH2PO4 buffer, pH 2.5:CAN (80:20, v/v)	HPLC-UV	100	5.9	~85%
Gao [16]	Plasma (0.5)	PP with HClO4	Kromasil C18	ACN:H2O:H3PO4: TEA (14:86:0.6:0.3, v/v/v/v)	HPLC-UV	50	8.4	89-98

[a] MRM, multiple reaction monitoring; FD, fluorescence detection; [b] MeOH, methanol; ACN, acetonitrile; TEA, triethylamine; [c] PP, protein precipitation; LLE, liquid-liquid extraction; [d] LOQ, limit of quantification; [e] Rt, retention time; [f] NA, not available.

Assay validation

The method was validated in accordance with international regulations [33, 34]. Representative chromatograms of drug-free plasma and plasma spiked with levofloxacin at LLOQ are shown in Fig. 2. No interfering peaks from the endogenous plasma components were observed in the retention time of levofloxacin.

The calibration curves were linear over the concentration range of 0.100 – 10 μg/mL in human plasma, with a correlation coefficient greater than 0.99. The LLOQ was 0.100 μg/mL. The values obtained for intra-day and inter-day precision and accuracy during the validation are shown in Tables 2 and 3, respectively.

All values for accuracy and precision were within recommended limits (<15%). The means of absolute recovery values were between 95% and 104.5%.

Method application

The validated method was used for therapeutic drug monitoring of levofloxacin (Fig. 2). As well other quinolones, levofloxacin has an excellent tissue and tissue fluid penetration, so it can be used for treatment of infections in a wide range of organ systems. It is available in both oral and intravenous formulations and one of its major advantages is the ability to treat many serious infections with oral or intravenous-oral switch regimens. Levofloxacin is used in treatment of urinary tract infections (pyelonefritis and complicated urinary tract infections, chronic bacterial prostatitis), respiratory tract infections (acute sinusitis, acute bacterial exacerbation of chronic bronchitis, community acquired pneumonia, skin and skin structure infection and post exposure prophylaxis and curative treatment after Anthrax inhalation (but treating physicians should refer to national consensus documents regarding the treatment of Bacillus anthracis).

Table 2. The intra-day precision (CV %), accuracy (bias %) and recovery data for the measurement of levofloxacin in human plasma (the analysis of five different samples, n = 5)

Nominal concentration (μg/mL)	Found concen-tration mean μg/mL	± SD	CV (%)	Bias (%)	Recovery (%)	± SD
0.100	0.103	0.010	9.3	3.2	95.5	4.1
0.200	0.209	0.006	3.1	4.6	97.6	5.8
0.800	0.779	0.050	6.5	-2.6	97.2	3.2
3.200	3.216	0.102	3.2	0.5	95.2	8.6

Table 3. The inter-day precision (CV %), accuracy (bias %) and recovery data for the measurement of levofloxacin in human plasma (one analysis on five different days, n = 5)

Nominal concentration (μg/mL)	Found concentration mean μg/mL	± SD	CV (%)	Bias (%)	Recovery (%)	± SD
0.100	0.104	0.011	11.0	3.9	95.9	4.2
0.200	0.203	0.019	9.5	1.5	97.3	3.7
0.800	0.762	0.044	5.8	-4.7	104.5	5.0
3.200	3.133	0.209	6.7	-2.1	98.5	1.3

CONCLUSION

The developed and validated LC-MS/MS assay is simple, rapid, and accurate having the characteristics required of the methods applied in therapeutic drug monitoring. The method was validated over the concentration range of 0.100-10 μg/mL which covers therapeutic plasma levels of levofloxacin. In comparison with other published HPLC [5, 14-20] or LC-MS/MS [21-23] methods for monitoring levofloxacin in human plasma, the developed method performs better in terms of volume of analyzed plasma sample, analyte recovery, and speed (both sample preparation and chromatographic run-time), which are essential attributes for methods used in routine analysis. This new fast method was successfully applied in therapeutic drug monitoring of levofloxacin. It can also be successfully used in pharmacokinetics and bioequivalence studies of levofloxacin.

EXPERIMENTAL SECTION

Reagents

Acetonitrile and methanol of isocratic grade for liquid chromatography, and formic acid of analytical-reagent grade were purchased from Merck KGaA (Darmstadt, Germany). Deionised water was obtained using a Milli-Q Water purification system (Millipore, Milford, MA, USA). The human blank plasma was supplied by the Regional Blood Transfusion Centre of Cluj-Napoca (Romania) from healthy volunteers, men and women.

Apparatus

The following apparatus were used: 204 Sigma Centrifuge (Osterode am Harz, Germany); Analytical Plus and Precision Standard Balance (Mettler-Toledo, Switzerland); Vortex Genie 2 mixer (Scientific Industries, New York,

USA); Ultrasonic bath Elma Transsonic 700/H (Singen, Germany). The HPLC system used was an 1100 series Agilent Technologies model (Darmstadt, Germany) consisting of two G1312A binary pumps, an in-line G1379A degasser, an G1329A autosampler, a G1316A column oven and an Agilent Ion Trap Detector 1100 VL.

Chromatographic and spectrometric conditions

Chromatographic separation was performed on a Zorbax SB-C18 (100 mm x 3.0 mm i.d., 3.5 μm) column (Agilent Technologies) under isocratic conditions using a mobile phase of a 17:83 (v/v) mixture of acetonitrile and 0.1% (v/v) formic acid in water at 50 ºC with a flow rate of 1 mL/min. The detection of levofloxacin was performed in multiple reaction monitoring (MRM) mode using an ion trap mass spectrometer with an electrospray ion (ESI) source, positive ionisation (capillary 4000 V, nebulizer 60 psi (nitrogen), dry gas nitrogen at 12 L/min, dry gas temperature 350ºC). The extracted ion current (EIC) chromatogram of m/z 318 from m/z 362 was analysed.

Standard solutions

A stock solution of levofloxacin (5 mg/mL) was prepared by dissolving an appropriate quantity of levofloxacin in methanol. A working solution (10 µg/mL) was prepared by appropriate dilution in drug-free human plasma. This solution was used to prepare plasma calibration standards with the concentrations of 0.100, 0.200, 0.400, 0.800, 1.600, 3.200, and 10.00 µg/mL. Quality control (QC) samples of 0.200 µg/mL (low), 0.800 µg/mL (medium) and 3.200 µg/mL (high) were prepared by adding the appropriate volumes of working solution to drug-free human plasma. The resultant plasma calibration standards and quality control standards were pipetted into 15 mL polypropylene tubes and stored -20ºC until analysis.

Sample preparation

Standards and plasma samples (0.1 mL) were deproteinised with methanol (0.3 mL). After shaking with vortex-mixer (10 s) and centrifugation (5 min at 10.000 rpm), the supernatants (0.2 mL) were transferred in autosampler vials and 1 µL were injected into the HPLC system.

Method validation

The specificity of the method was evaluated by comparing the chromatograms obtained from the plasma samples containing levofloxacin with those obtained from different plasma blank samples (n=6).

The concentration of levofloxacin was determined automatically by the instrument data system using peak areas and the external standard method. The calibration curve model was determined by the least squares analysis: $y = b + ax$, weighted ($1/y^2$) linear regression, where y - peak area of the analyte and x - concentration of the analyte (µg/mL).

The intra-day precision (expressed as coefficient of variation, CV %) and accuracy (expressed as relative difference between obtained and theoretical concentration, bias %) were determined by the analysis of five different samples (n = 5) from each QC standards (at lower, medium and higher levels) on the same day. The inter-day precision and accuracy were determined by analysis on five different days (n = 5) of one sample from each QC standards (at low, medium and high levels).

The lower limit of quantification (LLOQ) was established as the lowest calibration standard with an accuracy and precision less than 20%.

The relative recoveries (at LLOQ, low, medium and high levels) were measured by comparing the response of the spiked plasma with the response of standards in solvent with the same concentration of levofloxacin as the plasma (n = 5).

REFERENCES

1. A.C. Moffat, M.D. Osselton, B. Widdop, “Clarke’s Analysis of Drug and Poisons in pharmaceuticals, body fluids and postmortem material”, Pharmaceutical Press, Inc, London, **2011**.
2. D. Sarisaltik, *FABAD J Pharm Sci.,* **2007**, *32*, 197.
3. P. Anderson, J. Knoben, W. Troutman, “Handbook of clinical drug data”, 10th ed., McGraw-Hill, New York, **2002**, 167.
4. M.A. Miller-Hjelle, V. Somaraju, J.T. Hjelle, “Synthetic Organic Antimicrobials: Sulfonamides, Trimethoprim, Nitrofurans, Quinolones, Methenamine”, in: C.R. Craig, R.E. Stitzel, “Modern Pharmacology with Clinical Applications”, 6th ed., Lippincott Williams & Wilkins, **2004**, 519.
5. S. Watabe, Y. Yokoyama, K. Nakazawa, K. Shinozaki, R. Hiraoka, K. Takeshita, Y. Suzuki, *J. Chromatogr. B Analyt. Technol. Biomed. Life. Sci*., **2010**, *878*, 1555.
6. D. Bao, T.T. Truong, P.J. Renick, M.E. Pulse, W.J. Weiss. *J. Pharm. Biomed. Anal.,* **2008**, *46*, 723.
7. M. Weinrich, S. Scheingraber, T. Stremovskaia, M.K. Schilling, F. Kees, G.A. Pistorius, *Int. J. Antimicrob. Agents*, **2006**, *28*, 221.
8. A.A, Salem, H.A. Mossa, *Talanta,* **2012**, *88,* 104.
9. M. Hernández, F. Borrull, M. Calull, *J. Chromatogr. B Biomed. Sci. Appl.,* **2000***, 742,* 255.
10. J.F. Galan-Herrera, J.L. Poo, O. Rosales-Sanchez, E. Fuentes-Fuentes, L. Cariño, V. Burke-Fraga, S. Namur, M.G. Parra, *Clin. Ther.,* **2009***, 31*, 1796.

11. L. Baietto, A. D'Avolio, F.G. De Rosa, S. Garazzino, S. Patanella, M. Siccardi, M. Sciandra, G. Di Perri, *Ther. Drug Monit.,* **2009***, 31,* 104.
12. A. Das, J. Mukherjee, G. Dey, A.K. Sarkar, B.K. Sahoo, U.S. Chakrabarty, U. Nandi, T.K. Pal, *Arzneimittelforschung,* **2011***, 61*, 61.
13. H. Liang, M.B. Kays, K.M. Sowinski, *J. Chromatogr. B Analyt. Technol. Biomed. Life Sci.,* **2002***, 772*, 53.
14. F.A. Wong, S.J. Juzwin, S.C. Flor, *J. Pharm. Biomed. Anal*., **1997**, *15*, 765.
15. T.M. Kumar, G. Srikanth, J.V. Rao, K.S. Rao, *Int. J. Pharm. Pharm. Sci*., **2011**, *3*, 247.
16. X.X. Gao, G.C. Yao, N. Guo, F. An, X.J. Guo, *Drug Discov Ther*., **2007**, *1*, 136.
17. F.M. Wagenlehner, M. Kinzig-Schippers, U. Tischmeyer, C. Wagenlehner, F. Sörgel, A. Dalhoff, K.G. Naber, *Int. J. Antimicrob. Agents,* **2006***, 27*, 7.
18. S. Siewert, *J. Pharm. Biomed. Anal.,* **2006***, 41*, 1360.
19. T. Tsaganos, P. Kouki, P. Digenis, H. Giamarellou, E.J. Giamarellos-Bourboulis, K. Kanellakopoulou, *Int. J. Antimicrob. Agents,* **2008***, 32,* 46.
20. Z.L. Zhou, M. Yang, X.Y. Yu, H.Y. Peng, Z.X. Shan, S.Z. Chen, Q.X. Lin, X.Y. Liu, T.F. Chen, S.F. Zhou, S.G. Lin, *Biomed Chromatogr*., **2007**, *21*, 1045.
21. H.Y. Ji, D.W. Jeong, Y.H. Kim, H.H. Kim, D.R. Sohn, H.S. Lee, *J. Pharm. Biomed. Anal.,* **2006***, 41,* 622.
22. P.F. Fang, H.L. Cai, H.D. Li, R.H. Zhu, Q.Y. Tan, W. Gao, P. Xu, Y.P. Liu, W.Y. Zhang, Y.C. Chen, F. Zhang, *J. Chromatogr. B Analyt. Technol. Biomed. Life Sci.,* **2010***, 878*, 2286.
23. S.A. Meredith, P.J. Smith, J. Norman, L. Wiesner, *J. Pharm. Biomed. Anal.,* **2012***, 58,* 177.
24. L. Vlase, S. Vancea, C. Mircioiu, C.E. Lupusoru, D. Marchidan, C.M. Ghiciuc, *Studia UBB Chemia*, **2011**, *56*, 181.
25. D.S. Popa, B. Kiss, L. Vlase, A. Pop, R. Iepure, R. Paltinean, F. Loghin, *Farmacia,* **2011***, 59*, 539.
26. L. Vlase, D.S. Popa, C. Siserman, D. Zaharia, *Rom. J. Leg. Med.*, **2011**, *19*, 145.
27. L. Vlase, D. Muntean, M. Cuciureanu, R. Cuciureanu, S. Gocan, *J. Liq. Chromatogr.& Related Tech*., **2011***, 34*, 436.
28. L. Vlase, D. Muntean, M. Achim, *Studia UBB Chemia,* **2010***, 55*, 305.
29. D.S. Popa, L. Vlase, D. Chirila, F. Loghin, *Rom. Rev. Lab. Med.,* **2010***, 18*, 37.
30. Q.A. Xu, T.L. Madden, "Analytical Methods for Therapeutic Drug Monitoring and Toxicology", John Wiley & Sons, New Jersey, **2011**.
31. L. Tong, P. Li, Y. Wang, K. Zhu, *Chemosphere,* **2009***, 74,* 1090.
32. G.A. Khan, R. Lindberg, R. Grabic, J. Fick. *J. Pharm. Biomed. Anal.,* **2012***, 66*, 24.
33. Guidance for Industry, Bioanalytical Method Validation. U.S. Department of Health and Human Services, Food and Drug Administration. Federal Register, **2001**, *66*.
34. Guidance on the Investigation of Bioavailability and Bioequivalence. The European Agency for the Evaluation of Medicinal Products, Committee for Proprietary Medicinal Products, **2001**, CPMP/EWP/QWP/1401/98.

STUDIA UBB CHEMIA, LVIII, 1, 2013 (p. 117 – 131)
(RECOMMENDED CITATION)

ASSESSMENT OF MASS AND ENERGY INTEGRATION ASPECTS FOR IGCC POWER PLANTS WITH CARBON CAPTURE AND STORAGE (CCS)

CALIN-CRISTIAN CORMOS[a*], CRISTIAN DINCA[b]

ABSTRACT. Integrated Gasification Combined Cycle (IGCC) is a power generation technology in which solid fuel is partially oxidized by oxygen and steam / water to produce a combustible gas called syngas. Syngas can then be used either for power generation or processed to various chemicals (hydrogen, ammonia, methanol etc.). Carbon Capture and Storage (CCS) represent a group of technologies aimed to capture CO_2 from energy-intensive processes and then stored for long period of time in suitable geological locations. This paper evaluates in details mass and energy integration aspects for an IGCC power plant fitted with pre- and post-combustion carbon capture configurations based on gas-liquid absorption processes (chemical and physical solvents).

Case studies analyzed in the paper are using coal to produce around 375 - 485 MW net electricity simultaneous with capturing about 90 % of the carbon contained in the feedstock. Two carbon dioxide capture options (post- and pre-combustion capture options) are compared with the situation of no carbon capture in term of mass and energy integration aspects as well as quantification of overall energy penalties. Plant options (no capture, pre-combustion and post-combustion capture) are modelled using ChemCAD and the simulation results used to asses integration aspects as well as overall plant performance indicators.

Keywords: *Gasification; Carbon Capture and Storage (CCS); Process integration*

INTRODUCTION

Energy issue is important and actual considering the need of security for energy supply, environmental protection and climate change prevention by reducing the greenhouse gas emissions. It is known that solid fossil fuels

[a] *Babes-Bolyai University, Faculty of Chemistry and Chemical Engineering, Arany Janos 11, RO-400028, Cluj-Napoca, Romania*
[b] *Politehnica University, Faculty of Power Engineering, 313 Splaiul Independentei, RO-060042, Bucharest, Romania*
* *Corresponding author: cormos@chem.ubbcluj.ro*

reserves (mainly coal and lignite) ensure a greater energy independence compared with liquid fossil fuels (oil) or gaseous fossil fuels (natural gas) [1], but coal utilization is looked with concern because of bigger greenhouse gas emissions (CO_2). For example, for production of one MWh electricity, the carbon dioxide emission in case of natural gas is about 350 – 400 kg and in case of coal about 800 – 900 kg [2-3]. The main aim of this paper is to evaluate the main mass and energy integration aspects of various carbon dioxide capture options (pre- and post-combustion capture both based on gas-liquid absorption processes) applicable to the energy conversion process by solid fuel gasification.

For climate change mitigation, a special attention is given to the reduction of CO_2 emissions by capture and storage techniques (CCS) [4]. From the point of view of carbon capture, there are several technological options, the most important are: post-combustion capture from flue gases, pre-combustion capture, oxy-combustion, chemical looping etc. [5-6]. After capturing, CO_2 must be stored safely for a long period of time, several practical options are under evaluation: storage in geological reservoirs, storage in exhausted oil and gas reservoirs, enhanced oil recovery (EOR) or injection in coal beds that cannot be mined due to the high depth (Enhanced Coal Bed Methane Recovery - ECBM) [6].

In this paper, the authors have analysed pre-combustion and post-combustion capture options of carbon dioxide using physical and chemical solvents [7-10]. The evaluated power generation technology is based on coal gasification (partial oxidation). These two carbon capture options are in the development and implementation stage to be applied within the power sector. The power plant concepts evaluated in this paper generate about 375 - 485 MW electricity using a Combined Cycle Gas Turbine (CCGT). Three plant configurations were analyzed in details by mathematical modelling and simulation:

Case 1: Conventional IGCC technology, no carbon capture;
Case 2.a: IGCC with pre-combustion capture using physical (Selexol®) solvent, 90% carbon capture rate;
Case 2.b: IGCC with pre-combustion capture using chemical (Methyl-DiEthanol-Amine - MDEA) solvent, 90% carbon capture rate;
Case 3: IGCC with post-combustion capture using chemical (Methyl-DiEthanol-Amine - MDEA) solvent, 90% carbon capture rate.

PLANT CONFIGURATIONS AND DESIGN ASSUMPTIONS

Conventional IGCC technology for power production is a thermo-chemical process in which the solid feedstock is partially oxidized with oxygen and steam to produce syngas (a mixture of H_2 and CO). Syngas is then desulphurised

in an Acid Gas Removal (AGR) system in which H_2S is captured from the syngas and send to a Claus plant to be partially oxidised to sulphur. Syngas is then burned in a gas turbine (GT) to generate power (syngas-fuelled gas turbine). Hot flue gases from the GT are used to raise steam which is then expanded in a steam turbine (ST) to generate power.

Recently the gasification technology received renew interest due to promising reduced energy and cost penalty for carbon capture as well as the potential to be operated in multi-fuel multi-product scenario. This means that IGCC power plant are able to process lower grade fuels compared with combustion processes as well as the capability to poly-generate various total or partial decarbonised energy vectors (power, hydrogen, substitute natural gas, liquid fuels by Fischer - Tropsch synthesis).

Conceptual layout of a modified IGCC scheme for power generation with carbon dioxide capture using pre-combustion option is presented in Figure 1 [9,11].

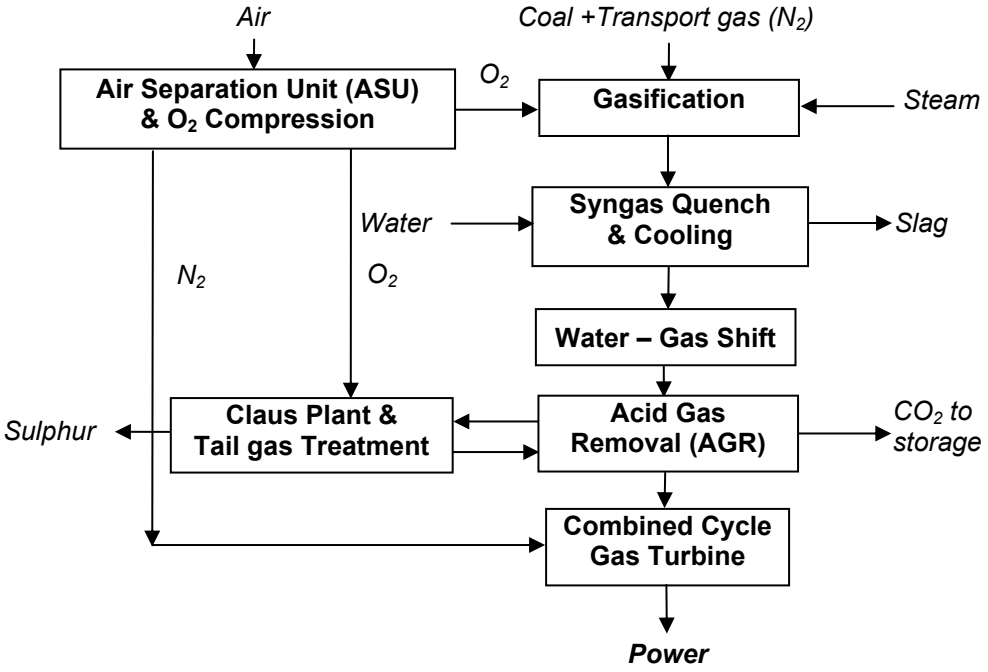

Figure 1. Layout of IGCC scheme for power production with CO_2 pre-combustion capture

The main differences of IGCC with pre-combustion CO_2 capture scheme compared with a conventional IGCC scheme without carbon capture is the presence of water gas shift (WGS) stage of carbon monoxide (having the role to concentrate the carbon species in the form of CO_2 that can be later captured) and a bigger Acid Gas Removal (AGR) system which captures, in addition of hydrogen sulphide as in the conventional technology, also carbon dioxide [11]. The decarbonised gas (hydrogen-rich gas) is then used in a combined cycle gas turbine to produces power (hydrogen-fuelled gas turbine).

The other IGCC-based carbon capture option evaluate in the paper is the post-combustion method in which the carbon dioxide is captured from the flue gases produced by syngas burning in the gas turbine. Basically, this option is similar with and IGCC power plant is which the gas turbine fuel gases are treated for CO_2 capture. The conceptual layout of an IGCC scheme for power generation with carbon capture using post-combustion option is presented in Figure 2 [12].

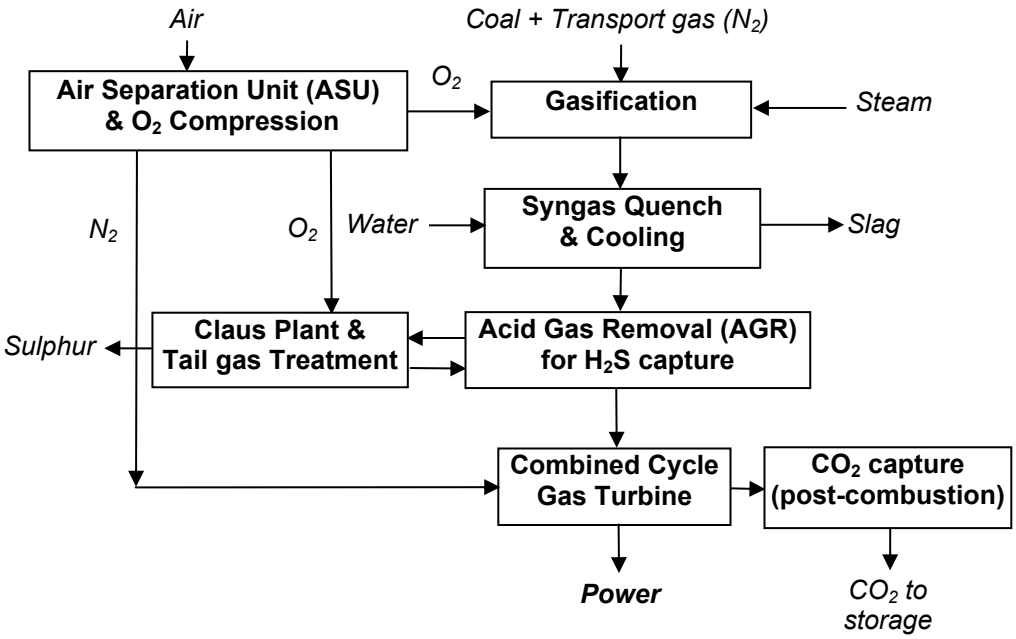

Figure 2. Layout of IGCC scheme for power production with CO_2 post-combustion capture

For the case studies analyzed in this paper, coal was considered as feedstock (fuel characteristics being presented in Table 1).

Table 1. Fuel (coal) characteristics

Parameter	Coal
Proximate analysis (% wt.)	
Moisture	8.10
Volatile matter	28.51
Ash	14.19
Ultimate analysis (% wt.)	
Carbon	72.04
Hydrogen	4.08
Nitrogen	1.67
Oxygen	7.36
Sulphur	0.65
Chlorine	0.01
Ash	14.19
Lower heating value - LHV (MJ/kg a.r.)	25.353

As gasification reactor, the option was in favour of entrained flow type operating at high temperature (slagging conditions) which give a high conversion of solid fuel (~99%). From different gasification technologies available on the market, Shell technology was chosen, the main factors for consideration were dry feed design of the gasifier and syngas quench which ensure the high energy efficiency [13].

Other main sub-systems of the plant and theirs design assumptions used in the modelling and simulation are presented in Table 2 [9,14].

Table 2. Main design assumptions

Unit	Parameters
Air Separation Unit (ASU)	Oxygen purity: 95% (vol.) Delivery pressure: 2.37 bar Power consumption: 225 kWh/ton O_2 No air integration with gas turbine
Gasification reactor (Shell)	Oxygen / solid fuel ratio (kg/kg): 0.84 Steam / solid fuel ratio (kg/kg): 0.12 Nitrogen / solid fuel ratio (kg/kg): 0.09 O_2 pressure to gasifier: 48 bar Pressure: 40 bar Temperature: >1400^{o}C Carbon conversion: 99.9 % Syngas quench
Shift conversion (Cases 2.a and 2.b)	Sulphur tolerant catalyst Two adiabatic beds Pressure drop: 1 bar / bed

Unit	Parameters
Acid Gas Removal - AGR (all cases)	Solvent: Selexol®; H_2S capture only Solvent regeneration: thermal (heat)
CO_2 pre-combustion capture (Cases 2.a and 2.b)	Solvent: Selexol®, MDEA Separate H_2S and CO_2 capture Selexol regeneration: pressure flash 4 levels: 12 bar / 5 bar / 2 bar and 1.05 bar MDEA regeneration: thermal (heat)
CO_2 post-combustion capture (Case 3)	Solvent: MDEA (Methyl-DiEthanol-Amine); Solvent regeneration: thermal (heat)
CO_2 compression and drying (Cases 2 and 3)	Delivery pressure: 100 bar Compressor efficiency: 85% Solvent used for drying: TEG
Claus plant & tail gas treatment	Oxygen-blown H_2S-rich gas composition: > 20% (vol.)
Gas turbine	Type: M701G2 Net power output: 334 MW Power efficiency: 39.5% Pressure ratio: 21 Turbine outlet temperature (TOT): 588^oC
Heat Recovery Steam Generator (HRSG) and steam cycle (Rankine)	Three pressure levels: 118 / 34 / 3 bar MP steam reheat Steam turbine isoentropic efficiency: 85% Steam wetness ex. steam turbine: max. 10%
Heat exchangers	ΔTmin. = 10^oC Pressure drop: 1 % of inlet pressure

Captured CO_2 stream has to comply with a quality specification considering the final use. Considering transport (pipeline) and storage option (EOR or aquifers), CO_2 stream has to have very low concentration of water (<500 ppm) and hydrogen sulphide (<100 ppm) as these components could give corrosion problems along the pipeline network [15].

MODELING AND SIMULATION OF PLANT CONCEPTS

The three IGCC-based energy conversion processes described above: Case 1 – Conventional IGCC without carbon capture; Case 2 – IGCC with pre-combustion capture and Case 3 – IGCC with post-combustion carbon capture were mathematical modelled and simulated using ChemCAD and Thermoflex software. As thermodynamic package used in simulations, Soave-Redlich-Kwong (SRK) model was chosen considering the chemical species present and process operating conditions (pressure, temperature etc.).

Simulation of plant configurations yields all necessary process data (mass and molar flows, composition, temperatures, pressures, power generated and consumed) that are needed to assess the mass and energy integration aspects as well as the overall performance of the processes.

The following key plant performance indicators were used:

- *Cold gas efficiency* (CGE) shows the overall efficiency of the gasification process (conversion of solid fuel into syngas) and it is calculated with the formula:

$$CGE = \frac{Syngas\ thermal\ energy\ [MW_{th}]}{Feedstock\ thermal\ energy\ [MW_{th}]} * 100 \quad (1)$$

- *Syngas treatment efficiency* (STE) indicates the energy losses through the syngas conditioning line (shift conversion) and acid gas removal (AGR) system. This indicator is calculated with the formula:

$$STE = \frac{Syngas\ thermal\ energy\ ex.\ AGR\ [MW_{th}]}{Syngas\ thermal\ energy\ ex.\ quench\ [MW_{th}]} * 100 \quad (2)$$

- *Gross and net electrical efficiency* (η_{gross} and η_{net}) shows the overall plant performance in term of overall energy conversion process. These indicators are calculated as follow:

$$\eta_{gross} = \frac{Gross\ power\ output\ [MW_e]}{Feedstock\ thermal\ energy\ [MW_{th}]} * 100 \quad (3)$$

$$\eta_{net} = \frac{Net\ power\ output\ [MW_e]}{Feedstock\ thermal\ energy\ [MW_{th}]} * 100 \quad (4)$$

- *Carbon capture rate* (CCR) is calculated considering the molar flow of captured carbon dioxide divided with carbon molar flow from the feedstock:

$$CCR = \frac{Captured\ CO_2\ molar\ flow\ [kmole/h]}{Feedstock\ carbon\ molar\ flow\ [kmole/h]} * 100 \quad (5)$$

- *Specific CO_2 emissions* (SE_{CO_2}) are calculated considering emitted CO_2 mass flow for each MW power generated:

$$SE_{CO_2} = \frac{Emitted\ CO_2\ mass\ flow\ [kg/h]}{Net\ power\ generated\ [MW_e]} * 100 \quad (6)$$

In term of ancillary energy consumptions (power, heat and cooling water) for CCS cases, the following indicators was used:

- *Specific power consumption* (SPC) are calculated considering the power consumption for captured CO_2 mass flow:

$$SPC = \frac{Ancillary\ power\ consumption\ [MW_e]}{Captured\ CO_2\ mass\ flow\ [kg/h]} * 100 \quad (7)$$

- *Specific heating consumption* (SHC) are calculated considering the heating consumption for captured CO_2 mass flow:

$$SHC = \frac{Ancillary\ heating\ consumption\ [MW_{th}]}{Captured\ CO_2\ mass\ flow\ [kg/h]} * 100 \quad (8)$$

- *Specific cooling consumption* (SCC) are calculated considering the cooling consumption for captured CO_2 mass flow:

$$SCC = \frac{Ancillary\ cooling\ consumption\ [MW_{th}]}{Captured\ CO_2\ mass\ flow\ [kg/h]} * 100 \quad (9)$$

MASS AND ENERGY INTEGRATION ASPECTS

The simulation results of all investigated case studies were used to assess mass and energy integration aspects. The most important in term of evaluating overall energy conversion process are the heat and power integration analysis of the gasification island and syngas conditioning line (first system) and the power block (Combined Cycle Gas Turbine - CCGT) as the second system. For optimisation of energy efficiency the steam raised in the gasification island was used to cover the ancillary heating consumptions (e.g. solvent regeneration), the rest was integrated in the Rankine cycle of the power block. On the other hand, cold condensate from the steam turbine was pre-heated in the syngas conditioning line and then returned back to Heat Recovery Steam Generator (HRSG).

As illustrative example, Table 3 presents the steam cycle parameters for Case 2.a (Shell-based IGCC with pre-combustion capture using Selexol).

The simulation results were used to perform energy integration analysis (pinch analysis) for optimisation of overall energy efficiency. Hot and cold composite curves (HCC and CCC) as well as grand composite curves of gasifier island & syngas conditioning line and power block were constructed. As minimum approach temperature, a conservative value of 10°C was chosen [16-17]. Considering Case 2.a as illustrative example, Figure 3 presents composite curves and grand composite curves for gasification island and syngas conditioning line (including WGS reactors) and Figure 4 presents the same curves for power block (CCGT).

Table 3. Steam cycle parameters - Case 2.a

Stream	Flowrate (t/h)	Temperature (°C)	Pressure (bar)
HP steam from WGS reactors	188.00	326.94	120.00
HP steam from gasifier	243.85	420.00	120.00
HP steam to HP Steam Turbine	689.85	576.10	118.00
MP steam to MP reheater	384.35	392.24	34.00
MP steam to process units	305.50	417.55	41.00
LP steam from process units	89.50	208.69	3.00
LP steam to LP Steam Turbine	596.85	172.93	3.00
LP steam (6.5 bar) to process units	29.00	229.81	6.50
LP Steam Turbine exhaust	596.85	31.32	0.046
Cooling water to steam condenser	30500.00	15.00	2.00
Cooling water from steam condenser	30500.00	25.00	1.80
Hot condensate returned to HRSG	931.77	115.00	2.80
BFW to HP BFW pumps	683.00	115.00	2.80
BFW to MP BFW pumps	70.00	115.00	2.80
BFW to LP BFW pumps	171.50	115.00	2.80
Flue gas at stack	2813.64	99.98	1.02

As can be observed from Figures 3 and 4, significant heat recovery is done in form of HP steam from gasifier island (syngas boiler) and syngas conditioning line (WGS reactors) [18-19]. The first aspect is a specific feature of syngas quench gasifiers (e.g. Shell, E-Gas) and it confers a higher energy efficiency compared with water quench gasifiers (e.g. GE-Texaco, Siemens). The second mentioned aspect (WGS reactors) are common to all IGCC-based CCS configurations with pre-combustion capture. Shift reaction is exothermic and it gives the capability of HP steam raising but also it reduce the overall thermal energy send to the combined cycle [20]. This important aspect can be noticed by comparing syngas-fuelled and hydrogen-fuelled CCGTs.

Table 4 presents the specific power, heating and cooling consumptions of all investigated CCS cases, in addition another physical solvent - Rectisol® was evaluated. As can be noticed Selexol® process has the lower penalty in terms of energy consumption. Comparing the two physical solvents (Selexol® and Rectisol®), for Rectisol® the overall net efficiency is about 0.5 % lower than in case of Selexol for the same carbon capture rate. However, Rectisol has also some merits for instance the deeper syngas cleaning of undesirable components (e.g. H_2S). This is of particular importance in chemical applications (e.g. ammonia synthesis) where lower H_2S concentrations (<10 ppm) in the syngas are desirable.

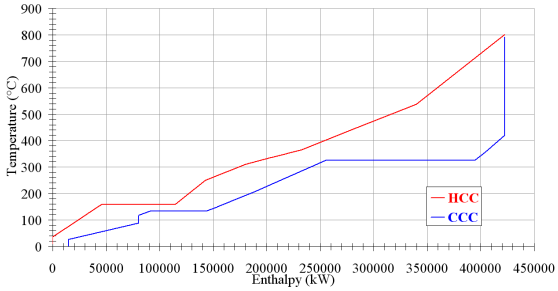

3.a. Hot and cold composite curves

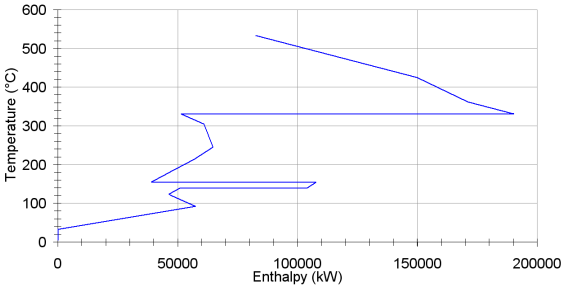

3.b. Grand composite curve

Figure 3. Energy integration analysis for gasification island and syngas conditioning line (Case 2.a)

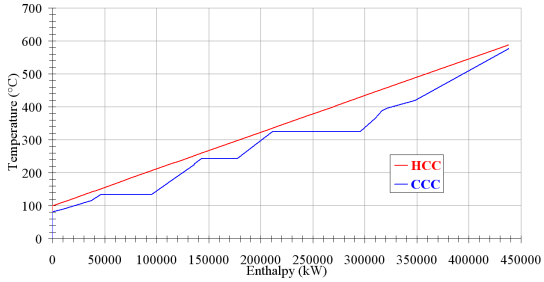

4.a. Hot and cold composite curves

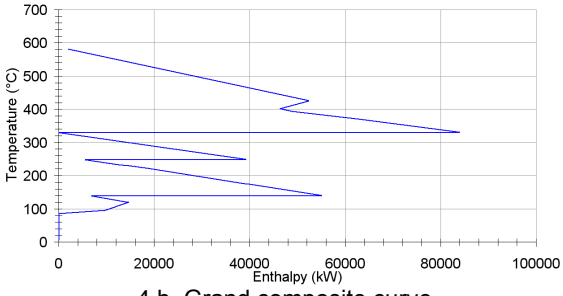

4.b. Grand composite curve

Figure 4. *Energy integration analysis for the power block (CCGT) (Case 2.a)*

Table 4. Energy consumptions pre- and post-combustion capture cases

Ancillary duty	Units	Pre-comb. Case 2.a Selexol®	Pre-comb. Rectisol®	Case 2.b MDEA	Post-comb. Case 3 MDEA
SPC	kWh/kg CO_2	0.1078	0.1185	0.0949	1.35
SHC	MJ/kg CO_2	0.2236	0.3739	0.7016	2.80
SCC	MJ/kg CO_2	0.5591	0.6154	3.3143	3.72

Table 4 reveals the main causes of significant energy penalty for post-combustion cases (not only for gasification but also for combustion power plants) namely high power and heat (steam) consumption [21].

To have a clearer picture about the impact of CCS technology in IGCC power plants, Table 5 presents normalised mass and energy balances for generation of 1 MWh net power using Shell gasifier (Case 1a vs. Case 1b). As can be noticed from Table 5, the introduction of carbon capture implies a significant increase of all normalised mass and energy flows for instance 25% for coal, 24% for oxygen, 22% for cooling water etc.

Table 5. Normalised mass and energy balances for Case 1 vs. Case 2.a

Input	Units	Value		Output	Units	Value
Case 1						
Coal	kg	304.62		Net power	MWh_e	1.00
Nitrogen	kg	468.74		Captured CO_2	kg	0.00
Oxygen	kg	257.10		Flue gases	kg	5922.52
Air	kg	5025.10		Sulphur	kg	1.83
Cooling water	kg	73148.66		Ash (dry)	kg	39.61
Fresh water	kg	41.22		Process water	kg	134.05
Energy (coal)	MWh_{th}	2.15		Cooling water	kg	73148.66
				Thermal energy (CW)	MWh_{th}	0.92
Case 2.a						
Coal	kg	382.53		Net power	MWh_e	1.00
Nitrogen	kg	489.71		Captured CO_2	kg	847.17
Oxygen	kg	320.11		Flue gases	kg	6495.31
Air	kg	5861.57		Sulphur	kg	2.26
Cooling water	kg	89018.98		Ash (dry)	kg	49.75
Fresh water	kg	670.44		Process water	kg	327.10
Energy (coal)	MWh_{th}	2.69		Cooling water	kg	89018.98
				Thermal energy (CW)	MWh_{th}	1.03

RESULTS AND DISSCUSSIONS

After performing mass and energy integration analysis, the results were used for quantification of overall key performance indicators of evaluated power plants concepts. Tables 6 and 7 presents overall plant performance indicators of analysed case studies in comparison with the plant concept without CCS. Table 6 is presenting the evaluation of pre-combustion capture (Case 2.a: Shell-based IGCC power plant with Selexol-based pre-combustion capture and Case 2.b: Shell-based IGCC power plant with MDEA-based pre-combustion capture) and Table 7 for post-combustion capture (Case 3: Shell-based IGCC power plant with MDEA-based post-combustion capture).

Table 6. Overall plant performance indicators - pre-combustion capture

Main Plant Data	Units	Case 1	Case 2.a	Case 2.b
Coal flowrate (a.r.)	t/h	147.80	165.70	165.70
Coal LHV (a.r.)	MJ/kg		25.353	
Coal thermal energy (A)	MW_{th}	1040.88	1166.98	1166.98
Raw syngas energy (B)	MW_{th}	839.05	934.76	934.76
Cold gas efficiency (B/A * 100)	%	80.61	80.10	80.10
Syngas exit AGR energy (C)	MW_{th}	835.41	831.92	831.92
Treatment efficiency (C/B *100)	%	99.56	88.99	88.99
Gas turbine output (M701G2)	MW_e	334.00	334.00	334.00
Steam turbine output	MW_e	224.01	210.84	200.72
Expander power output	MW_e	0.68	0.78	1.18
Gross electric power output (D)	MW_e	558.69	545.62	535.90
ASU consumption	MW_e	39.91	44.73	44.72
Gasification island consumption	MW_e	8.38	9.12	10.05
AGR consumption	MW_e	6.12	39.81	36.35
Power island consumption	MW_e	19.09	18.78	18.70
Ancillary consumption (F)	MW_e	73.50	112.44	109.82
Net power output (G = D - F)	MW_e	485.19	433.18	426.08
Gross efficiency (D/A * 100)	%	53.67	46.75	45.92
Net efficiency (G/A * 100)	%	46.61	37.11	36.51
Carbon capture rate	%	0.00	90.79	91.24
CO_2 specific emissions	kg/MWh_e	741.50	86.92	85.51

As can be noticed from the Table 6, comparing with a Shell-based IGCC scheme without carbon capture (Case 1), the pre-combustion capture using either physical and chemical solvents implies an energy penalty of about 9.5 net electrical efficiency percentage points for Selexol and 10.1 for

MDEA. The difference between the evaluated physical and chemical solvents are due to the higher regeneration heat needed for the chemical solvent (MDEA). When analysing also the post-combustion capture, one can noticed that this scheme implies a higher energy penalty compared with pre-combustion capture (1.1 net percentage points compared with Selexol and 0.5 compared with the same solvent - MDEA). Basically, this can be explained by the fact that carbon dioxide concentration in the syngas (about 40% vol.) and syngas pressure (about 30 bar) are much higher compared with post-combustion case when CO_2 concentration in the flue gases is about 8 – 10% vol. and the pressure is close to the atmospheric pressure [21-22].

Table 7. Overall plant performance indicators - post-combustion capture

Main Plant Data	Units	Case 1	Case 3
Coal flowrate (a.r.)	t/h	147.80	148.18
Coal LHV (a.r.)	MJ/kg	25.353	
Coal thermal energy (A)	MW_{th}	1040.88	1043.56
Raw syngas energy (B)	MW_{th}	839.05	835.37
Cold gas efficiency (B/A * 100)	%	80.61	80.05
Syngas exit AGR energy (C)	MW_{th}	835.41	831.95
Treatment efficiency (C/B *100)	%	99.56	99.59
Gas turbine output (M701G2)	MW_e	334.00	334.00
Steam turbine output	MW_e	224.01	135.67
Expander power output	MW_e	0.68	1.45
Gross electric power output (D)	MW_e	558.69	471.12
ASU consumption	MW_e	39.91	39.98
Gasification island consumption	MW_e	8.38	8.21
AGR consumption (incl. CO_2 compression)	MW_e	6.12	27.76
Power island consumption	MW_e	19.09	19.12
Ancillary consumption (F)	MW_e	73.50	95.07
Net power output (G = D - F)	MW_e	485.19	376.05
Gross efficiency (D/A * 100)	%	53.67	45.14
Net efficiency (G/A * 100)	%	46.61	36.03
Carbon capture rate	%	0.00	90.36
CO_2 specific emissions	kg/MWh_e	741.50	90.11

From the point of view of greenhouse gas emission, the implementation of carbon capture technology for an IGCC scheme is resulting in a substantial reduction of the specific carbon dioxide emission (85-90 CO_2/MWh for pre- and post-combustion capture vs. 826.05 kg CO_2/MWh for the case without

capture). IGCC technology has also other important benefits from environmental point of view [13,23-24]: very low SO_x and NO_x emissions, possibility to process lower grade coal and lignite or other solid fuels (biomass of almost every sort, solid waste having energetic value) which are difficult to handle by conventional energy conversion process (e.g. steam plant).

CONCLUSIONS

This paper analyze from technical point of view, using modelling and simulation techniques and mass and energy integration analysis, the possibility of applying to IGCC power generation technology various carbon capture methods. One most commercially and technologically mature carbon capture method was evaluated namely gas-liquid absorption operated in pre- and post-combustion configurations. The main differences in term of energy efficiency and heat and power integration between a conventional IGCC scheme without carbon capture compared with a scheme with pre-combustion capture or a scheme with post-combustion capture were analysed in details.

As main conclusion, pre-combustion carbon dioxide capture method is more suitable for gasification process than post-combustion (0.5 - 1.1 net electricity percentage points lower energy penalty). The simulation results of the analysed plant concepts were also used for evaluation of environmental impact of gasification-based energy conversion processes with carbon capture and storage (quantification of specific CO_2 emissions, fuel decarbonisation rate).

ACKNOWLEDGEMENT

This work was supported by a grant of the Romanian National Authority for Scientific Research, CNCS – UEFISCDI, project ID PN-II-PT-PCCA-2011-3.2-0162: "*Technical-economic and environmental optimization of CCS technologies integration in power plants based on solid fossil fuel and renewable energy sources (biomass)"* - CARBOTECH.

BIBLIOGRAPHY

1. *Statistical Review of World Energy*, BP, **2011**, www.bp.com.
2. E. Tzimas, A. Mercier, C.C. Cormos, S. Peteves, *Energy Policy*, **2007**, *35*, 3991.
3. Integrated Pollution Prevention and Control (IPPC), "Reference Document on Best Available Techniques for Large Combustion Plants", European Commission, JRC, Institute for Prospective Technological Studies, Seville, Spain, **2005**.
4. European Commission (EC), DG Energy and Transport (DG TREN), "Strategic Energy Review", **2012**, http://ec.europa.eu/energy.

5. J.D. Figueroa, T. Fout, S. Plasynski, H. Mcilvired, R. Srivastava, *International Journal of Greenhouse Gas Control*, **2008**, *2*, 9.
6. Intergovernmental Panel on Climate Change (IPCC), "Special Report, CO_2 capture and storage", **2005**, www.ipcc.ch.
7. J. Davison, *Energy,* **2007**, *32*, 1163.
8. G.T. Rochelle et al., "Research Needs for CO_2 Capture from Flue Gas by Aqueous Absorption/Striping", **2001**, US DOE, Federal Energy Technology Centre, Final report.
9. C.C. Cormos, *Energy*, **2012**, *42*, 434.
10. NETL, Department of Energy, "Cost and performance baseline for fossil energy plants", Report DOE/NETL-2007/1281, **2007**.
11. International Energy Agency (IEA), Greenhouse Gas R&D Programme (GHG), "Potential for improvement in gasification combined cycle power generation with CO_2 capture", Report PH4/19, **2003**.
12. International Energy Agency (IEA), Greenhouse Gas R&D Programme (GHG), "Improvement in power generation with post-combustion capture of CO_2". Report PH4/33, **2004**.
13. C. Higman, M. Van Der Burgt, "Gasification", Elsevier Science, Second edition, **2008**.
14. C.C. Cormos, *International Journal of Hydrogen Energy*, **2009**, *3*, 6065.
15. E. de Visser, C. Hendriks, M. Barrio, M.J. Mølnvik, G. de Koeijer, S. Liljemark, *International Journal of Greenhouse Gas Control*, **2008**, *2*, 478.
16. L. Duan, M. Zhao, Y. Yang, *Energy*, **2012**, *45*, 107.
17. R. Smith, "Chemical processes: Design and integration", Wiley, **2005**.
18. C.C. Cormos, *International Journal of Hydrogen Energy,* **2010**, *35*, 7485.
19. C. Kunze, K. Riedl, H. Spliethoff, *Energy*, **2011**, *36*, 1480.
20. M. Liszka, T. Malik, G. Manfrida, *Energy*, **2012**, *45*, 142.
21. A. Padurean, C.C. Cormos, A.M. Cormos, P.S. Agachi, *International Journal of Greenhouse Gas Control*, **2011**, *5*, 676.
22. G.P. Hammond, S.S. Ondo Akwe, S. Williams, *Energy*, **2011**, *36*, 975.
23. A. Bhattacharya, D. Manna, B. Paul, A. Datta, *Energy*, **2011**, *36*, 2599.
24. C.C. Cormos, F. Starr, E. Tzimas*, International Journal of Hydrogen Energy*, **2010**, *35*, 556.

STUDIA UBB CHEMIA, LVIII, 1, 2013 (p. 133 – 140)
(RECOMMENDED CITATION)

A THEORETICAL APPROACH ON THE STRUCTURE AND REACTIVITY OF MODEL PHOSPHASTANNAPROPENES

AGOTA BARTOK[a], PETRONELA M. PETRAR[a], GABRIELA NEMEŞ[a*], LUMINIŢA SILAGHI-DUMITRESCU[a]

ABSTRACT. The stability of phosphastannapropenes and their coordination ability towards transition metal centers was estimated by DFT calculations. The influence of several substituents on the stabilization of the model compounds Mes*P(ML_n)=CCl-SnClRR', Mes*P(η^2-ML_n)=CCl-SnClRR' (R = H, R'; R' = H, Me, Mes, Ph, Fl, Mes*; ML_n = $W(CO)_6$, $PdCl_2Me$, $PtCl_2Me$ has been studied.

Keywords: *phosphastannapropenes; palladium-, tungsten- and platinum complexes; low coordinate phosphorus compounds; multiple bonding; DFT.*

INTRODUCTION

The synthesis of heteroallenescontaining one or two heavy elements from group 14 or 15 is a challenge in Organometallic chemistry. The electronic properties and the reactivity of structures like E_{15}=C=E_{14} or E_{15}=C=E_{15} are significantly different than those of allenes, as a consequence of the involvement of the heavy atom in the π-bonding [1]. It was already shown that derivatives like heteroallenes (>C=C=$E_{14/15}$) and phosphheteroallenes (-P=C=$E_{14/15}$) are very interesting from both fundamental and applied points of view [2,3,4]. Literature data show that the stability of heteroallenes is highly dependent on the type of substituents on the heavier atoms [5,6].

Due to the high reactivity of phosphastannapropenes and phospha-stannaallenes towards a wide range of chemical species, an insight in their electronic structure and properties using computational chemistry offers a good starting point for the synthetic chemist [1,3,7]. One of the first systematic computational studies in the field of heavier group 14 analogues of allenes was reported by Apeloig [8]. Recently, a theoretically study performed on

[a] *Babes-Bolyai University, Faculty of Chemistry and Chemical Engineering, Department of Chemistry, Arany Janos 11, RO-400028, Cluj-Napoca, Romania*
* *Corresponding author: sgabi@chem.ubbcluj.ro*

the not yet synthesized phosphastannaallenes >Sn=C=P– [9] showed that the BP86/LANL2DZ [10,11] level of theory is appropriate in the description of such unsaturated systems. Although there are theoretical studies on several substituted phosphastannaallenes [12], there are no studies yet on their precursors, stannyl-phosphapropenes.

The choice of the appropriate stannyl-substituted phosphaalkenes precursor is crucial for the synthesis of a stable phosphastannaallene. As shown by the experimental attempts to obtain stable phosphastannaallenes, one of the most useful substituents on the phosphorus atom is the 2,4,6-tri-*tert*-butylphenyl group (Mes*) (excellent in terms of steric protection of the P=C bond and readily available). Therefore the model compounds subjected in the present study are Mes*P=CCl-SnClRR' (where R = H, R'; R' = H, Me, Mes, Ph, Fl, Mes*). Coordination compounds of phosphastannapropenes were also investigated as the electronic effects induced by the transition metals could also make the phosphastannapropenes more prone to vicinal halogen elimination and maybe afford more stability to the phosphaallenic unit thus obtained [13].

RESULTS AND DISCUSSION

Bearing in mind our goals in the research of the phosphastannapropenes' coordination capacity to transition metals through computational [9], as well as experimental methods [14], we have studied several model compounds (Mes*P(ML_n)=CCl-SnClRR', Mes*P(η^2-ML_n)=CCl-SnClRR'), using $W(CO)_6$, $PdCl_2Me$ and $PtCl_2Me$ as the metal-containing fragment (see Scheme 1), by alternating the substituent only on the tin atom and modifying the coordination possibilities.

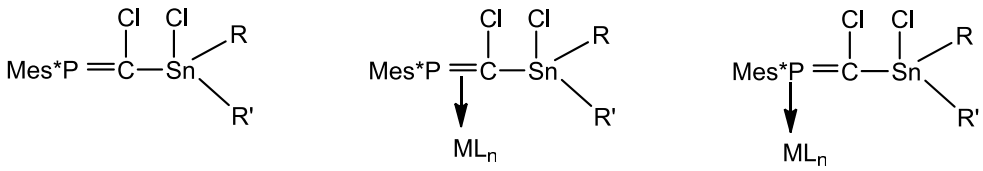

ML_n = $W(CO)_6$, $PdCl_2Me$, $PtCl_2Me$ R = H, R'; R' = H, Me, Mes, Ph, Fl, Mes*

Scheme 1

Selected computed geometrical parameters for the 1,3-phosphastannapropenes are given in Table 1, together with results from the Mulliken and NBO analysis.

Table 1. Calculated geometrical parameters, bond orders and charges for phosphastannapropenes Mes*P=C(Cl)-Sn(Cl)RR'

R	R'	C-Sn (Å)	P=C-Sn (°)	WBO C=P	WBO Sn-C	Müll.ch. C	Müll.ch. Sn
H	H	2,14	125,60	1,77	0,66	-0,74	0,65
H	Me	2,14	120,38	1,75	0,64	-0,72	0,84
H	Mes	2,15	118,79	1,75	0,62	-0,71	0,72
H	Ph	2,14	119,76	1,75	0,64	-0,72	0,79
H	Fl	2,15	120,67	1,75	0,62	-0,74	0,88
H	Mes*	2,17	119,35	1,76	0,60	-0,74	0,65
Me	Me	2,15	120,95	1,76	0,6	-0,74	1,09
Mes	Mes	2,17	123,88	1,77	0,55	-0,79	0,97
Ph	Ph	2,15	121,19	1,75	0,60	-0,77	1,06
Fl	Fl	2,11	121,54	1,75	0,64	-0,80	0,93
Mes*	Mes*	2,24	125,33	1,76	0,53	-0,82	0,90

The calculated Sn-C bond distances lie between 2.137 (R = R' = H) and 2.240 (R = R' = Mes*). This is in agreement with experimental determinations in solid state for the single tin-carbon bond, lying between 2.11 and 2.24 Å [15]. The P-C double bond is shown not to be influenced significantly by the nature of the R and R' substituents. The calculated values are close to those previously reported in the literature from X-ray data [16]. The P-C-Sn angles vary between 118.79° and 125.6° in good agreement with the results reported for similar systems (phosphagermapropenes [17] and phosphasilapropenes [18]). The Mulliken atomic charge on the tin atom varies between 0.65 and 1.09. The lowest value was found when R = R' = H and R = H, R' = Mes*. The highest positive value is found in the case of R = R' = Me or Ph. In the case of the hydrogen containing derivatives, charge transfer occurs from a σ(Sn-H) bonding orbital to the antibonding σ^*(Sn-C_c) orbital, leading to an average Sn-C bond order of 0.62 (C_c denotes the central carbon atom). In the phosphastannapropenes whithout at least one Sn-H bond the donation from the σ (Sn-$C_{R,R'}$) bonding orbital to the antibonding σ^*(Sn-C_c) orbital ($C_{R,R'}$ denotes the *ipso* carbon atom of the R and R' substituents) was observed. In these cases the average Sn-C bond order is around 0.60. No donor-acceptor interactions involving the Sn-C_c bond could be identified in the compounds with R = R' = Mes, Fl and Mes*, therefore the average Sn-C bond order is lower than in the previous two cases (i.e. 0.54).

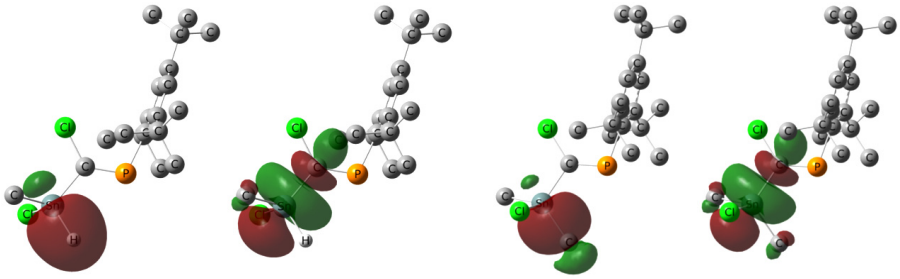

Figure 2. Natural bond orbitals involved in second order perturbation interactions: σ (Sn-H) → σ*(Sn-C_c) for Mes*P=CCl-SnClHMe and σ (Sn- $C_{R,R'}$) → σ*(Sn-C_c) interactions for Mes*P=CCl-SnClMe$_2$

The coordination of phosphastannapropenes to different transitional metals through the phosphorus atom or the P=C double bond was evaluated using model compounds. The optimized geometries obtained are presented in Table 2.

A comparison of the coordination through the phosphorus atom or the double bond can be inferred on the basis of the data in Tables 2 and 3. The highest positive Mulliken atomic charge value on the tin atom is found when R = R' = Me or Ph (varying between 0.65 and 1.09). We chose the methyl group to compare the specified coordinated phosphastanna-propenes.

Table 2. Optimized Mes*P(ML_n)=CCl-SnClMe$_2$ and Mes*P(η^2-ML_n)=CCl-SnClMe$_2$ geometries

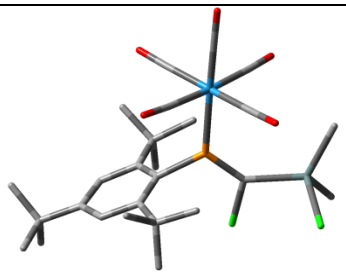 Mes*P(W(CO)$_6$)=C(Cl)-SnClMe$_2$	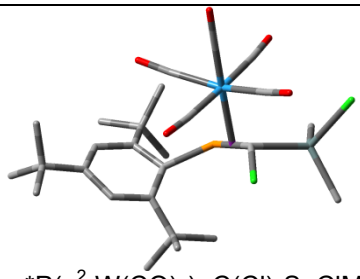 Mes*P(η^2-W(CO)$_6$)=C(Cl)-SnClMe$_2$
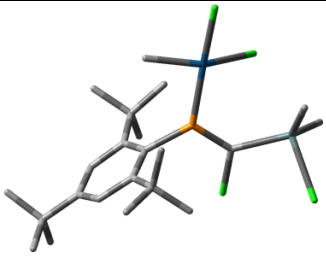 Mes*P(PtMeCl$_2$)=C(Cl)-SnClMe$_2$	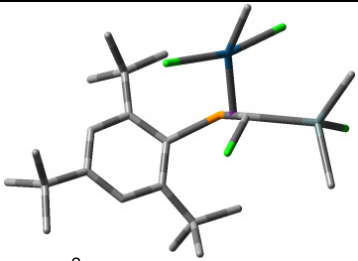 Mes*P(η^2-PtMeCl$_2$)=C(Cl)-SnClMe$_2$

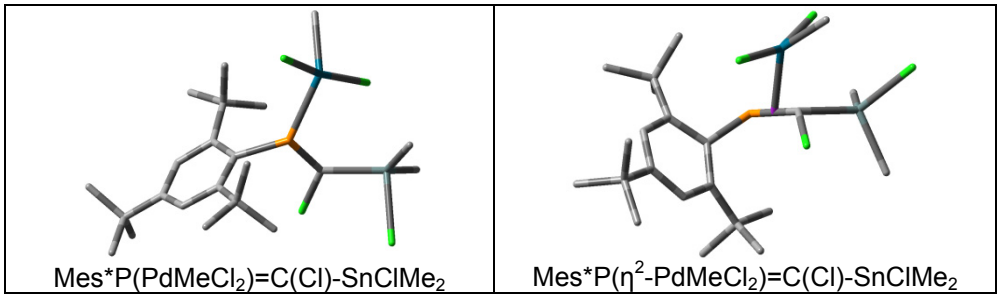

Mes*P(PdMeCl$_2$)=C(Cl)-SnClMe$_2$ | Mes*P(η^2-PdMeCl$_2$)=C(Cl)-SnClMe$_2$

The energy difference between the phosphorus coordinated and the double bond coordinated metal compounds is 7.35 kcal/mol for the platinum derivatives and as high as 15.76 kcal/mol in the case of the tungsten complexes (Table 3). The same preference was noticed for all platinum and tungsten complexes. If we compare the two types of coordination to the PdMeCl$_2$ fragment, the energetically favoured situation is found to be the one where the metal is coordinated by the phosphorus-carbon double bond (Table 3). This behaviour is the same for all palladium derivatives.

Table 3. Calculated energies and geometrical parameters for Mes*P(ML$_n$)=CCl-SnClMe$_2$, Mes*P(η^2-ML$_n$)=CCl-SnClMe$_2$

Coordination mode	PtMeCl$_2$		PdMeCl$_2$		W(CO)$_6$	
	P atom	P=C db	P atom	P=C db	P atom	P=C db
ΔE (kcal)	0	7.35	8.49	0	0	15.76
C=P (Å)	1.73	1.89	1.76	1.86	1.73	1.85
C-Sn (Å)	2.18	2.23	2.19	2.23	2.16	2.20
P=C-Sn (°)	126.5	118.10	124.03	114.01	134.74	108.36
WBO C=P	1.67	1.11	1.59	1.20	1.68	1.25
WBO C-Sn	0.52	0.46	0.51	0.48	0.57	0.51
M←L (Å)	2.36	2.28*	2.50	2.14*	2.61	2.18*
Mülliken charge C	-0.73	-0.97	-0.64	-0.87	-0.71	-0.93
Mülliken charge Sn	1.05	1.13	1.10	1.13	1.06	1.11

**the distance between the metal and the middle of the P=C bond is given*

These results indicate that the preferred coordination mode is influenced by the nature of the transition metal atom and that the substituents on tin have little or no effect. It should be noted, however, that coordination through the phosphorus atom favors a *syn* arrangement of the two chlorine atoms, which in turn would facilitate their elimination through a lithium derivative leading to a C=Sn bond.

The P=C-Sn angles (Table 3, Table 4) obtained by the DFT method are in the range with the values reported in the literature for coordination compounds containing the P=C-Si unit or P=C-Ge unit (124.83° and 119.22° [19], respectively) with a phosphorus-metal bond.

Table 4. Calculated geometrical parameters for Mes*P(W(CO)$_6$)=C-SnClRR'

R	R'	C-Sn (Å)	P=C-Sn (°)	WBO C=P	WBO C-Sn	M←L (Å)	Müll. ch. C	Müll. ch.Sn
H	H	2,14	129,70	1,64	0,65	2,60	-0,68	0,62
H	Me	2,15	131,12	1,67	0,61	2,65	-0,68	0,84
H	Mes	2,19	112,85	1,23	0,54	2,88	-0,90	0,78
H	Ph	2,15	132,16	1,68	0,60	2,65	-0,70	0,80
H	Fl	2,17	133,14	1,68	0,58	2,65	-0,69	0,85
H	Mes*	2,17	128,43	1,67	0,57	2,62	-0,73	0,66
Me	Me	2,16	134,74	1,68	0,57	2,61	-0,71	1,06
Mes	Mes	2,22	132,89	1,69	0,52	2,66	-0,79	0,96
Ph	Ph	2,15	130,35	1,68	0,56	2,62	-0,77	1,04
Fl	Fl	2,17	132,62	1,67	0,53	2,61	-0,77	1,12
Mes*	Mes*	2,29	136,06	1,70	0,48	2,70	-0,79	0,88

CONCLUSIONS

A computational study of the influence of substituents on the tin atom on the stabilization of P=C-Sn species as precursors for phosphastannaallenes was reported. Tin-carbon bond orders are shown to be increased by the presence of methyl or phenyl groups on the tin atom. The coordination ability of model phosphastannapropenes to tungsten-, platinum- and palladium-organometallic fragments has also been investigated. The data indicates that, as in the case of silyl-phosphaallkenes, coordination through the phosphorus atom is preferred by platinum and tungsten. Coordination *via* phosphorus-carbon double bond is preffered by palladium.

METHODS AND BASIS SETS

Calculations were carried out using the Gaussian 09 [12] program, at the BP86/LANL2DZ[10,11] level of theory. All structures were optimized and a vibrational analysis was performed to confirm that the obtained geometries are a global minimum.

ACKNOWLEDGMENTS

This work is supported by UEFISCDI (Contract no. PCCE-140/2008).

REFERENCES

1 J. Escudié, H. Ranaivonjatovo, L. Rigon, *Chem. Rev*., **2000**, *100*, 3639;

2 J. Escudié, H. Ranaivonjatovo, *Organometallics,* **2007**, *26*, 1542;

3 J. Escudié, G. Nemes, *C. R. Chimie*, **2010**, *13*, 954;

4 J. Escudié, H. Ranaivonjatovo, M. Bouslikhane, Y. El Harouch, L. Baiget, G. Cretiu Nemes, *Russ. Chem. Bull.***, 2004**, *53*, 1020;

5 B.E. Eichler, G.E. Miracle, D.R. Powell, R. West, *Main Group Metal Chemistry*, **1999**, *22*, 147;

6 M. Yoshifuji, *J. Organomet. Chem*., **2000**, *611*, 210;

7 A. Kunai, Y. Matsuo, J. Ishikava, Y. Aso, T. Otsubo, F. Ogura, *Organometallics*, **1995**, *14*, 1204;

8 N. Sigal, Y. Apeloig, *Organometallics,* **2002**, *21*, 5486;

9 P.M. Petrar, A. Bartok, G. Nemes, L. Silaghi-Dumitrescu, J. Escudié, *C. R. Chimie*, **2013**, *in press*, DOI 10.1016/j.crci.2012.10.013;

10 a) A.D. Becke, *Phys. Rev. A*, **1988**, *38*, 3098; b) J.P. Perdew, *Phys. Rev. B*, **1986**, *33*, 8822;

11 a) T.H. Dunning Jr., P.J. Hay, "Modern Theoretical Chemistry" Vol. 3, Plenum Press, New York, **1976**, 1; b) J. Hay, W.R. Wadt, *J. Chem. Phys.*, **1985**, *82*, 299;

12 *Gaussian 09, Revision A.02,* M.J. Frisch, G.W. Trucks, H.B. Schlegel, G.E. Scuseria, M.A. Robb, J.R. Cheeseman, G. Scalmani, V. Barone, B. Mennucci, G.A. Petersson, H. Nakatsuji, M. Caricato, X. Li, H.P. Hratchian, A.F. Izmaylov, J. Bloino, G. Zheng, J.L. Sonnenberg, M. Hada, M. Ehara, K. Toyota, R. Fukuda, J. Hasegawa, M. Ishida,T. Nakajima, Y. Honda, O. Kitao, H. Nakai, T. Vreven, J.A. Montgomery Jr., J.E. Peralta, F. Ogliaro, M. Bearpark, J.J. Heyd, E. Brothers, K.N. Kudin, V.N. Staroverov, R. Kobayashi, J. Normand,K. Raghavachari, A. Rendell, J.C. Burant, S.S. Iyengar, J. Tomasi, M. Cossi, N. Rega, J.M. Millam, M. Klene, J.E. Knox, J.B. Cross,V. Bakken, C. Adamo, J. Jaramillo, R. Gomperts, R.E. Stratmann,O. Yazyev, A.J. Austin, R. Cammi, C. Pomelli, J.W. Ochterski, R.L. Martin, K. Morokuma, V.G. Zakrzewski, G.A. Voth, P. Salvador, J.J. Dannenberg, S. Dapprich, A.D. Daniels, Ö. Farkas, J.B. Foresman, J.V. Ortiz, J. Cioslowski and D. J. Fox, *Gaussian, Inc., Wallingford CT*, **2009**;

13 R.M. Birzoi, D. Bugnariu, R.G. Gimeno, A. Riecke, C. Daniliuc, P.G. Jones, L. Konczol, Z. Benko, L. Nyulaszi, R. Bartsch, W.-W. du Mont, *Eur. J. Inorg. Chem.*, **2010**, *1*, 29;

14. A. Lini, P. Petrar, G. Nemes, R. Septelean, L. Silaghi-Dumitrescu, H. Ranaivonjatovo, *Rev. Roum. Chim.,* **2012**, *57*, 287*;*
15 A.G. Davies, “Organotin Chemistry”; VCH: Weinheim, **1997**;
16 a) L.N. Markovski, V.D. Romanenko, *Tetrahedron*, **1989**, *45*, 6019; b) R. Appel, “Multiple Bonds and Low Coordination in Phosphorus Chemistry”, Georg Thieme Verlag, Stuttgart, **1990**;
17 F. Ouhsaine, H. Ranaivonjatovo, J. Escudié, N. Saffon, M. Lazraq, *Organometallics*, **2009**, *28*, 1973;
18 A. Bartok, R. Septelean, P.M. Petrar, G. Nemes, L. Silaghi-Dumitrescu, H. Ranaivonjatovo, S. Mallet-Ladeira, N. Saffon, C. Hemmert, H. Gornitzka, *J. Organomet. Chem.,* **2013***, 724,* 200;
19 Y. El Harouch, H. Gornitzka, H. Ranaivonjatovo, J. Escudié, *Organomet. Chem.*, **2002**, *643*, 202.

STUDIA UBB CHEMIA, LVIII, 1, 2013 (p. 141 – 149)
(RECOMMENDED CITATION)

WOOD FIBERS CHARACTERIZATION BY TGA ANALYSIS

AMALIA MIHAELA IURIAN[a], IOANA PERHAIŢA[b], RALUCA ŞEPTELEAN[c], ALINA SAPONAR[b,c*]

ABSTRACT. The thermal analysis for some wood fibers (from sawdust) and for the corresponding composites plate is reported. The thermal stability domains, the partial and the total weight loss and the T_{max} of the weight loss maxima were determined on the basis of TG and DTG plots registered in nitrogen flow. It was demonstrated that, in the case of chemically treated sawdust fibers, the maximum of decomposition temperature decreased with the increasing of the concentration of alkaline solution and in the case of the composite plates, with the increasing of the alkaline solution concentration, the thermal stability of the composite plate increases.

Keywords*: wood, thermal analysis, lignin, cellulose*

INTRODUCTION

In the last period, a particular attention is given to the new materials with improved properties including composite materials reinforced with wood fibers. The latest research in the field highlights the use of sawdust in obtaining such materials [1].

Thermogravimetric analysis (TGA) has become the most frequently used characterization method for many materials. The TGA is particularly more adapted for the mass variation study. The protocols used depend on the quality and the physical characteristic of the discussed materials. The measurements in TGA can be performed during a rising in temperature, in static rate (isotherm) or under a temperature program, in controlled atmosphere.

[a] *Technical University of Cluj-Napoca, Faculty of Materials and Environmental Engineering, B-dul Muncii Nr. 103-105, RO-400641 Cluj-Napoca, Romania*
[b] *"Raluca Ripan" Institute for Research in Chemistry, Babes-Bolyai University 400294, Cluj-Napoca, Romania*
[c] *Babes-Bolyai University, Faculty of Chemistry and Chemical Engineering, 40084, Cluj-Napoca, Romania*
* *Corresponding author: saponar_alina@yahoo.com*

The thermogravimetric analysis of the raw materials (wood fibers) and the composite plates with wood waste and resin is performed to determine their chemical characteristics and it's based on tracking weight changes of the materials depending on temperature. By the use of TGA method we can study the structure of wood fibers, the oxidative stability, and the moisture- or volatile content [1-7]. Thermal degradation of the wood fibers in chemical constituents was also studied, knowing that, this degradation begins at 250ºC with cellulose degradation and ends at 450ºC with degradation of lignin [8-12]. According the literature data [13] natural lignin contains some functional groups like methoxyl, phenolic hydroxyl, primary and secondary aliphatic hydroxyl, aldehyde and ketone which can be modified during the thermal treatment. A qualitative determination of the composition of thermoplastic wood composites was performed using TGA technique [14].

Our interest in the study of these new types of composite materials [15-18] is due to the interesting properties and multiple applications that lignin based composite materials can have.

We present a detailed analysis of the thermal behavior of wood fiber and the corresponding composite materials, subjected to various surface chemical treatments.

RESULTS AND DISCUSSION

The thermogravimetric analysis offers important details to determine the properties of the new composite materials based on wood fibers. Until now, for the best of our knowledge, only the mechanical and the morphological properties of these types of treated and untreated sawdust materials have been studied [16]. Considering the possible applications of composite materials based on sawdust, a study on thermal behavior, is necessary. The thermal degradation of wood is a crucial aspect for the manufacturing process, because it determines the maximum processing temperature that can be used. On the other hand, the thermal analysis can offer useful information about the stability or the temperature range in which the compounds can be used, without changing their composition and properties.

Due to its lower thermal stability, wood is usually used as filler only in polymers that are processed at temperatures below 200 °C. Because of the high temperatures, the degradation of wood can lead to undesirable properties, such as odor, discoloration and loss of mechanical strength.

The mixed deciduous and coniferous sawdust samples used were treaded (using the literature procedure [16]) as shown in Table 1. The temperature domains of the decomposition stages, including the starting point (onset), the partial and total weight loss (on TG plots) and the T_{max} [ºC] of the weight loss maxima (on DTG plots) are also described.

For the untreated and treated sawdust (with NaOH and KOH), the weight loss varies between 69.2 and 81.1% and for the composite plates (untreated and treated sawdust impregnated with resin) between 81.2 and 85.3% (Figure 1).

The total mass loss is higher for untreated wood fibers, in comparison with the treated wood. This may be due to the impurities that are on the surface of the wood fibers. For the wood fibers treated with NaOH solution, the mass loss is smaller, due to the advance cleaning of the fiber surface. The smallest weight loss (69.2%) was obtained in the treatment with KOH in solution (10%), which shows a thorough cleaning of fibers by this method.

By treatment with alkaline solution, the cell-wall components such as ester-linked molecules of the hemicellulose can be cleaved. The resulting dissolved hemicellulose and lignin (formed by the hydrolysis of acetic acid esters) together with the swelling of cellulose, decrease the crystallinity of cellulose. Due to the cleavage of the lignin - hemicellulose or lignin – cellulose bonds, the biodegradability of the cell-wall increases [19], this tends to increase the hydrophilic behavior and hence the solubility of the material, leading to a decrease in thermal stability of the sample.

Table 1. Data of thermogravimetric analysis (TG and DTG) for the sample **1**-**8**

Sample no.	Treatment	Temperature domain [ºC]	T_{onset}* [°C]	T_{max} [°C]	Partial mass loss (Δm_p) [%]	Total mass loss (Δm_T) [%]
1	Untreated	25 - 150	-	71	4.2	80.7
		150 - 330	254	-	26.2	
		330 - 800	336	357	50.3	
2	Treated with 2% NAOH	25 - 150	-	66	4.8	75.2
		150 - 270	200	-	9.3	
		270 - 800	267	314	61.1	
3	Treated with 5% NaOH	25 - 150	-	70	4.2	72.5
		150 - 250	180	-	8.9	
		250 - 800	249	298	59.4	
4	Treated with 5% KOH	25- 150	-	64	4.0	81.1
		150 - 800	281	354	77.1	
5	Treated with 10% KOH	25 - 150	-	66	5.0	69.2
		150 - 250	180	-	9.6	
		250 - 800	249	293	54.6	
6	Composite plate: impregnated untreated sawdust	25 -150	-	65	3.4	81.2
		150 - 800	271	354	77.8	
7	Composite plate: impregnated sawdust treated with 5% KOH	25 - 330	248	315	24.2	85.3
		330 - 800	339	389	61.1	

Sample no.	Treatment	Temperature domain [ºC]	T_{onset}* [°C]	T_{max} [°C]	Partial mass loss (Δm_p) [%]	Total mass loss (Δm_T) [%]
8	Composite plate: impregnated sawdust treated with 10% KOH	25 - 330	213	303	23.4	82.8
		330 -800	350	394	59.4	

T_{onset}* = starting temperature of mass loss steps.

The thermogravimetric analysis shows that the first stage of degradation of the analyzed material occurs in the 25 ÷ 150 °C temperature range and corresponds to the loss of water (Table 1). This partial mass loss does not exceed 5%, even if the alkaline surface treatment was applied.

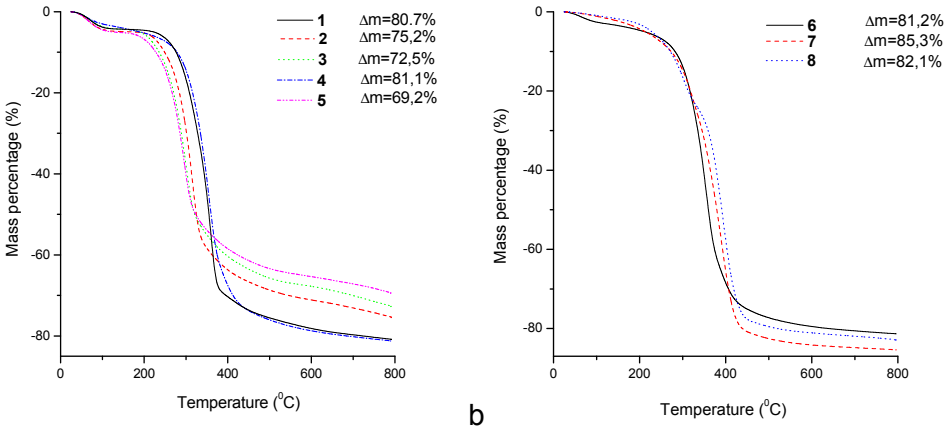

Figure 1. TG curves of the treated and untreated sawdust (a) and of the treated and untreated composite plates (b)

For all the samples, it was found that by drying these fibers at room temperature, the water absorbed during alkaline treatments was not completely removed. In order to determine how the water molecules were bonded to the wood surface, a controlled drying at 105 ºC was performed, using a temperature controlled oven. The amount of water removed at this temperature does not differ substantially between treated and untreated fibers. This fact can be explained by the presence of hydrogen bonds formed between the hydroxyl groups from the water molecules and the OH fragments forming the cellulose fiber.

The second stage of fiber degradation occurs in the 150 ÷ 300 °C temperature range and is associated with the degradation of hemicellulose from the wood fibers, which according to the literature has a deterioration interval between 150 ÷ 280 °C [9].]. This is because cellulose has a monodimensional structure and thus a relative small number of bonding sites, while hemicellulose has a bidimensional structure which could afford the formation of a higher number of interactions between their components.

Major mass loss is observed, for untreated sawdust fibers (sample **1**), at 357 °C, where the decomposition of lignin occurs, as already established in the literature [9]. In the case of the chemically treated sawdust fibers, the temperature of maximum decomposition decreased with the increasing of the concentration of the alkaline solution. Thus when applying a treatment with a solution of 10% KOH, the major weight loss is achieved at a maximum temperature of 293 °C, sample **5** being the sample with the lowest thermal stability (Figure 2a).

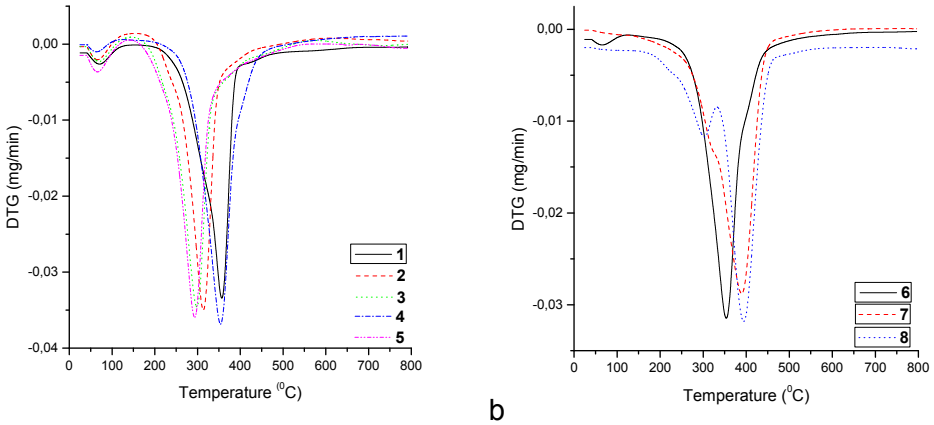

Figure 2. DTG curves of the treated and untreated sawdust (a) and of the treated and untreated composite plates (b)

In the case of the composite plates, with the increasing of the concentration of alkaline solution used in the treatment of sawdust, the thermal stability of the composite plate increases. This behavior can be explained by the amount of resin incorporated and thus giving a higher thermal stability (Figure 2b).

In order to complement this study, a FT-IR analysis was performed on samples **1**, **5**, **6** and **8** (Figure 3).

In the case of sample **1** and **5**, all the specific bands were evidenced according with literature data [20a]. The vibrations of –OH group (alcoholic or phenolic) involved in the hydrogen bonds appear in the case of sample **1,** at 3405 cm^{-1} and **5** at 3385 cm^{-1}, respectively. The stretching vibration of the C=O bonds (in ketone groups) in β location, relative to the aromatic ring, is observed at 1735 cm^{-1} in sample **1** and is not present in the treated sample **5**. The same behavior was previously described for fibers in which a reduction with lithium aluminum hydrate was performed [20b]. Stretching vibration of C=O bonds in α or γ location, relative to the aromatic rings, were observed at 1638 cm^{-1} in sample **1** and at 1595 cm^{-1} in sample **5** (Figure 3). The appearance of the –OH vibration bands in the treated sample occurs with a lowering in intensity of the vibration bands corresponding to the carboxyl groups (at 1596-1600 cm^{-1}), suggesting the partial reduction to hydroxyl groups after treatment with alkaline solution.

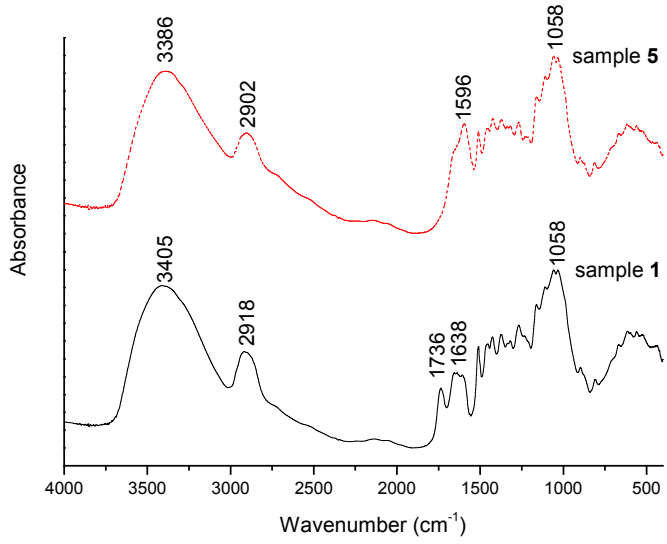

Figure 3. FT-IR spectra of sample **1** (untreated sawdust) compared to sample **5** (treated sawdust with 10% KOH)

The recorded FT-IR spectra for samples **6** and **8** (untreated and treated plates) don't show significant changes for the lignin bands when compared to the parent wood sawdust (samples **1** and **5** respectively) all the vibration bands appearing in the specific ranges.

CONCLUSIONS

The thermal behavior of sawdust (treated and untreated), in comparison with the composite plates (treated and untreated) was evaluated, on the basis of thermogravimetric plots.

The total mass loss is higher for untreated wood fibers, relatively with the treated wood. For the wood fibers treated with NaOH solution, the mass loss is smaller, due to the advance cleaning of the fiber surface. The smallest weight loss (69.2%) was obtained in the treatment with 10% KOH solution, showing a thorough cleaning of fibers by this method.

The first stage of degradation occurs in the 25 ÷ 150 °C temperature range and corresponds to the loss of water. The second stage of the fiber degradation occurs in the 150 ÷ 300 °C temperature range and is associated with the degradation of hemicellulose from the wood fiber.

The maximum of decomposition temperature decreased with the increasing of the concentration of alkaline solution, the sample **5**, being the sample with the lowest thermal stability. This could be justified by the fact that a higher concentration of the alkaline solution, creates a more intense cleaning of the wood fibers by destroying the inter-connections between the wood fibers, which thus leads to a decrease of the thermal stability of the sample.

In the case of the composite plates, a higher concentration of the alkaline solution increases the thermal stability of the plate, due to a increased amount of resin incorporated and thus sample **8** has the highest thermal stability.

EXPERIMENTAL SECTION

Samples preparation

The samples 1 ÷ 8 were prepared and treated according with the protocols presented in literature [16].

Investigation methods

Thermal analysis

Thermogravimetric analysis (TGA) was performed using a Mettler Toledo TGA/SDTA851^e Thermal Analysis System. The measurements were carried out in the temperature range of 25 ÷ 800 °C, in alumina crucible, in nitrogen with a flow rate of 50 mL min^{-1}. A heating rate of 10 °C min^{-1} was used and the samples weighted between 19 ÷ 27 mg.

Infrared spectroscopy

Infrared absorption spectra were recorded on a Thermo Scientific Nicolet 6700 FT-IR spectrometer, using KBr pellets.

Sample 1: (KBr, $\nu_{max.}$, cm^{-1}) ν_{OH} = 3405; ν_{-C-H} = 2918; $\nu_{C=O}$ = 1736 (β location, in COOH group); $\nu_{C=O}$ = 1638 (α and γ location); ν_{C-O} = 1058;

Sample 5: (KBr, $\nu_{max.}$, cm^{-1}) ν_{OH} = 3386; ν_{-C-H} = 2901; $\nu_{C=O}$ = 1596 (α and γ location); ν_{C-O} = 1058;

Sample 6: (KBr, $\nu_{max.}$, cm^{-1}) ν_{OH} = 3423; ν_{-C-H} = 2925; $\nu_{C=O}$ = 1737 (β location);$\nu_{C=O}$ = 1608 (α and γ location); ν_{C-O} = 1033;

Sample 8: (KBr, $\nu_{max.}$, cm^{-1}) ν_{OH} = 3423; ν_{-C-H} = 2924; $\nu_{C=O}$ = 1602 (α and γ location); ν_{C-O} = 1033.

ACKNOWLEDGEMENTS

This work was financially supported by CNCSIS-UEFISCSU, project number PCCE 129/2008 and project number PCCE 140/2008.

REFERENCES

1. H. Jeske, A. Schirp, F. Cornelius, *Thermochim. Acta*, **2012**, *543*, 165.
2. S. Singh, C. Wu, P.T. Williams, *J. Anal. Appl. Pyrol.*, **2012**, *94*, 99.
3. F. Sliwa, N.El. Bounia, G. Marin, F. Charrier, F. Malet, *Polym. Degrad. Stabil.*, **2012**, *97*, 496.
4. H.-S. Yang, M.P. Wolcott, H.-S. Kim, H.-J. Kim, *J. Therm. Anal. Calorim.*, **2005**, *82*, 157.
5. J. Bourgois, M.C. Bartholin, R. Guyonnet, *Wood Sci. Technol.*, **1989**, *23*, 303.
6. C. Popescu, *Thermochim. Acta*, **1996**, *285*, 309.
7. J.J. Weiland, R. Guyonnet, R.Gibert, *J. Therm. Anal.*, **1998**, *51*, 265.
8. W. K.Tang, W. K. Neill, *J. Polym. Sci: Part C*, **1964**, *6*, 65.
9. J. Kudo, E. Yoshida*, J. Japan. Wood Res.*, **1957**, *3(4)*, 125.
10. J. Guo, “Pyrolysis of wood powder and gasification of wood-derived char”, Technische Universiteit Eindhoven, **2004**, 170.
11. S. Hafsi, M. Benbouzid, *Res. J. Appl. Sci.*, **2007**, *2*, 810.
12. S. Renneckar, A.G. Zink-Sharp, T.C. Ward, W.G. Glasser, *J. Appl. Polym. Sci.*, **2004**, *93(3)*, 1484.
13. V.M. Nikitin,” Lignins”, Goslesbumizdat Leningrad, **1961**.
14. F.M.B. Coutin, M.P. Wolcott, H.-S. Kim, H.-J. Kim, *J. Therm. Anal. Calorim.*, **2005**, *82*, 157.

15. A. Borlea (Tiuc), T. Rusu, S. Ionescu, O. Nemes, *Rom. J. Mat.*, **2012**, *42(4)*, 405.
16. O. Nemes, A.M. Chiper, A.R. Rus, V.F. Soporan*, O. Tataru, P. Bere, Studia UBB Chemia*, **2010**, *55*, 101.
17. A.M. Gombos, O. Nemes, V.F. Soporan, A. Vescan, *Studia UBB Chemia*, **2008**, *3*, 81.
18. O. Nemes, F. Lachaud, R. Piquet, *Studia UBB Chemia*, **2008**, *53(3)*, 25.
19. E. Sjöström, "Wood chemistry Fundamentals and applications". Press: Academic Press inc., London, Ltd, **1981**.
20. a) H.L. Herget, *J. Organomet. Chem.,* **1960**, 25, 405; b) H.L. Herget, E.F. Kurth, *J. Am. Chem. Soc.,* **1953**, *75*, 1622.